IMPLEMENTATION OF FIBER PHASED ARRAY ULTRASOUND GENERATION SYSTEM AND SIGNAL ANALYSIS FOR WELD PENETRATION CONTROL

A Thesis
Presented to
The Academic Faculty

by

Bao Mi

In Partial Fulfillment
of the Requirements for the Degree
Doctor of Philosophy in School of Mechanical Engineering

Georgia Institute of Technology
November 2003

IMPLEMENTATION OF FIBER PHASED ARRAY ULTRASOUND GENERATION SYSTEM AND SIGNAL ANALYSIS FOR WELD PENETRATION CONTROL

Approved by:

Prof. I. Charles Ume, Chairman

Prof. Yves Berthelot

Prof. Wayne Book

Prof. Karl Jacob

Prof. Chen Zhou

Date Approved: **November 14, 2003**

ACKNOWLEDGMENT

First of all, I would like to thank my advisor, Professor Charles Ume for his support and guidance throughout this research.

I would like to thank my thesis reading committee: Professors Yves Berthelot, Wayne Book, Karl Jacob, and Chen Zhou for their expertise and valuable suggestions.

I would like to acknowledge the financial supporters of this research: The Manufacturing Machines and Equipment Program of NSF under grant No. DMI-9908082.

I would also like to thank my colleagues for their collaboration and assistance along the way: Matthew Miller, Akio Kita, Erich Schlender, Matt Rogge, Sheng Liu, Dathan Erdahl, Hai Ding, Reinhard Powell, Lizheng Zhang, and Carl Hanna.

My wife, Hexin, has been supportive and compassionate beyond words. There were many times I would have given up without her encouragement and emotional support during this journey.

TABLE OF CONTENTS

LIST OF TABLES

LIST OF FIGURES

SUMMARY

Welding is a primary technique that is used to join structural components together. When optimum weld penetration depth is not achieved, the welded components must be scraped or fixed. Scraping and fixing slow down productivity and add to the product cost. A fully automated robotic welding process, equipped with on-line sensors that are able to monitor and control the depth of weld penetration in real-time, would result in increased productivity and significant cost savings.

The overall purpose of this research is to develop a real-time laser ultrasonics based system for controlling robotic weld quality by monitoring the weld pool. The concept of real-time weld quality control is quite broad and this work is narrowed down to weld penetration depth monitoring and control with Time-of-Flight (ToF) technique. The weld penetration depth is one of the most important weld geometric parameters that define the weld quality, hence remains a key control quantity. This research focuses on the implementation and optimization of a fiber phased array generation unit and the development of signal analysis algorithms to extract the weld penetration depth information from the ultrasonic signals. The developed system is based on using the fiber phased array technique to generate ultrasound, and an Electro-Magnetic Acoustic Transducer (EMAT) as a receiver. The ultrasound generated by the fiber phased array propagates through the weld pool and is picked up by the EMAT. The ultrasound ToF is measured to derive the weld penetration depth. A transient finite element (FE) model is

developed to predict the temperature distribution during the gas metal arc welding (GMAW) process. An analytical model is developed to study the propagation of ultrasound in a temperature gradient during the real-time welding. These ultrasound propagation paths are numerically traced. The cross-correlation technique has been applied to estimate the ToF of ultrasound. The analytical relationship between the ToF and the weld penetration depth, obtained by ray-tracing algorithm and geometric analysis, matches the experimentally estimated ToF very well.

The real-time weld sensing technique developed in this research is efficient and can readily be deployed for commercial applications. It will remove the major obstacle to a fully automated robotic welding process. An on-line welding monitoring and control system will facilitate mass production characterized by consistency, high quality, and low costs. Such a system will increase the precision of the welding process, resulting in quality control of the weld beads. Moreover, in-process control will relieve human operators of tedious, repetitive, and hazardous welding tasks, thus reducing welding-related injures.

CHAPTER I

INTRODUCTION

Welding is now a well-established method and a primary technique that is used to join structural components together. Traditional welding is performed by a skilled operator who is capable of detecting and correcting most major faults as the joint is fabricated, thereby achieving satisfactory weld quality. In modern manufacturing, however, automated welding processes are highly desired. Robots have extended the level of welding automation. Unlike human operators, robots do not have built-in intelligence. Without on-line sensing, their performance cannot be evaluated until the process is complete and off-line testing performed. When defects are detected off-line, costly repairs must be made which also impair the quality of the weld. Therefore, on-line sensing is essential to ensure consistently high standards and reduce post-weld repair costs in automated welding. However, the development of reliable non-contact, non-destructive, on-line sensors, which are able to detect defects as they form and with the capability of operating at high temperatures and in harsh environments, remains a big challenge to a fully automated robotic welding process.

The purpose of this research is to develop a real-time laser ultrasonics based system to monitor and control the robotic weld quality. The concept of real-time weld quality control is quite broad and this work has been narrowed to weld penetration depth

monitoring and control with laser ultrasonics. The system is based on a laser phased array ultrasound generation system and an electromagnetic acoustic transducer (EMAT) reception system. Laser phased array generation of ultrasound has several advantages over bare laser generation. Laser phased array generation is more efficient than bare laser generation because it steers the ultrasonic energy to the region of interests. The array is very flexible in achieving various desired source configurations on the surface of the specimen. Among the noncontact ultrasound transducers such as EMAT, laser interferometer, and capacitance transducer, the EMAT is the most suitable receiver for real-time welding application. The laser interferometer has insufficient sensitivity for applications with rough surfaces. The capacitance transducer is sensitive to rough surfaces, ambient vibrations, and the change of the material. It is unsuitable for welding application. The EMAT may be engineered to survive harsh environments, and it is relatively insensitive to surface conditions.

1.1 Non-Destructive Evaluation of Weld

The purpose of controlling the quality of the weld is to achieve certain strength, toughness, and fatigue properties in the weld and the Heat Affected Zone (HAZ). These quality parameters are primarily affected by the geometry of the weld [Kou and Le, 1988; Savage, Lundin and Aronson, 1965]. Weld penetration depth is one of the most important geometric parameters that indicate the weld quality, hence remains a key control quantity. Weld penetration refers to the depth of melting and fusion into the base material of the weld joint. There are two major problems associated with penetration depth. They are incomplete melting and burn-through. With incomplete penetration the area available to

support loads is less than what is expected, and high stress concentrations may form at the joint. At the other extreme, excessive melting may result in burning through or unnecessary heating of the weldment. Therefore, monitoring and maintaining an appropriate penetration depth for a base material of given thickness is essential to obtaining a consistent weld quality.

Various non-destructive weld evaluation techniques have been investigated and developed over the past years. Among them, radiographic technique, vision technique, and ultrasonic technique are the most commonly employed approaches.

1.1.1 Radiographic Inspection of Weld

Radiographic inspection relies on detecting a change in the transmitted intensity of a gamma-ray or an X-ray beam that arise from the fact that a defect and the surrounding metal have different absorption coefficients. Radiography was the only available method for finding buried defects in welds before the advent of ultrasonic inspection. Traditional radiographic inspection uses high-quality film to take images [Placious, *et al.*, 1981; Rokhlin, 1989]. Significant progresses have been made in radiography over the years. Now, the radiographic inspection can be made filmless and applied in real-time application [Liao, 1998; Ditchburn, *et al.*, 1996; Guu and Rokhlin, 1992]. For weld inspection, the most commonly used real-time techniques rely on the conversion of X-rays to visible light using a fluorescent screen or X-ray image intensifier and coupling the light output to a TV or video camera. While radiographic inspection is a dependable way to detect porosity, inclusions, cracks, and voids in weld interiors, it is a

slow and expensive NDT method. The safety hazards associated with the use of X-rays and gamma radiation have further limited the applications of this method.

1.1.2 Infrared Sensing (Vision Technique) of Weld

Infrared and vision techniques have been applied to the weld penetration monitoring and control in the past. One general approach is to observe the weld joint from the backside, typically utilizing infrared detectors [Vorontsov, 1970]. In the simplest implementation, a certain level of broadband radiation detected is associated with the proper penetration. The penetration depth is then maintained using either welding current or travel speed as a control parameter. This approach requires access to the backside of the weld and provision for maintaining the sensor position relative to the point of welding, which cannot be easily met in most real-world configurations. A more convenient vision technique for controlling the penetration is based on the detection of weld pool width from a digitized television image [Richardson, Gutow, and Rao, 1982; Nagarajan, Chen, and Chin, 1989]. The digitized image is analyzed by a vision processor for the purpose of detecting the molten weld pool edge features and hence pool width. This approach relies on an assumption that a constant bead width to depth of penetration ratio exists for the welding condition. One particular difficulty associated with the bead width technique is that minor changes in composition have been shown to alter dramatically the penetration behavior [Sundell, Solomon, and Correa, 1986]. Chen *et al*. (1988) have experimentally investigated the relationship between the thermal image and the depth of penetration. They concluded that the thermal temperature distributions of the

plates being welded change along with the penetration and thickness of the plates being welded. However, no concrete relationships have been established.

1.1.3 Ultrasonic Sensing of Weld

Ultrasonics was first introduced as a NDT technique for weld inspection in the 1960's. Since then, this technique has undergone extensive development and gained increasing acceptance. Consequently, ultrasonics is now the major technique used for validation of welded structures in many in-service inspection applications, e.g. off-shore structures, nuclear and pressure vessel industries, and a range of naval applications. Ultrasonic sensing of the welding process has the potential to detect weld pool geometry and discontinuities in real time. Traditional ultrasonic transducers require intimate surface contact and fluid couplants, which are not applicable to on-line weld inspection where elevated temperature and rough surface are usually present [Stroud, 1989]. One alternative to the conventional contact ultrasonic method is laser ultrasonic testing, which has attracted a lot of research efforts since it was first demonstrated by White in 1963. In such a system, a pulsed laser is used to generate ultrasound and a laser interferometer is used to pick up the ultrasound propagated through the inspected media. Indeed, a pulsed laser can be used as an efficient broadband generator. On the other hand, laser interferometry receiving systems generally require shining and smooth surface finish over the inspection region, which usually does not exist in welding environment. One solution for this weakness is to replace the problematic laser receiver with an EMAT. While the EMAT needs to be placed in close proximity to the specimen surface and hence is not a remote means to pick up the ultrasound, it is a non-contact transducer and requires no

couplants or special surface preparation, and can be made to operate at elevated temperatures. The EMAT, though not an efficient generator of ultrasound, can be designed and built as an excellent receiver for both longitudinal and shear waves.

Laser/EMAT hybrid system has been investigated in various inspection applications. Idaho National Engineering Laboratory (INEL) has developed ultrasonic sensing techniques to determine the quality of weld with both contact transducers and non-contact ultrasound generation and receiving techniques (laser/EMAT) [Carlson and Johnson, 1988, Carlson, *et al*. 1992]. A ray-tracing algorithm has been implemented to perform the path analysis. The sensing system was able to detect the incomplete penetration in a weld joining two 12.7 mm thick carbon steel plates based on presence or absence of the signal of interest in the acquired A-scans. In this system, only qualitative information of the weld pool geometry has been extracted from the A-scan results.

A multiple cavity pulsed laser/meander line EMAT system has been used to inspect a steel plate weld specimen for cracks off-line [Oursler, Wagner, 1995]. Thermoelastic generation is desired in this system to excite strong angled shear wave (30° lobe). A ten-cavity laser system, which can generate a laser beam train at a desired delay, is used to generate narrow band ultrasound. The EMAT is tuned to be sensitive to the ultrasound with particular frequency and at specified angle. In this application, the ten-cavity laser is used only for tuning the frequency of the generated ultrasound, not for steering the ultrasonic beam as a phased array.

Another hybrid laser-EMAT system has been introduced to detect weld defects using the B-scan technique [Dixon, Edwards, Palmer, 1998]. No phased array is applied in this system. It has been demonstrated that the ultrasonic waveform detected by the

EMAT can be extremely complicated. The off-line experimental results show that this system is unable to detect all defect types or sizes. This is not surprising because the ultrasonic signal generated by a point source (single laser beam) will propagate in all directions and the signal to noise ratio is low. It will even be worse if the system is used for on-line purpose due to the elevated temperatures introduced by the welding process.

1.2 Laser Phased Array / EMAT Hybrid System for Sensing Weld Penetration Depth – Proposed Approach

The overall objective of this research is to develop a real-time ultrasound based system to control the robotic weld quality by monitoring the weld pool geometry. The concept of real-time weld quality control is quite broad and this work has focused on penetration monitoring and control with laser ultrasonics. The system is based on the laser phased array technique that has been investigated for many years by the Laser Processing lab, Georgia Institute of Technology [Hopko, Ume, 1999; Yang, Ume, 1994; Yang, DeRidder, Ume, Jarzynski, 1993]. An EMAT is used as a non-contact receiver. The ultrasound generated by the laser phased array propagates around the weld pool and is picked up by the EMAT. Algorithms are developed to measure the Time of Flight (ToF) of the ultrasound and correlate the ToF to weld penetration depth. The uniqueness of this research is that the information on weld penetration depth extracted from the ultrasonic signals will be used as feedback to control the Gas Metal Arc Welding (GMAW) parameters (welding current, arc voltage, wire feed rate, torch speed, and torch angle etc…), to achieve desired penetration depth, and hence to increase weld quality.

Weld penetration depth detection has been studied on simulated liquid weld with laser linear array and EMAT configuration [Graham, Ume, 1997; Graham, Sanderson, Ume, 1993]. The results show that penetration depth of simulated liquid welds can be determined by ultrasound ToF techniques. Simulated welds provide a means of demonstrating the feasibility of applying a non-contact laser-EMAT ultrasonic evaluation system to real-time welds.

This dissertation focuses particularly on the implementation and optimization of the laser phased array generation unit used for monitoring real GMAW process and application of signal processing techniques on the received ultrasonic signals. In the real-time welding environment, both attenuation and noise levels will be increased compared to those in the simulated weld pool. High attenuation is due to the elevated temperature. High noise level is caused by the high levels of electromagnetic noise resulting from the welding process and acoustical noise disturbances in the manufacturing setting. As a result, use of a strong ultrasound generation is required in actual real-time weld inspection. A phased array is one means to enhance the ultrasound generation at certain desired directions. Successful application of the phased array, however, requires significant optimization work.

CHAPTER II

BACKGROUND

2.1 ULTRASONIC GENERATION BY LASER

When a pulsed laser beam is incident on a specimen, a portion of the energy is absorbed by the specimen and the rest of the portion is reflected. The absorbed energy pulses serve as the source of the generated ultrasound that travels within the specimen. Based on the input laser power density levels, the ultrasound can be generated in three regimes: thermoelastic regime, transition regime, and ablation regime. The laser source is usually modeled as an ideal point source for simplicity.

2.1.1 Thermoelastic Regime

When the absorbed energy is within the thermoelastic regime for the tested material, the induced stresses fall below the elastic limit for that material and no permanent deformation or damage occurs.

Thermal expansion and compression in the thermoelastic regime are expected to be in the direction parallel to the material surface (Fig. 2-1). So, a thermoelastic source is usually represented as a point dilatation (center of expansion) at the surface. [Hutchins, *et al.*, 1981]

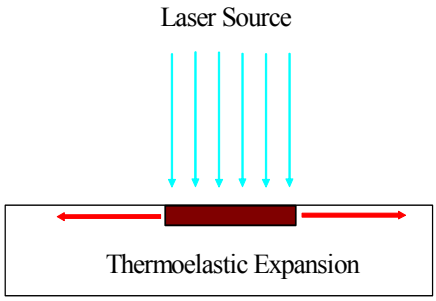

Fig. 2-1: Thermoelastic generation mechanism.

Under thermoelastic regime, the directivity patterns are described by Eq. 2-1 for longitudinal wave and Eq. 2-2 for shear wave [Rose, 1983]. In deriving these equations, a point source is assumed. Bernstein and Spicer (2000) have analytically and experimentally confirmed that the directivity pattern produced by a thermoelastic line source is identical to that by a point source. The directivity patterns of the ultrasound generated in thermoelastic regime are shown in Fig. 2-2.

$$u_L \propto \frac{\sin\theta \sin 2\theta \sqrt{k^2 - \sin^2\theta}}{(k^2 - 2\sin^2\theta)^2 + 2\sin\theta \sin 2\theta \sqrt{k^2 - \sin^2\theta}} \qquad \text{Eq. 2-1}$$

$$u_S \propto \frac{\sin 2\theta \left(1 - 2\sin^2\theta\right)}{(1 - 2\sin^2\theta)^2 + 2\sin\theta \sin 2\theta \sqrt{k^{-2} - \sin^2\theta}} \qquad \text{Eq. 2-2}$$

where,

u_L: Magnitude of longitudinal wave

u_S: Magnitude of shear wave

θ: Angle measured away from inner surface normal (refer 0° position in Fig. 2-2)

$k = \frac{c_L}{c_S}$: Ratio of the longitudinal wave velocity to the shear wave velocity

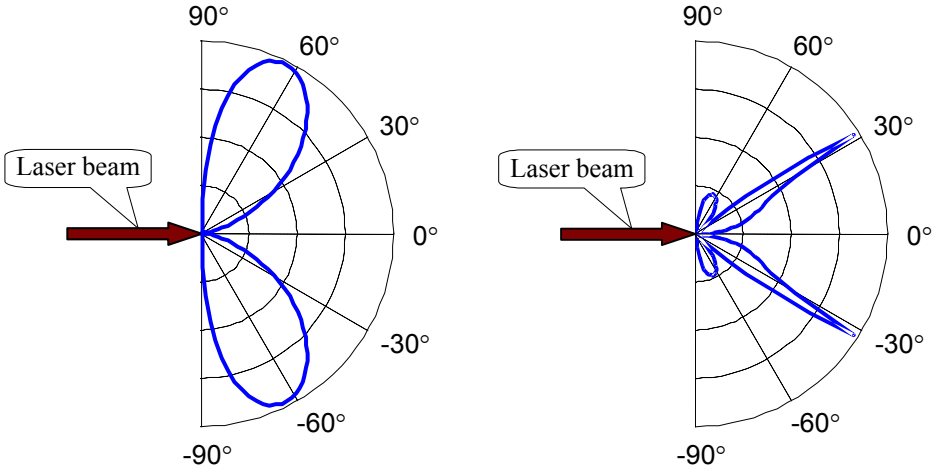

a) longitudinal wave b) shear wave

Fig. 2-2: Theoretical directivity pattern in thermoelastic regime (steel).

2.1.2 Intermediate Regime

The intermediate regime happens when the absorbed energy causes melting but no vaporization. The power range in this regime is too narrow to be of practical interest. Material testing in this regime is highly uncertain. The transition regime is avoided because this regime is neither nondestructive nor able to produce strong signals. No rigorous models for the intermediate regime have been found in literature.

2.1.3 Ablation Regime

Ablation occurs when the absorbed laser energy causes vaporization. The material that departs from surface with an outward momentum generates a normal force on specimen, which in turn produces bulk waves and surface waves (Fig. 2-3).

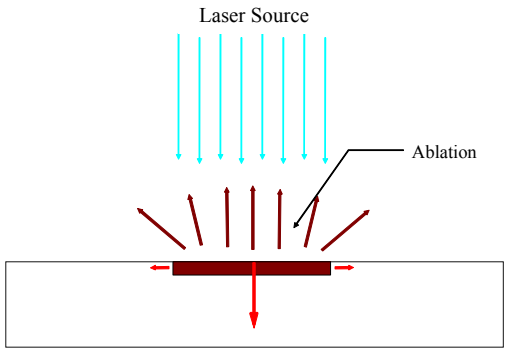

Fig. 2-3: Ablation generation mechanism.

Under ablation condition, the longitudinal wave is dominant. The source in ablation regime is usually modeled temporally as an impulse and spatially as a point force. This model results in the directivity patterns of Eq. 2-3 and Eq. 2-4 [Miller and Pursey, 1954], illustrated in Fig. 2-4.

$$u_L \propto \frac{2k^2 \cos\theta(k^2 - 2\sin^2\theta)}{(k^2 - 2\sin^2\theta)^2 + 4\sin^2\theta\sqrt{1-\sin^2\theta}\sqrt{k^2 - \sin^2\theta}} \qquad \text{Eq. 2-3}$$

$$u_s \propto \frac{\sin 2\theta\sqrt{1-k^2\sin^2\theta}}{k(1-2\sin^2\theta)^2 + 4\sin^2\theta\sqrt{1-\sin^2\theta}\sqrt{1-k^2\sin^2\theta}} \qquad \text{Eq. 2-4}$$

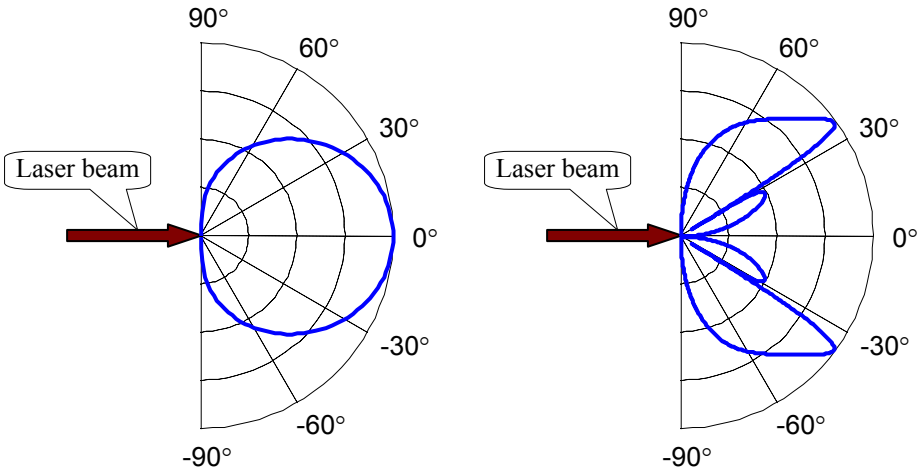

a) longitudinal wave b) shear wave

Fig. 2-4: Theoretical directivity pattern in ablation (steel).

2.1.4 Laser Power Density Threshold for Ablation

The ultrasound is generated by a pulsed laser in different regimes at various levels of laser power density. The specimen surface temperature affects the laser power density threshold. The difference between initial surface temperature and boiling point directly relates to the amount of energy required for ablation [Aussel *et al.*, 1988]. Eq. 2-5 predicts the required laser power density at which vaporization starts.

$$W_A = \frac{\pi}{4}\sqrt{\frac{K\rho C_v}{\tau_0}(T_v - T_i)^2} \qquad \text{Eq. 2-5}$$

where,

W_A: Absorbed power density

K : Thermal conductivity

ρ : Density

C_v Specific heat capacity

τ_0 : Duration of the laser pulse

T_v : Vaporization temperature

T_i : Initial temperature of the material

The thermoelastic limit can be calculated by replacing T_v , the vaporization temperature, with T_m , the melting point of the material. When aluminum is considered, the laser power density thresholds estimated by Eq. 2-5 for three regimes are plotted in Fig. 2-5.

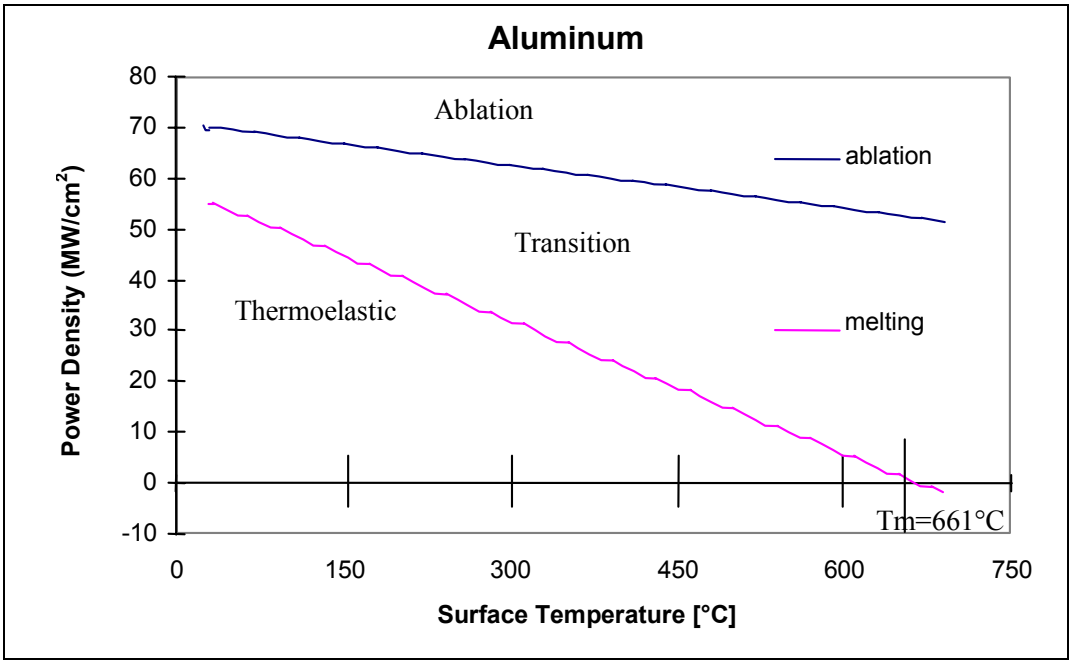

Fig. 2-5: Laser power density limits vs. specimen temperature in aluminum [Hopko, 1998].

2.2 PHASED ARRAY AND OPTICAL FIBERS

2.2.1 Phased Array

A phased array, a tool to make the ultrasound field be steered and amplified in a particular direction, can be designed and implemented to enhance the signal propagation in the region of interest.

A phased array is comprised of multiple sources with a time lag, illustrated by Fig. 2-6. The ultrasound field generated from each of the sources interacts to form predictable interference patterns that can be controlled by proper temporal and spatial arrangement of the sources.

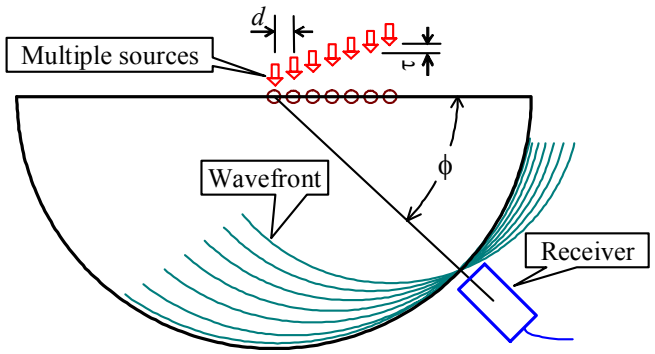

Fig. 2-6: Phased array.

An additional feature of phased arrays is that the destructive interference at angles other than the beam steering angle results in a reduction in the amplitude of the ultrasound signal. This feature effectively narrows the region of propagation to a band of angles surrounding the beam steering angle. Therefore, signals received from phased array systems can be less complex than signals generated from a single source.

The directivity pattern $u(\theta,\phi)$ of the ultrasound generated by a phased array is the product of the directivity pattern $u_e(\theta)$ produced by an individual source and the array factor $I_a(\theta,\phi)$, expressed by Eq. 2-6 and Eq. 2-7 [Vogel, *et al.*, 1987]. Note that the longitudinal wave and the shear wave for the same material have different traveling velocities. Thus the array factors are different for each of these two waves.

$$u(\theta,\phi) = u_e(\theta)\cdot I_a(\theta,\phi) \qquad \text{Eq. 2-6}$$

$$I_a(\theta,\phi) = \left(\frac{\sin Nq}{N\sin q}\right)^2 \qquad q = \frac{\pi d}{\lambda}(\sin\theta - \sin\phi) \qquad \sin\phi = \frac{\tau c}{d} \qquad \text{Eq. 2-7}$$

where,

$u(\theta,\phi)$: Intensity distribution of the radiation pattern at any constant distance

λ : Acoustic wavelength

ϕ : Selected beam steering direction

d : Distance between source element centers

N : Number of source elements

τ : Time delay between adjacent sources

c : Ultrasound speed

A laser-based phased array is conventionally created either by using an array of fiber optic lines of varying lengths [Bruinsma and Vogel, 1988; Jarzynski and Berthelot, 1989; Yang, *et al*., 1993; Noroy, *et al*., 1993] or by using a moving laser source [Ing, Gires and Fink, 1989]. The phased array applied in this research is constructed with three

fiber sources, as shown in Fig. 2-7. Each source is composed of 7 fibers (totaling 21 fibers, bundled together at the laser end). The fibers in each of the three sources measure 2 m, 52 m, and 102 m, respectively. The 50 m length difference results in a time delay of 0.243 μs between adjacent sources based on Eq. 2-8. The distal end of the phased array is configured as three line sources.

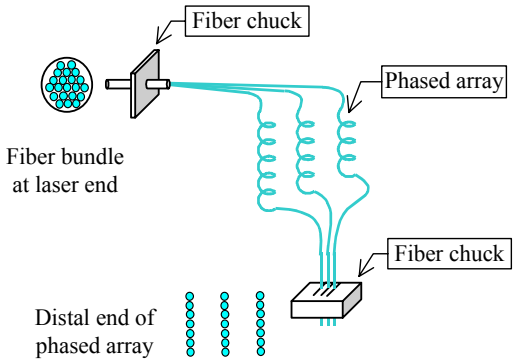

Fig. 2-7: Implementation of fiber phased array.

$$\tau = \frac{\Delta l}{c / n} \qquad \text{Eq. 2-8}$$

where,

τ : Time delay between adjacent sources

Δl : Length difference (50 m)

c : Speed of light in vacuum (3×10^8 m/s)

n : Refractive index of the fiber core (1.46 at 1064 nm wavelength)

When plugging the array parameters into Eq. 2-6 and Eq. 2-7, the directivity patterns for a 3 element array with the time delay of 0.243 μs and inter-spacing of 1.5 mm are illustrated in Fig. 2-8. These plots will help configure the array optimally.

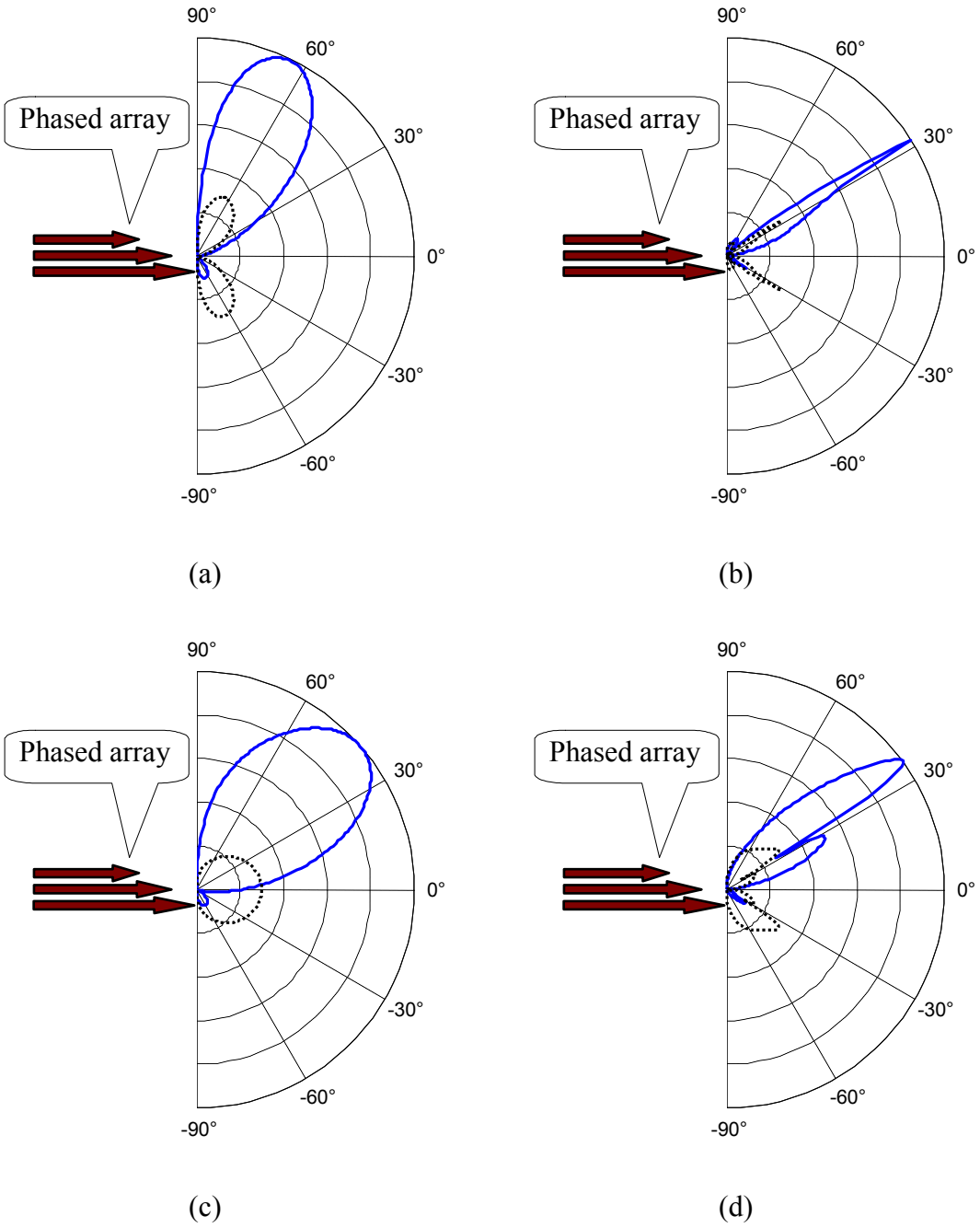

Fig. 2-8: Comparison of single source (dotted black line) and phased array (solid blue line). (a) Longitudiinal wave under thermoelastic regime. (b) Shear wave under thermoelastic regime. (c) Longitudiinal wave under ablative regime. (d) Shear wave under ablative regime.

2.2.2 Optical Fibers

Optical fibers serve as laser energy guide in many industrial applications, including laser welding and drilling [Jones, 1989; Doubrava *et al.*, 1990] and ultrasonics [Lanza di Scalea *et al.*, 1999; Jarzynski, 1989; Yang and Ume, 1994]. These applications usually require optical fibers capable of transmitting high power levels.

Typical optical fibers are composed of three layers of material: core, cladding, and jacketing (refer Fig. 2-9). The fiber core is made from the purest material, and is capable of transmitting high energy. The cladding has smaller refractive index and the core-cladding interface confines the light to the core by total reflection. The fiber jacketing serves as protection of the fiber and the material is usually chosen based on the application. The polyimide-coated fibers are made for high temperature applications. The core diameter for high-power laser applications ranges from about 400 to 1000 μm [Beck *et al.*, 1993]. Fibers larger than 1000 μm are usually not used because they are less flexible. The cladding diameter is typically 1.1 to 1.4 times the core diameter.

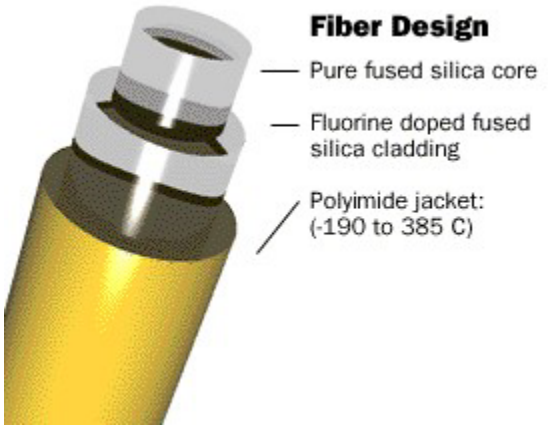

Fig. 2-9: Optical fiber design.

Of the three layers, the fiber core has the highest damage threshold and the jacketing has the lowest. When a laser beam is incident onto the end surface of the fiber, the fiber will experience permanent damage if the laser intensity exceeds its lowest damage threshold. Higher power levels can be attained by removing the jacketing material [Beck, *et al.*, 1993; Allison, *et al.*, 1985] or focusing the laser energy into the core of the fiber [Dewhurst, *et al*., 1988]. When using a fiber bundle system, the technique of focusing the laser into the core of the fiber is an impractical solution since the laser beam needs to be coupled into multiple fibers in the bundle simultaneously. Hence, the technique of removing fiber jacketing at the laser end is employed to improve the damage threshold.

2.3 Principle of EMAT Reception of Ultrasound

An EMAT is a non-contact ultrasonic transducer. While EMATs can be used both to generate and receive ultrasound, the discussion here will focus on the use of EMATs as receivers since pulsed lasers are better ultrasound generators. The non-contact operation makes EMAT a perfect solution for inspecting specimens in harsh environments and in motion.

A typical configuration for an EMAT receiver of acoustic waves in a specimen is shown in Fig. 2-10. An EMAT receiver functions through the interaction of particle displacement velocity (v) and static magnetic flux density (B). A free conduction current density distribution (J) is then established due to the mechanical vibrations of the medium and the presence of a static magnetic field. The relationship is expressed by Eq. 2-9 [Ludwig, You, and Palanisamy, 1993], where σ is the conductivity of the specimen.

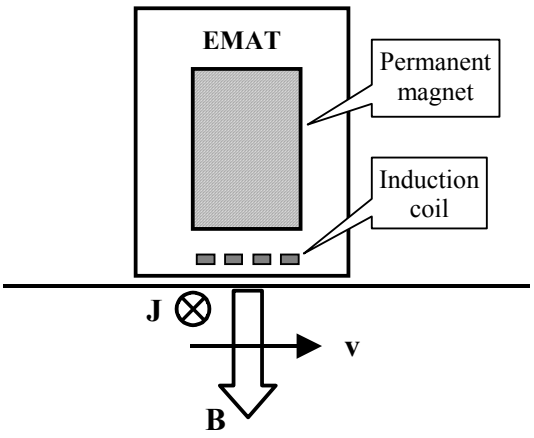

Fig. 2-10: Basic operational principle of an EMAT.

$$\mathbf{J} = \sigma \mathbf{v} \times \mathbf{B} \qquad \text{Eq. 2-9}$$

As a result, the current density is detected by the pick-up coil. The entire EMAT unit can be designed to be sensitive to either shear or longitudinal waves arriving at a particular angle and frequency by selecting appropriate direction of the magnetic field and shape of the receiving coil. An EMAT is not a point transducer like an interferometer. It has an area detection window that depends on the strength of the magnetic field and the size of the induction coil on the bottom of the EMAT assembly. As a result, ultrasound can be detected before it reaches the center of the EMAT, which introduces a bias to the ToF. The problem raised by this bias can be avoided by using relative ToF instead of absolute ToF.

Currently an EMAT assembly developed by National Institute of Standard and Technology (NIST) is used as a receiver. The EMAT was initially optimized for receiving 45° incident shear waves with a frequency bandwidth of 0.5 to 2.0 MHz. To make the EMAT suitable for this application, it was refurbished and characterized by

BWXT Services, a company that builds EMAT system for various applications. It is proven to be successful in receiving shear waves in a welding environment.

2.4 Analysis on the Wave Propagation in a Plate

The propagation of the elastic waves in a parallel-sided plate is discussed in this section. As shown in Fig. 2-11, the arrival times for bulk waves can be obtained by taking a geometric ray analysis. For simplicity the discussion is restricted to the wave arrivals given in Table 2-1, which lists the abbreviations of different wave arrivals and their meanings. It is straightforward to calculate the arrival time for the pure reflection case, such as PP and SS waves. When mode conversion happens, it is required to apply the Snell's law to determine the reflection point first.

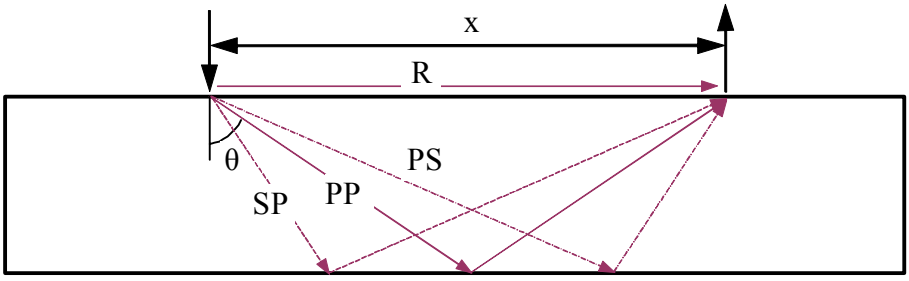

Fig. 2-11: Wave arrivals based on reflection in a plate.

In the case of weld tip diffraction, the calculation of the arrival time is straightforward because the locations of the rays are determined.

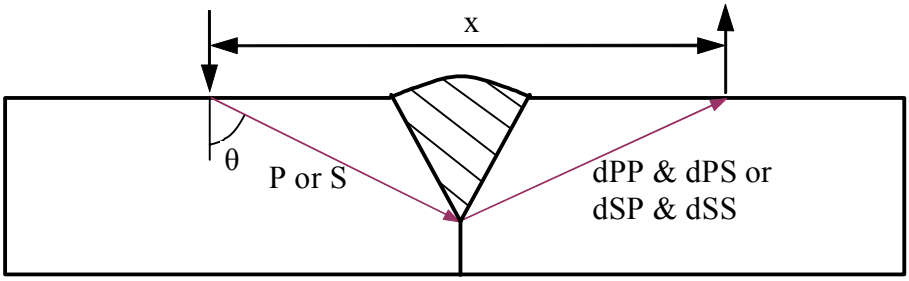

Fig. 2-12: Wave arrivals based on diffraction at the weld tip.

Table 2-1: Abbreviations of different wave arrivals.

Wave arrival	Symbol
Direct Rayleigh wave	R
Longitudinal wave reflected once	PP
Shear wave reflected once	SS
Longitudinal wave mode converted to shear wave	PS
Shear wave mode converted to longitudinal wave	SP
Diffracted longitudinal wave	dPP
Diffracted shear wave	dSS
Longitudinal wave diffracted as shear wave	dPS
Shear wave diffracted as longitudinal wave	dSP

CHAPTER III

WELD PENETRATION DEPTH INSPECTION SYSTEM

A laser phased array ultrasound generating system developed previously in this lab is implemented into the inspection system. An EMAT is used as a non-contact ultrasound receiver. The generating unit and the EMAT receiver form an on-line sensing system to monitor the weld penetration depth of the gas-metal arc welding (GMAW) process. Signal analysis algorithms are developed to extract the weld penetration depth information from the ultrasonic signals received by EMAT in real-time. This chapter discusses the overall weld penetration depth inspection system and the apparatus used in this research.

3.1 Overall System Setup

The overall system setup is illustrated by Fig. 3-1. The welding subsystem employs an Automatix AI 32v robot controller, General Electric Process P-50 robot, and a Miller Pulstar 450 welding machine. The AI 32v controller that runs the RAIL v6.04 operating system controls the P-50 process robot. The welding torch is attached to the end effector of the P-50 robot. An interface with the Pulstar 450 welder allows the AI 32v robot controller to manipulate various welding parameters such as arc voltage, wire feed rate (welding current), and welding speed. The Pulstar 450 welder controls the flow of

shielding gas, which is a mixture of 98% argon and 2% carbon dioxide. The welding machine/robot combination is ideally suited for making butt or V-grooved welds using the GMAW process.

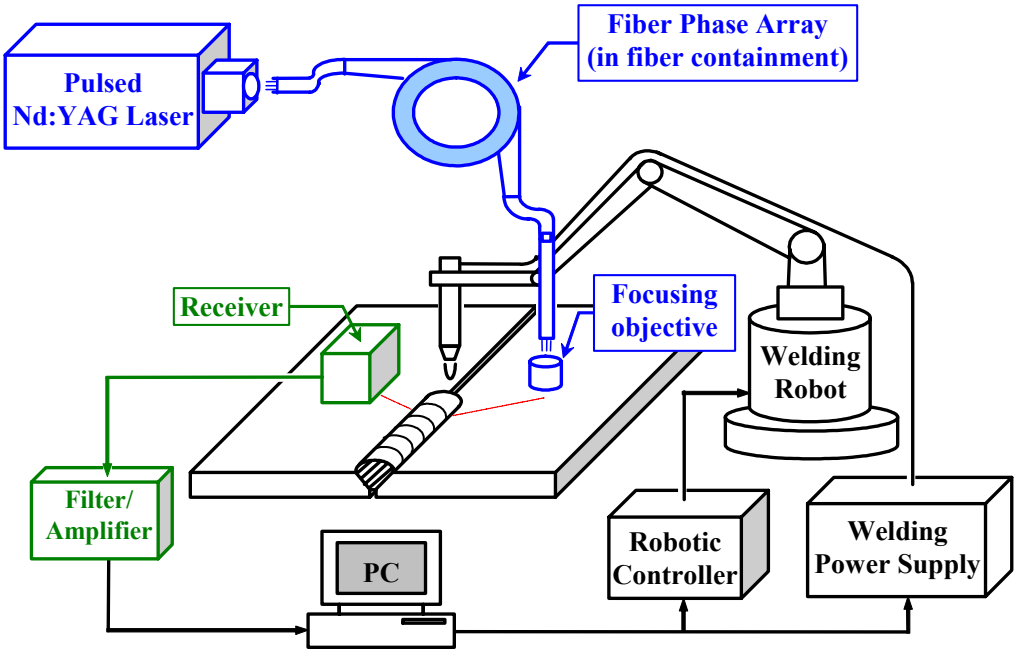

Fig. 3-1: Overall system setup.

A pulsed Nd-YAG laser is used as the light source. This laser operates at a wavelength of 1064 nm with 5~7 ns pulses at up to 650 mJ per pulse, with a firing rate of up to 20 Hz. The laser beam is coupled into the Flexible Fiber Bundle Linear Phased Array (FFBLPA) and directed onto the welding sample through the FFBLPA. A custom designed focusing objective lens is utilized to focus the beam emitting from the fibers onto the surface of the sample. It also protects the fibers from being contaminated or damaged by the ablation or welding spatter.

Ultrasonic signals are received by a receiver (angle beam PZTs or EMAT) in real-time and then acquired by a high speed acquisition card. Analysis algorithms are

developed for processing the ultrasonic signals to obtain the weld penetration. In the future, the information on the weld penetration depth will be used as a feedback to the system to correct the welding process, hence to achieve high quality weld.

3.2 Laser Phased Array Generating Subsystem

It is essential to deliver the laser beam to the surface of the specimen to be inspected efficiently and flexibly so that strong ultrasound signals can be generated and propagate along the desired direction. A laser phased array generating subsystem illustrated in Fig. 3-2 is implemented to generate ultrasound in a noncontact means. Phased arrays are constructed of multiple sources with a given spatial and temporal relationship resulting in a superposition of wave fronts at the desired beam steering angle. In this research, the phased array is composed of three line sources. Each of the three sources consists of 7 silica-silica fibers with 400 μm core. The fibers in each of the three sources measure 2 m, 52 m, and 102 m respectively. The difference in length introduces a time delay of 0.243 μs between adjacent line sources. At the laser end, the 21 fibers are arranged into a round bundle to face the laser beam. The laser beam emerging from the pulsed Nd:YAG laser is coupled into the fiber bundle.

This section presents a brief description of the components of the phased array generation system. The more detailed discussion on the implementation and characterization of the phased array is presented in Chapter IV.

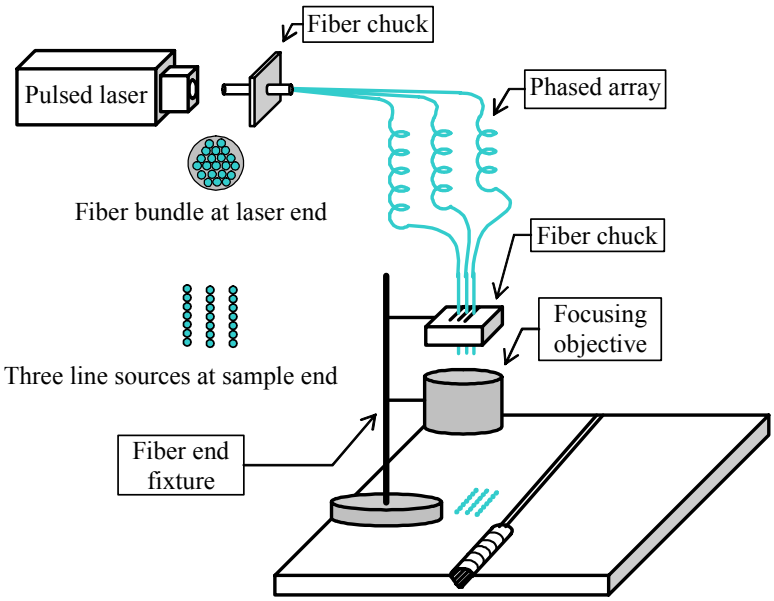

Fig. 3-2: Fiber phased array generation unit.

3.2.1 Nd-YAG Laser

The pulsed laser used as ultrasound generation source is a Surelite II model laser from Continuum, as shown in Fig. 3-3. The laser is an Nd:YAG laser, operating in the infrared (1064 nm), at 10 Hz repetition rate. The maximum laser power output is rated as 650 mJ/pulse at the wavelength of 1064 nm for a 7 mm diameter beam.

Fig. 3-3: Pulsed Nd-YAG laser used as ultrasound generation source.

The laser output power can be adjusted by changing the Q-switch delay setting. Note that higher Q-switch delays result in lower power. A power meter is used to measure the laser power. Fig. 3-4 shows the laser energy per pulse measured at different Q-switch delay settings. Q-switch setting of 250 μs is used in all of the experiments, which is experimentally proven a safe energy for optical fibers.

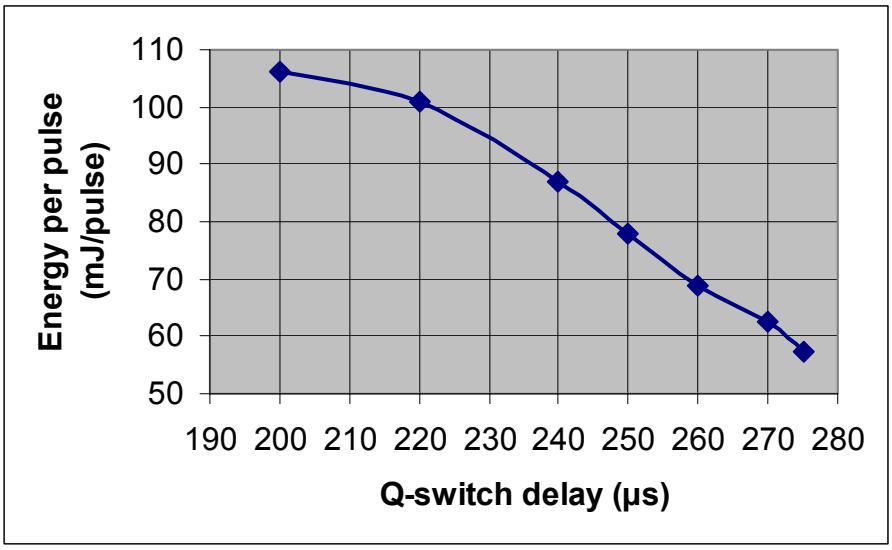

Fig. 3-4: Laser output energy vs. Q-switch delay.

It takes time for the laser power to stabilize after it is turned on. Fig. 3-5 shows a plot of the laser power over time. The result shows that the laser power becomes stabilized after about 30 minutes of warming up. The oscillation is within 1% after the first half hour. Based on this observation, all measurements are made after the laser has been warmed up for 30 min so that the experimental results are not affected by the laser power fluctuation.

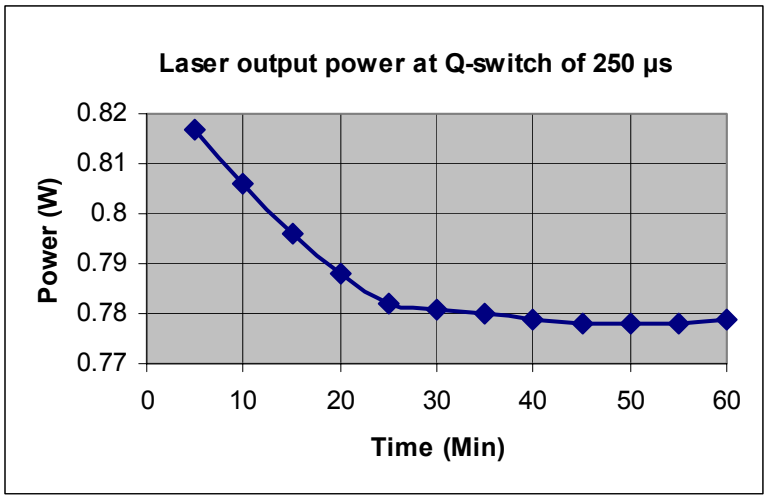

Fig. 3-5: Laser power stabilization with time.

3.2.2 Optical Fibers

The optical fibers used in this research are Optran® UV type fibers manufactured by CeramOptec Industries, Inc. The fibers are selected for this particular application based on their known performance for transmitting high power laser light and enduring high temperatures. The fibers are composed of pure silica core, doped silica cladding, and polyimide jacketing. The polyimide jacketing makes the fibers capable of operating in a broad temperature range (-190° to +385° C). The detailed fiber properties and dimensions are listed in Table 3-1.

3.2.3 Fiber Container

The optical fibers are fragile and lengthy. An appropriate container must be designed to arrange these fibers into an orderly way and protect them from being broken

Table 3-1: Properties and dimensions of Optran UV fiber.

Core	Material	Silica
	Refractive index	1.459
	Diameter	400 μm
Cladding	Material	Fluorine doped silica
	Diameter	440 μm
Jacketing	Material	Polyimide
	Diameter	480 μm
Index profile		Step index profile
Numerical aperture		0.22±0,02
Damage threshold		1.3 kW/mm^2 CW at 1064, up to 10 J, pulsed
Bend radius	Momentary	100 x cladding radius = 44 mm
	Long term	600 x cladding radius = 264 mm

during the service. As shown in Fig. 3-6, a containment ring has been designed to house the 21 fibers [Hopko, Ume, 1999]. The fibers are separated within the rigid ring in internal channels, making it possible to service an individual fiber. The containment unit is made of aluminum because it is strong and lightweight. The channel is approximately 37.7 mm by 76.2 mm (1.5" x 3"). The inside diameter is roughly 1 m.

Fig. 3-6: Fiber array container.

3.2.4 Focusing Objective

The laser coming out of a fiber is divergent and the irradiated area is a function of the distance between the fiber end and the specimen. Without a focusing lens, the fiber ends have to be close enough to the testing specimen in order to have a relatively small spot. This configuration leaves the fiber ends to be vulnerable to the ablation and the welding spatter. To solve this problem, a custom designed optical lens system – a focusing objective is utilized to focus the laser beam coming from the fibers onto the surface of the specimen. Fig. 3-7 shows the focusing objective together with the fiber phased array chuck. The focusing objective lens contributes to the physical robustness of the laser array probe by shielding the ends of the fibers from harsh welding conditions. Because the bottom face of the objective will be exposed to ablated material, fumes, heat, and welding spatter, a sapphire window is included in the design, and can be replaced or cleaned as needed. The use of the focusing objective makes it possible to generate ultrasounds in either thermoelastic regime or ablation.

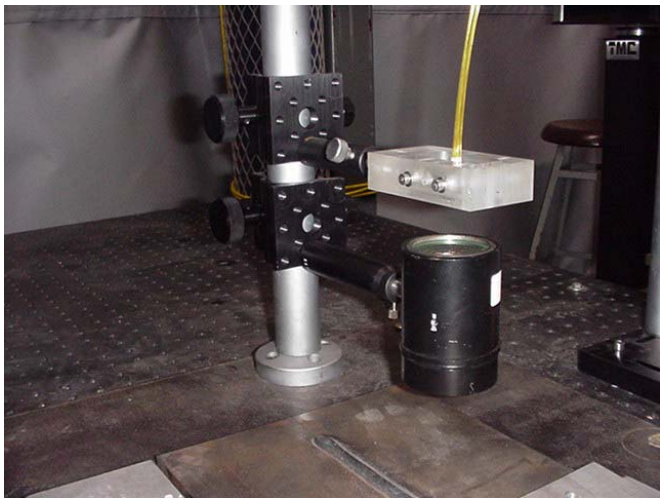

Fig. 3-7: Focusing objective with fiber chuck.

3.2.5 Laser Power Meter

The power meter is not a permanent component of the phased array subsystem. However, it is an essential tool used in array implementation and optimization. The fiber damage threshold and the laser power coming out of each single fiber are measured by the power meter so that the operation of the laser and the coupling between the laser and the fiber bundle are optimized. The laser power should be limited below the fiber damage threshold. The laser optics should be tuned and the fiber end surfaces should be carefully polished so that the laser energy is distributed into the 21 fiber bundle as uniform as possible. An accurate and consistent measurement of the laser power/energy is very important to this process. The laser power and energy meter used is model S310 from Scientech, as shown in Fig. 3-8. The meter can be configured as either a power mode or an energy mode. The power mode measures the average power (in watts or milliwatts) of repetitively pulsed lasers. The energy mode measures the energy per laser pulse or averaged energy for a selected number of pulses from 2 to 9999. In practice, the power mode is used to measure the averaged power. The average power mode measurement gives best accuracy and consistency. Eq. 3-1 - Eq. 3-3 give the conversions to obtain energy per pulse, instantaneous power, and instantaneous power density from measured average laser power.

$$\text{Energy per pulse} = (\text{Power meter measurement})/(\text{Repetition rate}) \qquad \text{Eq. 3-1}$$

$$\text{Instantaneous power} = (\text{Energy per pulse})/(\text{Pulse width}) \qquad \text{Eq. 3-2}$$

$$\text{Instantaneous power density} = (\text{Instantaneous power}) / (\text{Spot size}) \qquad \text{Eq. 3-3}$$

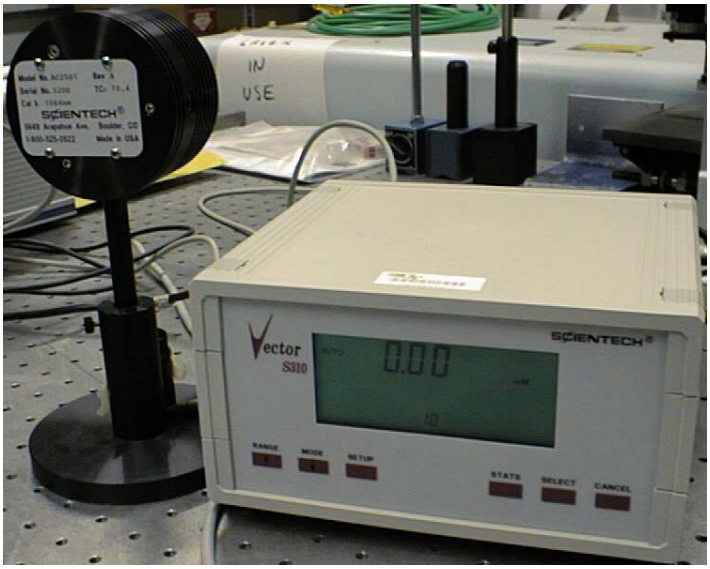

Fig. 3-8: Scientech S310 laser power and energy meter.

Fig. 3-9: Model 36-0203A Isoperibol Enclosure to isolate enviromental thermal disturbances for measuring small energies.

The laser power coming from a single fiber is in the range of 1to 10 mJ/pulse or 10 to 100 mW at the repetition of 10Hz. The measurement of the low power and energy is not stable due to the influence by environmental thermal disturbances. So an Isoperibol Enclosure (Model 36-0203A from Scientech as well, as shown in Fig. 3-9) is used to isolate the calorimeter from environmental thermal disturbances that affect the stability of

the calorimeter. Scientech recommends using this enclosure when attempting power measurements below 30 mW and single pulse energy measurements below 30 mJ. Note that the enclosure has to be removed when measuring high power/energy since overheat may occur.

3.3 EMAT RECEPTION SUBSYSTEM

3.3.1 EMAT Introduction

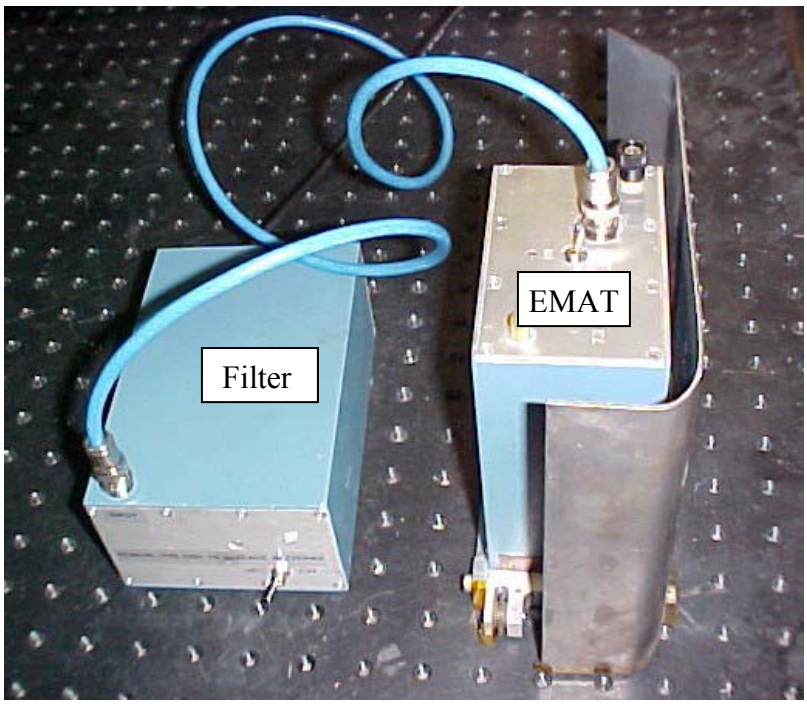

Fig. 3-10: EMAT system developed by NIST.

The EMAT used in this research was developed by A.V. Clark Jr. and S.R. Schaps of the National Institute of Standard and Technology (NIST). The EMAT system includes an EMAT assembly and a narrow band amplifier, as shown in Fig. 3-10. The

EMAT assembly detects ultrasonic waves in the metal weld plate without physical contact to the specimen (although a close proximity is required). A frame with a shield and three wheels is attached to the EMAT assembly to protect it from welding spatters and establish noncontact setup from the surface of samples to be inspected. The wheels must be electrically insulated from the EMAT assembly to block welding ground currents.

After years of service, the EMAT coils have been broken. Efforts have been made to refurbish and characterize the current EMAT so that it is optimized for the experimental setup shown in Fig. 3-1.

3.3.2 Characterization of Ultrasound with Variable Angle PZT Transducer

Fig. 3-11: Experimental setup for measuring the laser generated ultrasound at various receiving angles by a PZT with a variable angle wedge.

In order to understand the directivity pattern of the ultrasound at the receiving location, PZT transducers with variable angle wedge is used to measure the ultrasound at

different angles. The measurement setup is shown in Fig. 3-11. A half inch thick welded sample is used as an investigated medium. The focusing objective shown on the right of Fig. 3-11 focuses the laser from the phased array onto the sample surface.

The results with the setup described above are shown in Fig. 3-12 - Fig. 3-14. PZT transducers with frequency of 1.0 MHz and 2.25 MHz are used to measure the ultrasound at various receiving angles. Fig. 3-13 and Fig. 3-14 show the waveforms received by both PZTs at different angles. The results show that the ultrasound can be received by both 1.0 MHz and 2.25 MHz transducers over all the angles. The signals are refracted shear waves for angles except 90 degree (where surface wave is assumed). Fig. 3-12 shows how the ultrasonic signal strength varies along with the receiving angle.

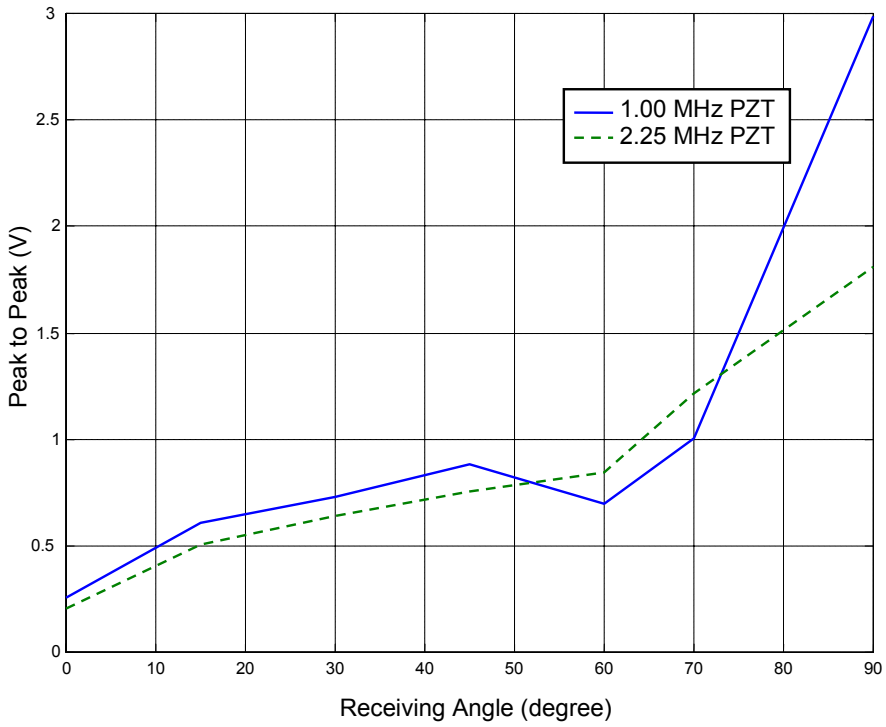

Fig. 3-12: Peak to peak value of the ultrasound at different angles.

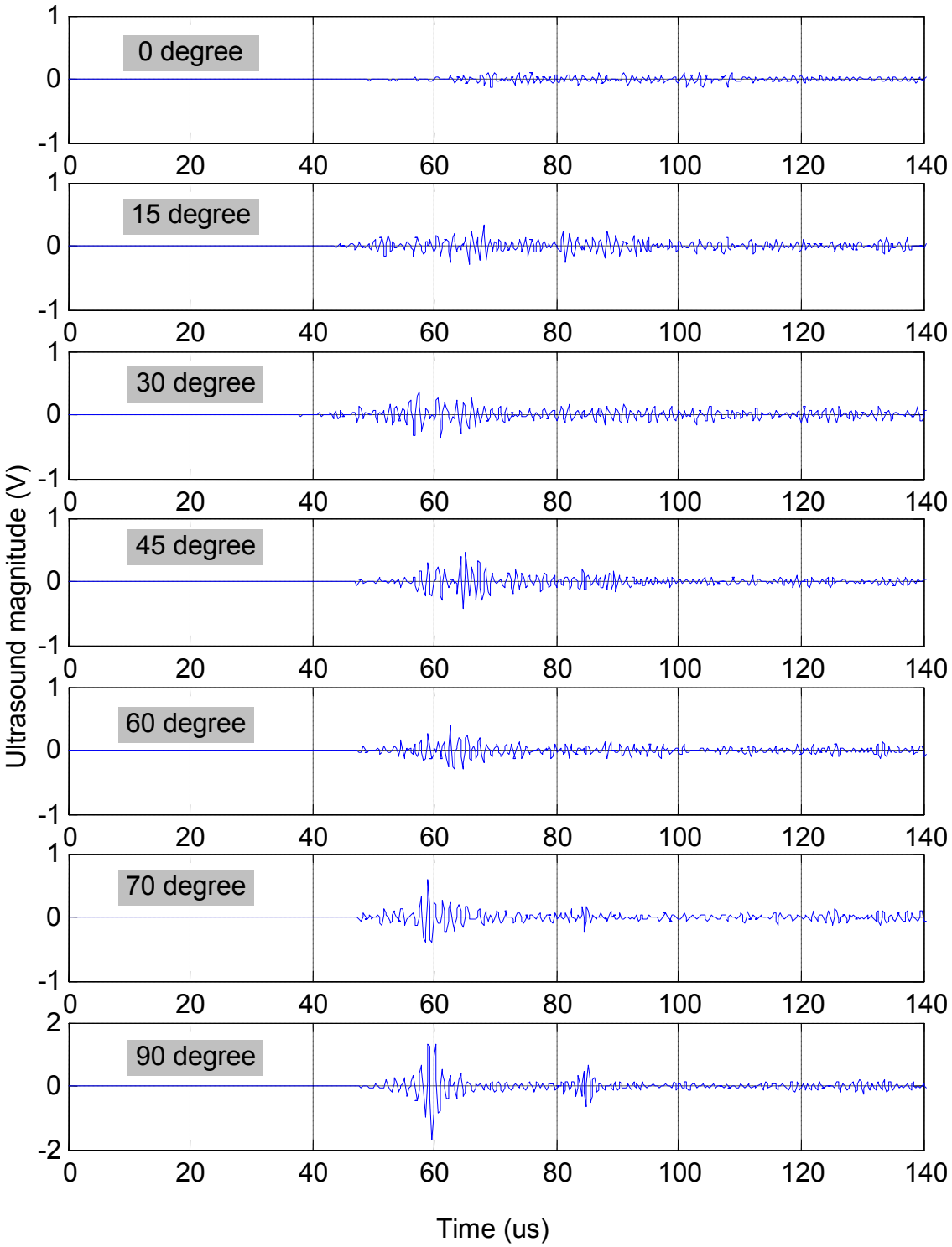

Fig. 3-13: Ultrasonic signals received by 1.0 MHz PZT at different receiving angles.

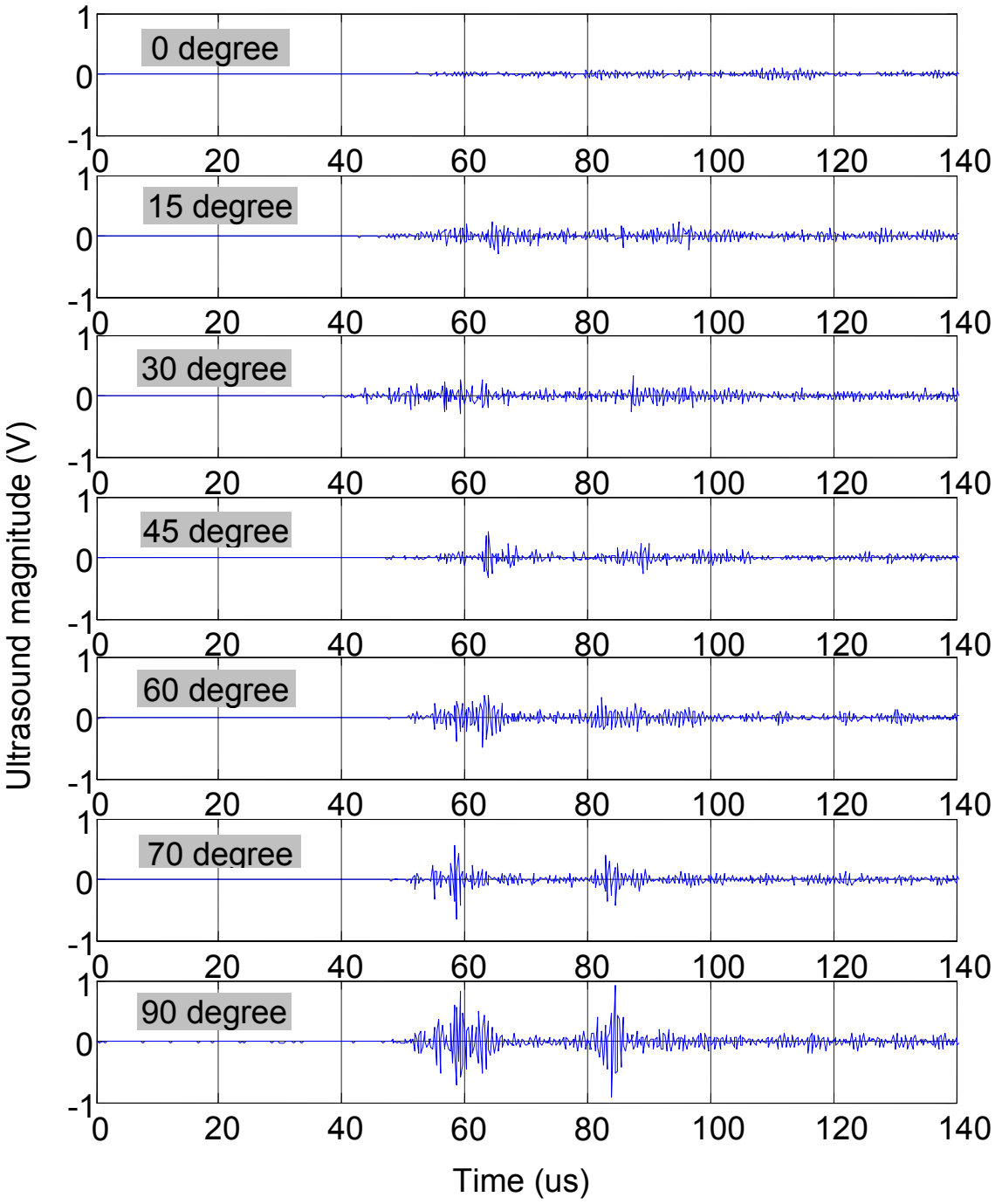

Fig. 3-14: Ultrasonic signals received by 2.25 MHz PZT at different receiving angles.

3.3.3 Refurbishment and Characterization of EMAT Unit

Based on the characterization of the ultrasound with PZTs discussed in the last section, the EMAT has been refurbished and characterized by BWXT Services, a company that builds EMAT system for various applications. The desired performance of the EMAT is that it is optimized to receive the ultrasound at large angles where the ultrasound energy focuses on.

In order to improve the sensitivity of the EMAT as a receiver for the detection of laser generated ultrasound for measuring the depth of weld penetration, a new coil with dual rectangular design has been proposed. This EMAT coil design is for maximizing the sensitivity of the receiver.

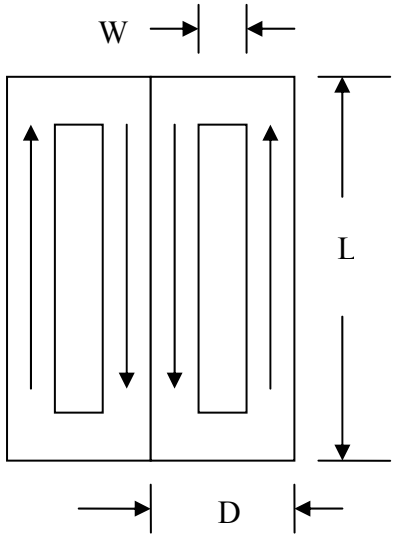

Fig. 3-15: EMAT coil shape and dimensions.

Fig. 3-15 shows a plane view of the proposed EMAT coil. D and W are determined by the desired ultrasonic reception properties. L is determined by the available magnetic field and transducer aperture considerations.

The refurbished EMAT is characterized by BWXT Services and the results for both longitudinal wave and shear wave are provided, as shown in Fig. 3-17 and Fig. 3-16 respectively. The longitudinal wave measurements have a little more scatter in it because a conventional piezoelectric transducer is used to launch the ultrasound and there could be variations in the coupling. The shear waves are generated with an EMAT and are more reproducible. The shear wave response peaks at 35 to 40 degrees then plunges to a minimum at 45 degrees. The rapid oscillation in the response between 45 and 60 degrees is due in part to an interfering reflection signal of unknown origin.

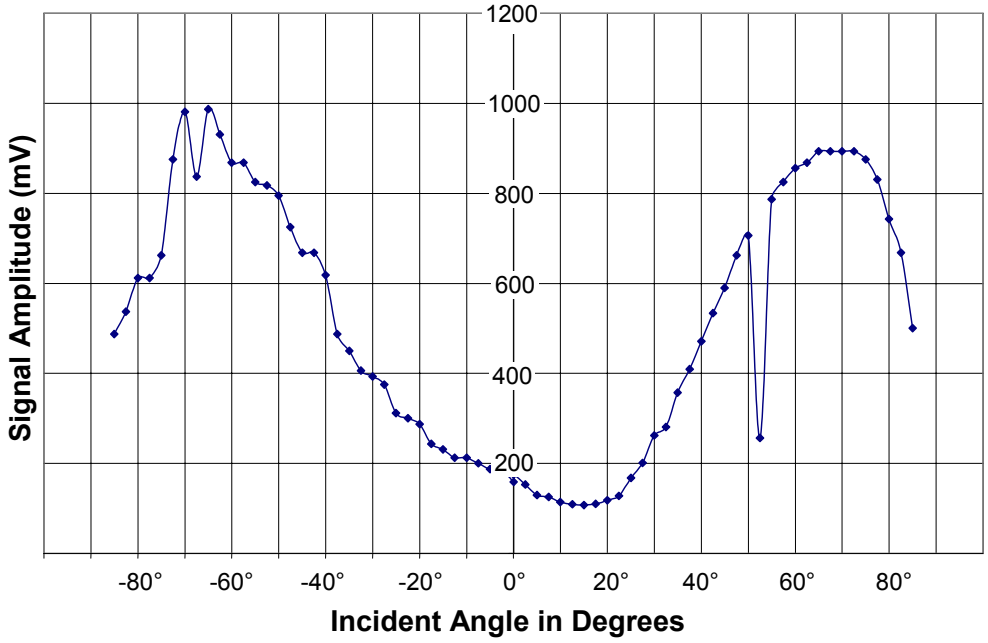

Fig. 3-16: EMAT response to incident 1.0 MHz longitudinal waves.

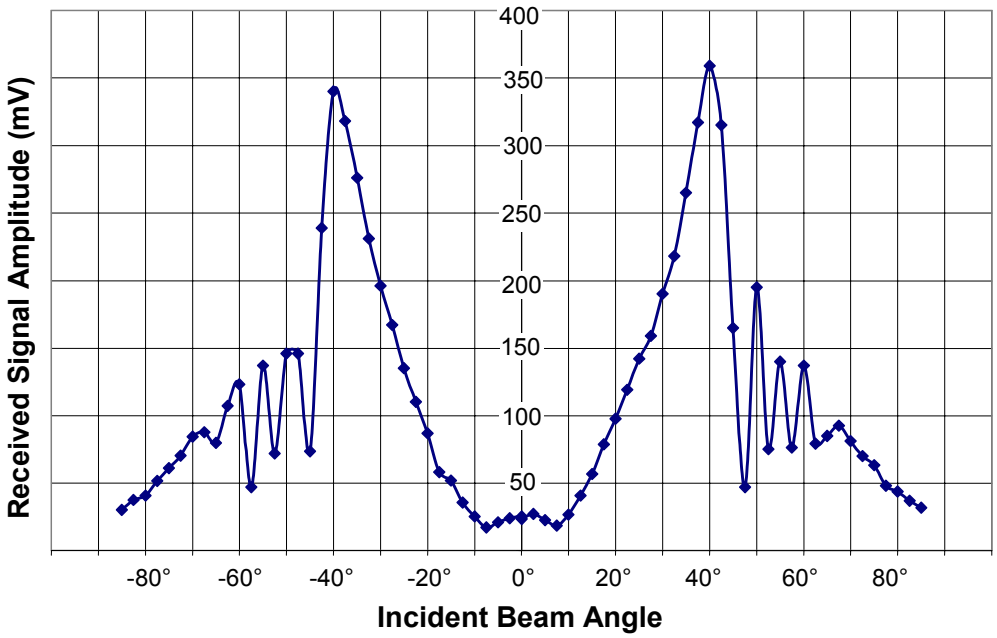

Fig. 3-17: EMAT response to 1.0 MHz shear waves.

It is proven that the EMAT is successful in receiving shear waves in welding environment and it has good EMI noise rejection if it is properly grounded.

3.4 Computer Acquisition System

A PC with a GaGe high-speed 6012 PCI A/D board serves as the main center of data acquisition and processing. The 6012 PCI A/D card has 12-bit resolution and is capable of sampling data at 60 MHz in single channel mode or 30 MHz in dual channel mode. This A/D card system is used to acquire the ultrasonic signals received by the EMAT as well as the trigger signal from the laser controller at a sampling rate of 10 MHz per channel.

The Continuum SureLite II Nd-YAG laser used in this research can be operated through RS-232 or TTL interface. In order to coordinate the robot controller, laser, and the acquisition system, an interface controller is designed to communicate between the laser and robot controllers. The interface controller is implemented with PIC microcontroller (PIC16F84). It detects the handshaking signal from the robot controller that indicates when welding begins and ends and then sends ASCII commands to laser power supply unit through RS232 interface to start and stop the laser firing. The flow chart of the controller's operation is shown in Fig. 3-18.

The acquisition software was developed with Labview, a graphical development environment for signal acquisition, measurement analysis, and data presentation. A screen shot of the software interface is shown in Fig. 3-19. The program first presets the system and waits for the trigger signal from the laser power supply. When the robot is in position to begin the welding process, the robot controller sends out the handshaking signal. This handshaking signal is monitored by the designed controller. The laser is turned on and off based on the indication of the handshaking signal. Once the laser is turned on, the acquisition of the ultrasonic signal starts and repeats at the laser firing rate.

In the data acquisition loop, the program receives a trigger signal from the laser controller and ultrasonic signals from the ultrasonic receiver. The acquisition of a single waveform starts with the trigger signal and ends after a specified number of samples (specified by user) are taken. A time lead or lag can be configured between the trigger signal and the start of the acquisition. Once the data collection is complete, the program stores the time that the trigger signal was received and the ultrasonic data in two separate files on the computer, which are analyzed offline afterwards. The program awaits the

next trigger signal from the laser and repeats the data acquisition and storage process. At the end of the welding process, the interface controller receives a handshaking signal from the robot controller and it acquires ultrasonic signals for another 15 seconds, and then turns off the laser emission and exits the data acquisition loop.

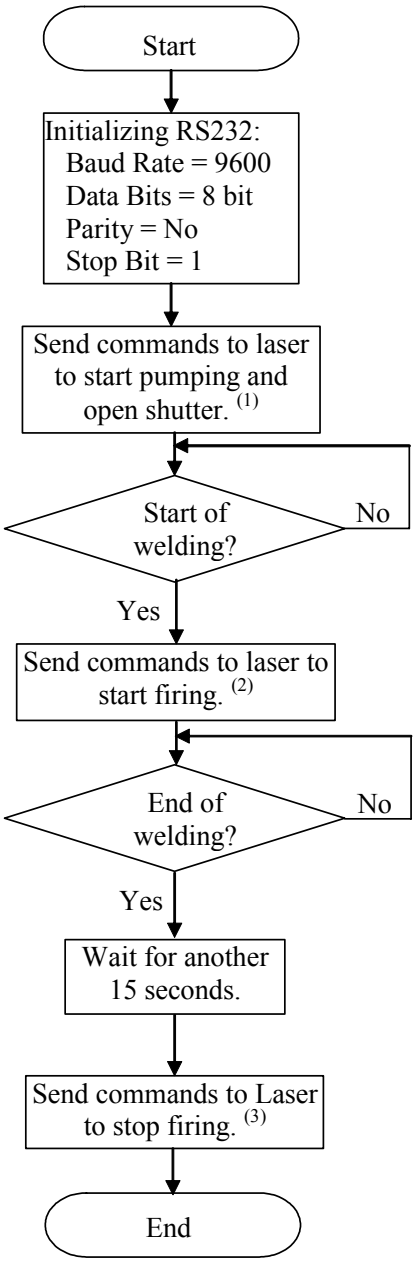

ASCII Commands Used

(1). Commands to start laser pumping:
ST 1 (start pumping);
SH 1 (open shutter);

(2). Commands to start laser firing:
PD 001 (start firing at 10Hz).
This command has to be issued no sooner than 1 second after the "open shutter" command is issued.

(3). Commands to stop firing:
PD 000

Fig. 3-18: Flow chart of interface controller.

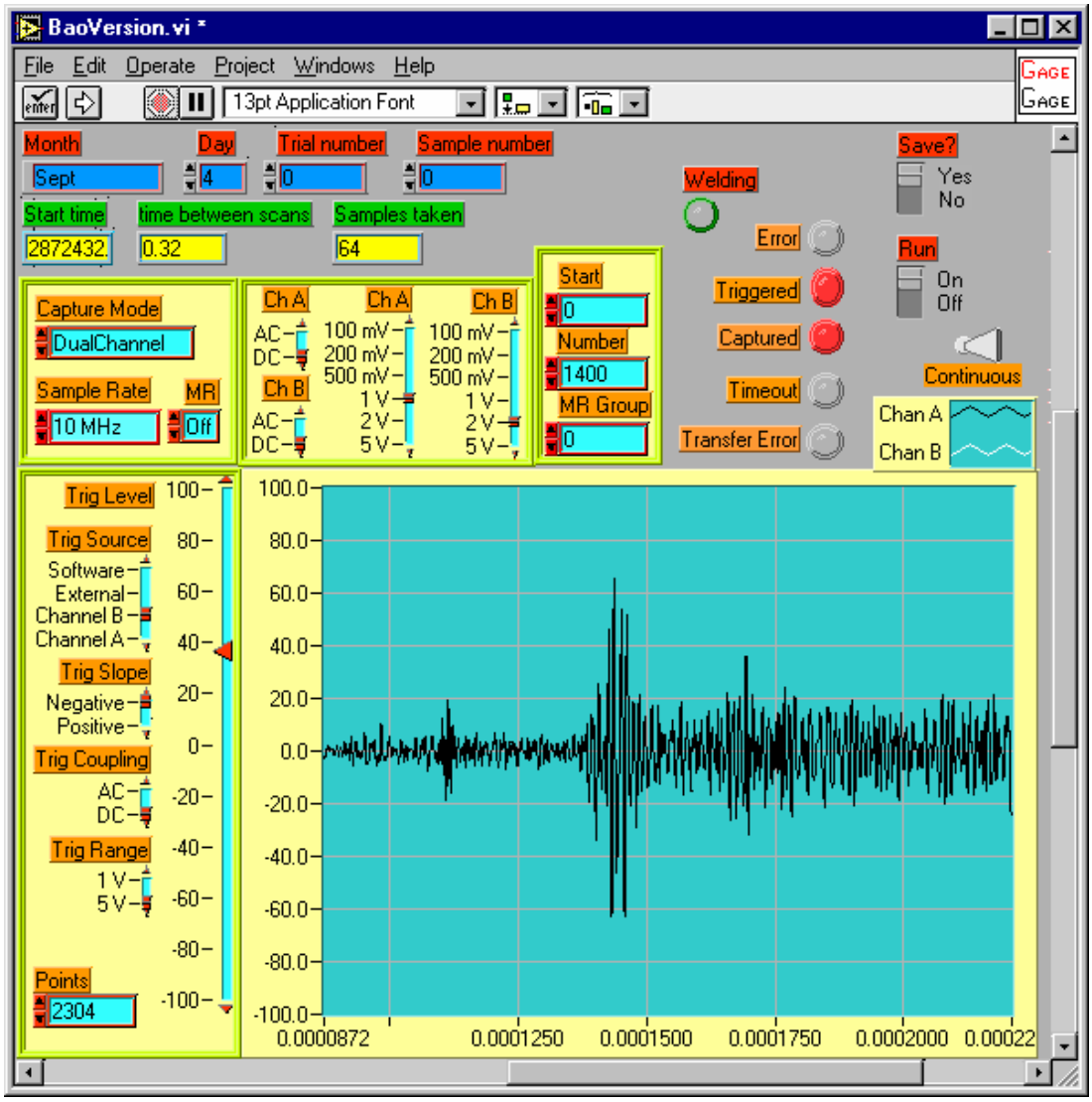

Fig. 3-19: Acquisition software interface developed in Labview.

3.5 Other Apparatus

3.5.1 KH3945 Filter/Amplifier

The KH3945 filter/amplifier shown in Fig. 3-20 is used to further filter and amplify the noisy signals from the EMAT receiver. This unit is manufactured by Krohn-

Hite Corporation. The Krohn-Hite Model 3945 is a multi-channel, Butterworth/Bessel filter with three channels. It offers a programmable filter covering a cutoff range from 3Hz to 25.6MHz, with a frequency response characteristic of maximally flat (Butterworth) for clean filtering in the frequency domain, or linear phase (Bessel) to provide superior pulse or complex signal filtering.

Fig. 3-20: Krohn-Hite Model 3945 Filter/Amplifier.

The Krohn-Hite filter is configured as a band pass filter with the selecting frequency range of 500 KHz to 750 KHz. This frequency range is found by try and error method. The amplifier was set to 20 dB amplification.

3.5.2 PZT Transducers

Angle beam transducers use the principles of refraction and mode conversion to produce refracted shear or longitudinal waves in the test material as shown in Fig. 3-21.

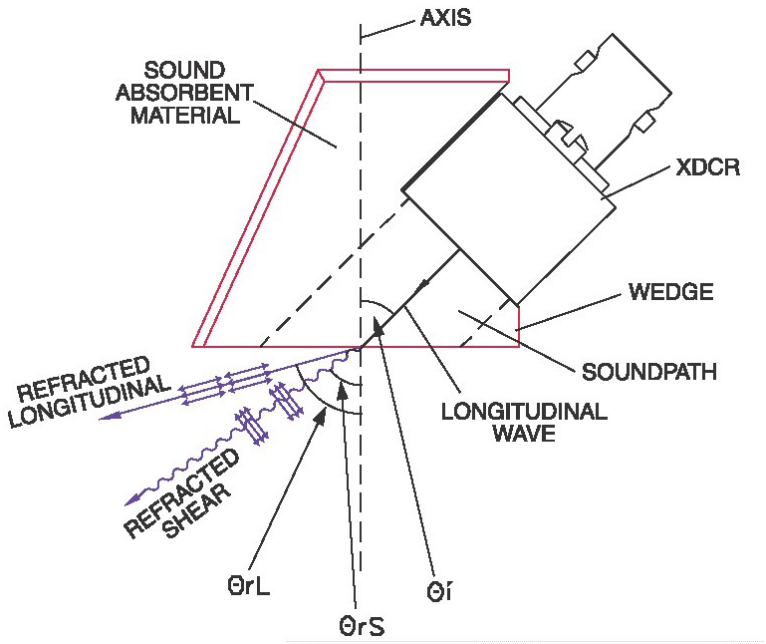

Fig. 3-21: Operating principle of an angle beam PZT transducer.

High temperature wedges are available for welding application. However, long term use in high temperature environment is not recommended even for the high temperature wedges because the heat will be transferred to the transducer after the wedge is exposed to the high temperature for an extended period of time.

The angle beam PZT is connected to a MR101 receiver in a Tektronix TM503B main frame. The PITCH/CATCH mode is used so that MR101 only receives ultrasonic signals without excitation.

CHAPTER IV

IMPLEMENTATION AND ANALYSIS OF FIBER PHASED ARRAY

The principle of a phased array is briefly presented in Chapter II and the components utilized to construct the phased array generation unit are discussed in Chapter III. In this chapter, the implementation of the fiber phased array into the weld penetration depth monitoring system and analysis of the fiber phased array performance are discussed in detail.

4.1 Optimal Coupling of Laser Light into Fiber Bundle

4.1.1 Fixture Design

The fibers at the laser end are configured as a circular bundle. Handling 21 fibers with polyimide jacketing removed is a very difficult task. Great care must be taken not to break the bare fibers. As shown in Fig. 4-1, a fixture is designed to hold the 21-fiber bundle so that the fibers are free of stress and the bundle is not yet loose. A tube-like fiber holder is designed to configure the fibers into a circular bundle. The fiber holder is placed in a fiber clamp purchased from Newport Corporation. The clamp slips over the end of the fiber holder and grips fibers and the tube. Then the tube and the clamp are attached to an X-Y Positioner so that it can be easily aligned to the laser beam.

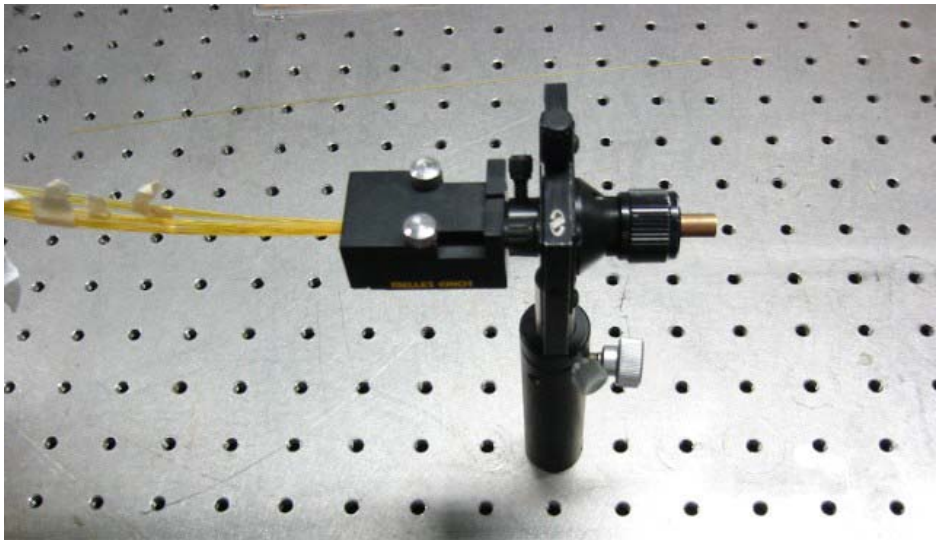

Fig. 4-1: Fiber chuck at the laser end.

The inner diameter of the tube holder is determined in such a way that it holds the 21 fibers without causing stresses or strains on the fibers. The minimum diameter of the fiber bundle can be found in AutoCAD by virtually arranging the 21 fibers in a drawing, as shown in Fig. 4-2. The actual tube size is a little bit larger than what was found from AutoCAD and it is determined by try-and-error method. A series of holes are drilled with the diameters around the value determined by AutoCAD, and the right dimension is chosen by trying 21 fibers into the holes. Fig. 4-3 shows the actual tube design.

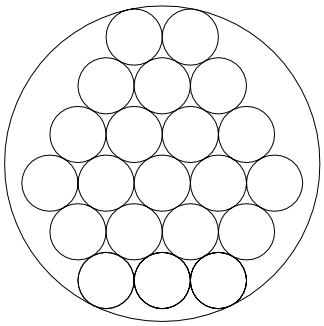

Fig. 4-2: Using AutoCAD to find out the smallest circle size to hold 21 fibers. The tube diameter is 2.47 mm with the fiber diameter of 0.44 mm.

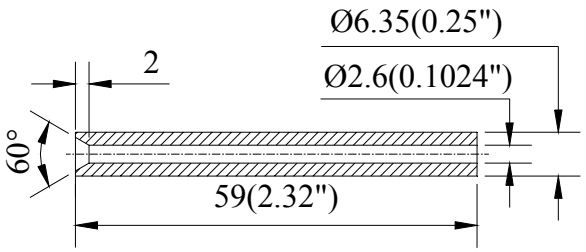

Fig. 4-3: Fiber bundle holder tube.

4.1.1 Laser Tune-up

The laser needs to be tuned very carefully to get rid of "hot spots" and achieve a better uniformity in its spatial distribution. This is critical to ensure an even distribution of laser energy over the fiber bundle. If the laser optics is not properly tuned, the energy distribution over the laser beam could be asymmetric and non-uniform. Fig. 4-4 shows the laser profiles recorded by a thermal sensitive paper. The brighter color means higher laser power energy.

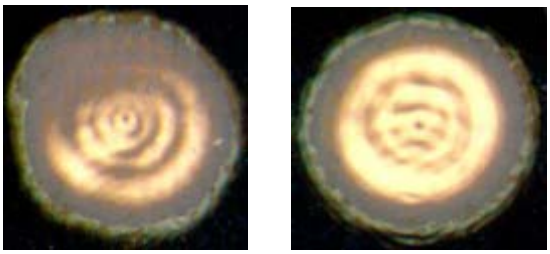

(a) (b)

Fig. 4-4: Laser profile on a thermal sensitive paper. (a) Before laser was tuned; (b) After laser was tuned.

4.1.2 Fiber End Preparation

The advantages of delivering light through optical fibers for laser generation of acoustic waves include flexibility and the possibility of achieving virtually any desired source configuration. However, since high optical power density (often of the order of 10^7 W/cm^2 or more for ablation) is required for efficient ultrasound generation, the implementation of the fiber optic delivery is not an easy task to perform.

Particular care must be taken in preparing the fiber surfaces and constructing the bundle. The fiber end preparation includes cleaving and polishing. The quality of the end preparation has a large effect on the amount of energy transmitted. For example, an imperfect cleave (chip on the edge) results in loss of surface area for launching the light into the fiber. End finish also affects the fiber damage threshold. At the laser end, the polyimide jacketing is dissolved by placing the end of the fiber in a hot solution of sulfuric acid. Care must be taken that no residue is left on the fiber: residue causes the fiber to fail even at low laser power. After the removal of the polyimide jackets, the individual fibers are cleaved and then polished with an initial 15 μm aluminum oxide grit followed by a 3 μm grit. After all of the fiber ends are carefully prepared, they are aligned and arranged into the tube holder.

4.1.3 Laser Energy Distribution among the Fiber Bundle

First of all, the 21 fibers are coded with different colors for three different sources. The 2 m fibers are coded as red, 52 m fibers as green, and 102 m fibers as blue. In each source, the 7 fibers are numbered so that they can be identified during the measurement.

Fig. 4-5 shows the actual arrangement of the 21 fibers in the circular bundle. The distribution of the 21 fibers at the laser end is randomly arranged. After the fibers are chucked at the laser end, each individual fiber can be identified by watching them through a magnifier, and blocking the light coming in a particular fiber from other end. When the fiber is blocked from other end, it becomes dark in the circular bundle and its location is identified.

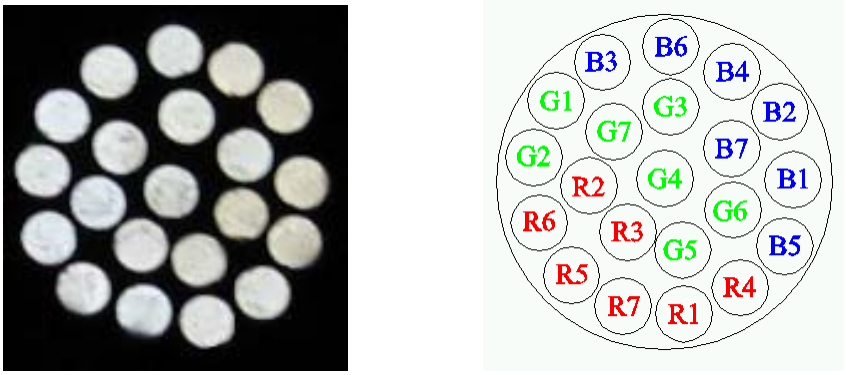

(a) (b)

Fig. 4-5: Arrangement of fiber bundle at the laser end. (a) Picture taken through a magnifier. (b) Illustration of the coded and numbered fibers in the circular bundle.

The output powers from each of the 21 fibers have been measured by the laser power meter described in Section 3.2.5 to evaluate the coupling performance. Fig. 4-6 shows the results for two cases: before and after the laser is tuned. The results show that the tuning of the laser makes a big difference in both the magnitude and the uniformity of the laser energy coupled into and delivered by the 21 fibers.

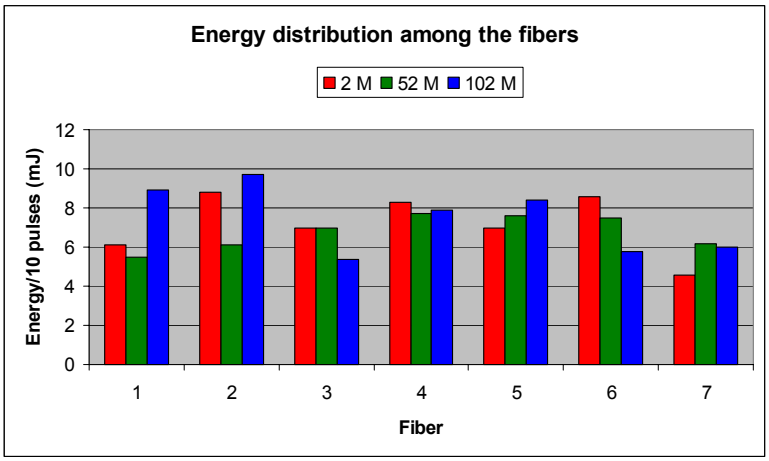

(a)

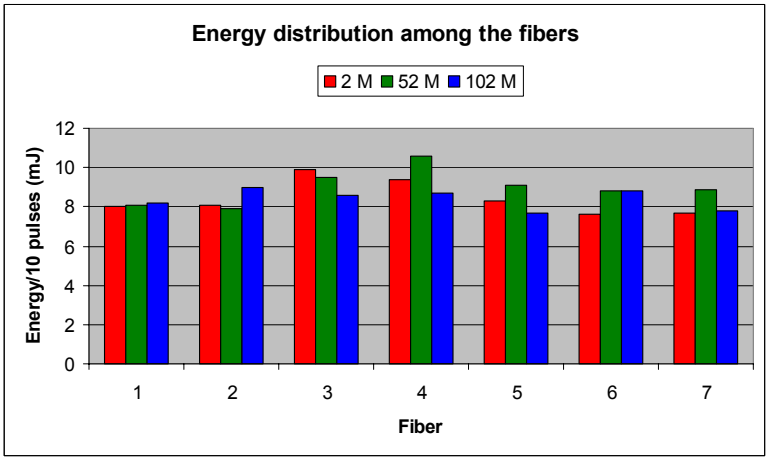

(b)

Fig. 4-6: Laser power distribution among the 21 fibers of the phased array. (a) Before laser is tuned. (b) After laser optics is tuned.

4.2 Fixture at the Distal End

A robust fixture at the distal end of the phased array is mandatory to attach the fibers and the focusing objective lens together. With the designed fixture, the following

parameters should be adjustable: 1. the distance between the fiber ends and the lens surface; 2. the distance between the three fiber line sources. The first parameter is used to make the unit capable of generating ultrasounds in either thermoelastic or ablative regime, as the task may demand. The inter-element spacing of the fiber phased array is one of the parameters to control the steered angle of the ultrasonic waves.

Fig. 4-7: Fixture at the distal end.

4.3 Calibration of Phased Array Timing

The designed time lag between the phased array sources is 0.246 μs based on Eq. 2-8. To verify this value, the timing of the fiber phased array is measured with a simple circuit shown in Fig. 4-8. An attenuator is used to limit the laser energy coupled into the photo transistor.

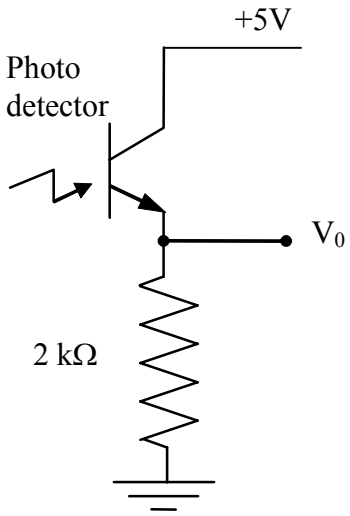

Fig. 4-8: Circuit to detect the laser timing.

The laser outputs from the fibers of the three line sources are monitored with the circuit shown in Fig. 4-8. A real-time digital oscilloscope is used to acquire and record the output V_0 with a sampling rate of up to 100 MHz. The Fixed Sync Out from the laser power supply is used to trigger the oscilloscope. Fig. 4-9 shows the measurements of the outputs for the three phases and the bare laser. The rising edge represents when the laser energy is received. Although the laser energy is a very short pulse, the signals received by the photo transistor show a step function. The reason is that the photo transistor is saturated by the laser energy and the photo transistor remains on for quite a while even after the laser pulse is cut off. The peak on a signal appeared right after the rising edge is considered as the laser pulse peak. This can be verified by the fact that the peak of the bare laser, which measures at $t = 0.167 \mu s$, agrees well with the value of $0.170 \mu s$ given by the laser operation manual.

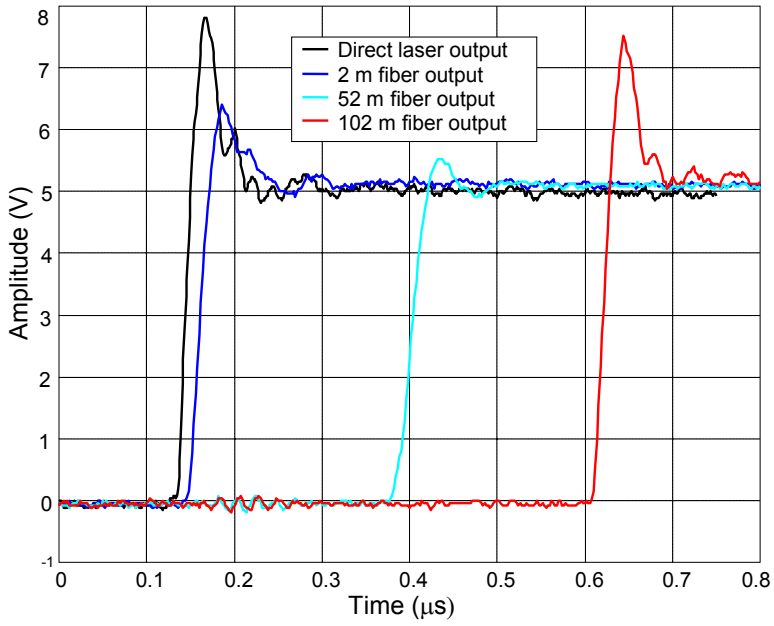

Fig. 4-9: Measured timing of laser outputs from three fiber phases and directly from laser.

When peak value is used, the time delay between the output directly from laser and the output from 2 m fiber is $\tau_0 = 0.02\mu s$. The time lags between the outputs from the different phase sources are shown in Table 4-1. The discrepancy between the designed value and the measure value could be caused by the measurement and the fiber length.

Table 4-1: Time lags between the three phases of the fiber phased array.

Time lag	Designed value (μs)	Measured value (μs)	Error (%)
Between 2 m fibers and 52 m fibers: τ_1	0.243	0.246	1.2
Between 52 m fibers and 102 m fibers: τ_2	0.243	0.212	-12.7

4.4 FIBER PHASED ARRAY ANALYSIS

The goal of the phased array is to steer the generated ultrasounds to the desired direction where the receiver is aligned. The steering behavior of the ultrasound generated by a phased array is predicted by Eq. 2-7, which can be used as a theoretical guideline for the phased array design and optimization. Note that the steering angle ϕ is not the direction in which the maximum ultrasound will be received. The resultant ultrasonic directivity pattern will be the product of the one generated by a single source and the array factor $I_a(\theta,\phi)$. The shear wave and the longitudinal wave are optimized at different directions with the same phased array configuration because the steering angle is wavelength dependent. Thus, the phased array has to be optimized based on the ultrasonic wave type, frequency, etc.

The directivity pattern is usually plotted in a polar coordinate system and the same propagation distance for any angle is assumed. This kind of plot can be obtained experimentally by using a semi-cylinder. However, the polar representation of directivity pattern will only give a rough idea of how the phased array works for the source/receiver configuration shown in Fig. 4-10. The situation in this application is more complicated than in the case with a semi-cylinder. First, the ultrasounds propagating along the different angles travel different distances before they are picked up by the receiver. So, when designing and optimizing the phased array, attenuation as a function of distance has to be taken into account. Second, both reflection and diffraction are angle (and hence location) dependent. Third, the receiving angle changes along the measuring locations and the receiver directivity will contribute to the measured results. As shown in Fig. 4-10, weld penetration depth *D* varies from the sample thickness to a smaller value (the

extreme case is $D = 0$). The corresponding angle θ varies from a certain angle θ_{min} to the extreme case 90°. The best signal strength can be obtained if the phased array can be designed and optimized so that most of the ultrasound energy will fall within this angle range.

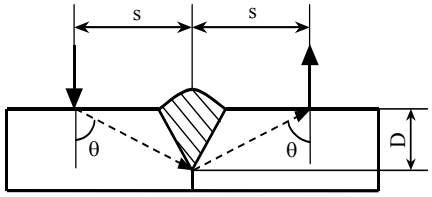

Fig. 4-10: Configuration of source and receiver.

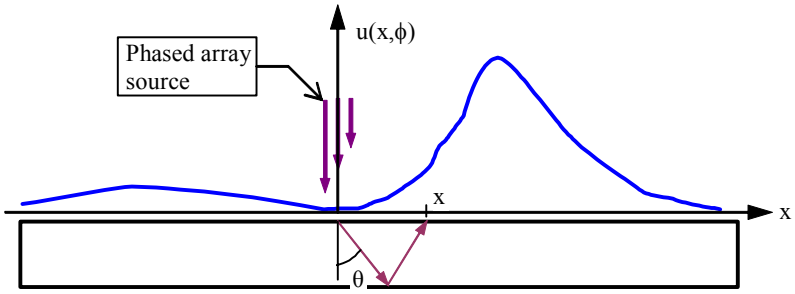

Fig. 4-11: Schematic of Cartesian representation of the directivity pattern.

When plane wave is assumed, the geometrical ray theory can be applied to derive the equations for calculating the ultrasound arrival strength. Assuming single reflection (or diffraction), the ultrasound received at different location can be expressed by Eq. 4-1.

$$u(x) = T(x)A(x)r(x)R(x) \qquad \text{Eq. 4-1}$$

where *T(x)* and *R(x)* are the source and receiver functions, *A(x)* takes into account distance dependent attenuation, and *r(x)* is the reflection (diffraction) coefficients. A similar approach has been adopted by some other researchers [Scruby, *et. al.*, 1986].

4.4.1: Phased Array Source Function

The ultrasound component along certain angle θ will bounce back based on the reflection law when it reaches the bottom and gets to the upper surface at the position x and then picked up by a receiver. When a Cartesian plot shown in Fig. 4-11 is used to predict and evaluate the phased array performance, the ultrasound receiving location x needs to be mapped to angle θ at which the ultrasound is generated and received. This mapping $\theta(x)$ can be simply derived by geometric analysis, as shown in Eq. 4-2.

$$\theta(x) = \tan^{-1}\left(\frac{x/2}{D}\right) \qquad \text{Eq. 4-2}$$

Plugging Eq. 4-2 into Eq. 2-6 gives the Cartesian representation of the directivity pattern $T(x)$ of the phased array source, which is the source function with respective to the location x as shown in Eq. 4-3.

$$T(x) = u_e(\theta(x)) \cdot I_a(\theta(x), \phi) \qquad \text{Eq. 4-3}$$

Fig. 4-12 and Fig. 4-13 show the comparison of the polar and Cartesian representation of the directivity pattern (analytical results) of an ablation phased array source.

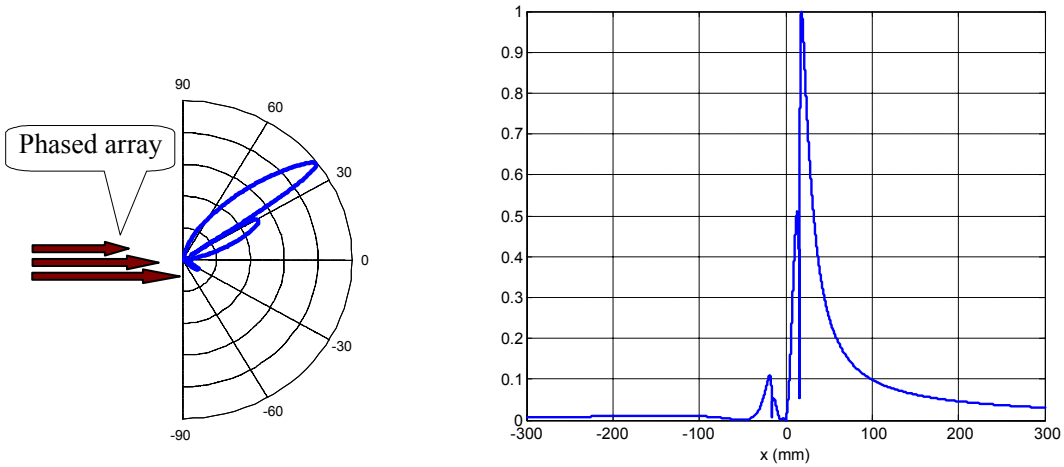

(a) (b)

Fig. 4-12: Directivity pattern of an ablative phased array source for shear wave (d = 1.5 mm, f = 1MHz). (a) Polar representation; (b) Cartesian presentation for D = 12.7 mm.

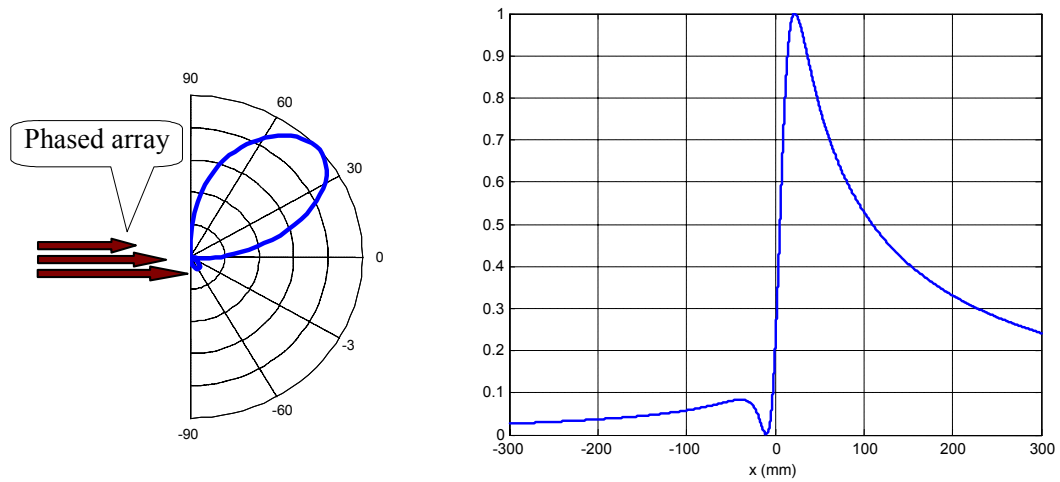

(a) (b)

Fig. 4-13: Directivity pattern of an ablative phased array for longitudinal wave (d = 1.5 mm, f = 1MHz). (a) Polar representation; (b) Cartesian presentation for D = 12.7mm.

4.4.2: Attenuation Factor

Earlier research results show that the laser-ultrasonic attenuation is exponential along the propagation path and dependent on the material microstructure and ultrasound wavelength [Aussel and Monchalin, 1989; Scruby, Smith and Moss, 1986]. The exponential attenuation is expressed by Eq. 4-4, where K is a constant determined by the material property.

$$A(x) = \exp\left(-K\frac{2D}{\cos(\theta(x))}\right) \qquad \text{Eq. 4-4}$$

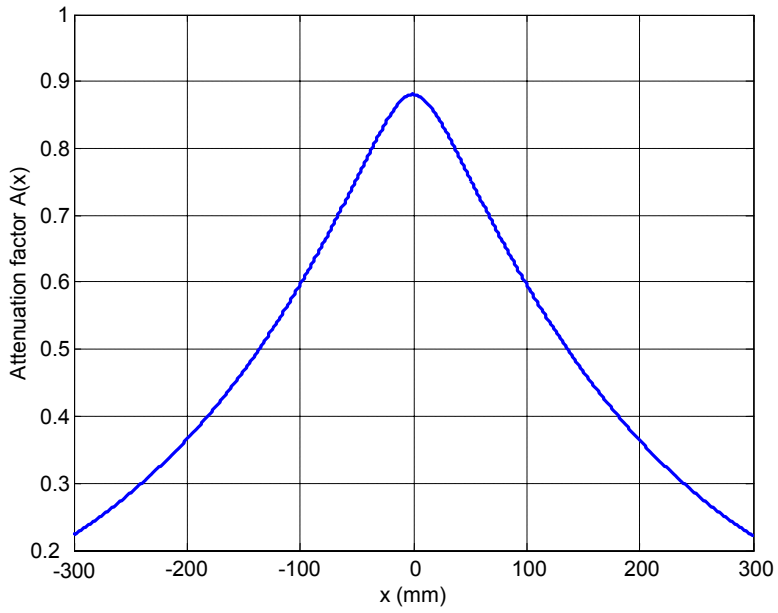

Fig. 4-14: Exponential attenuation factor.

4.4.3: Reflection Coefficients

The coefficients for the reflection of plane longitudinal (Eq. 4-5) and shear waves (Eq. 4-6) from a plane solid-vacuum boundary are given by Scruby [Scruby *et al*, 1986].

$$R_{PP} = \frac{4\sin^2\theta\sqrt{1-\sin^2\theta}\sqrt{k^2-\sin^2\theta}+(k^2-2\sin^2\theta)^2}{(k^2-2\sin^2\theta)^2+4\sin^2\theta\sqrt{1-\sin^2\theta}\sqrt{k^2-\sin^2\theta}} \quad \text{Eq. 4-5}$$

$$R_{SS} = \frac{4\sin^2\theta\sqrt{1-\sin^2\theta}\sqrt{1-k^2\sin^2\theta}-k(1-2\sin^2\theta)^2}{k(1-2\sin^2\theta)^2+4\sin^2\theta\sqrt{1-\sin^2\theta}\sqrt{1-k^2\sin^2\theta}} \quad \text{Eq. 4-6}$$

where,

R_{PP} : Reflection coefficient for longitudinal waves

R_{SS} : Reflection coefficient for shear waves

$k = \frac{c_L}{c_S}$: Ratio of the longitudinal wave velocity to the shear wave velocity

θ : Angle measured away from surface normal

4.4.4: Receiving Sensitivity as a Function of Angle

The receiving sensitivity of the EMAT is made available by BWXT Services who has characterized the EMAT. Both 1.0 MHz longitudinal and shear wave are measured and shown in Fig. 3-16 and Fig. 3-17.

4.4.5: Experimental Measurement with EMAT

The ultrasound is measured by an EMAT to evaluate the phased array generation source with the configuration shown by Fig. 4-15. Ultrasound is generated in a 12.7 mm thick steel plate by the phased array, and measured by an EMAT at different locations along x direction. Due to the size of the phased array generation (especially the focusing

objective), the EMAT does not have access to the vicinity of the ultrasound generation point. The measurements are made in the range of $69mm \le |x| \le 250mm$, where the phased array – EMAT distance will be. Fig. 4-16 shows the typical ultrasonic waveforms at different locations. It shows that the ultrasound is much stronger at one side than the other. This is the results from the steering effect of the phased array generation. Fig. 4-17 gives the comparison between theoretical and experimental measurements of ultrasonic signal strength in a plate. The magnitude is scaled so that they can be compared. At the measuring range, the theoretical prediction matches the experimental measurements very well.

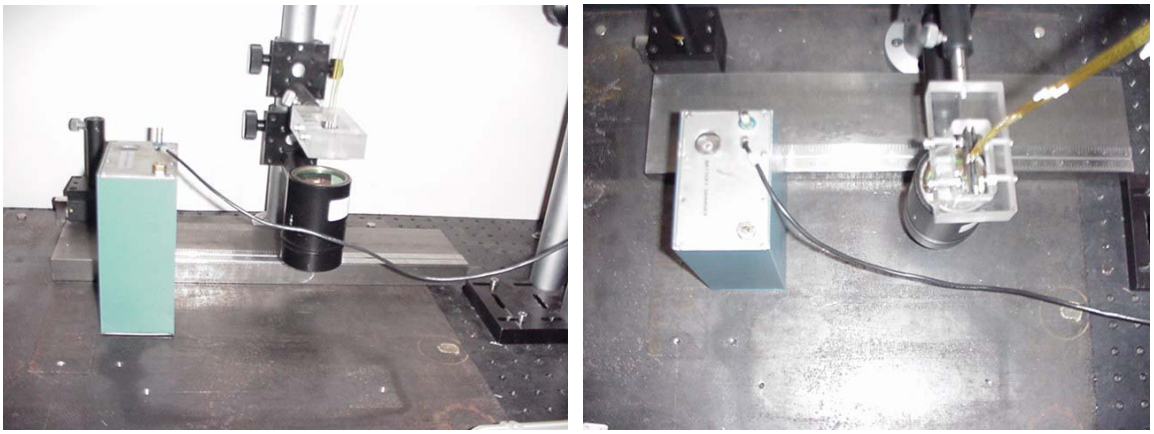

(a) (b)

Fig. 4-15: Setup for measuring strength along the base. (a) Side view. (b) Top view.

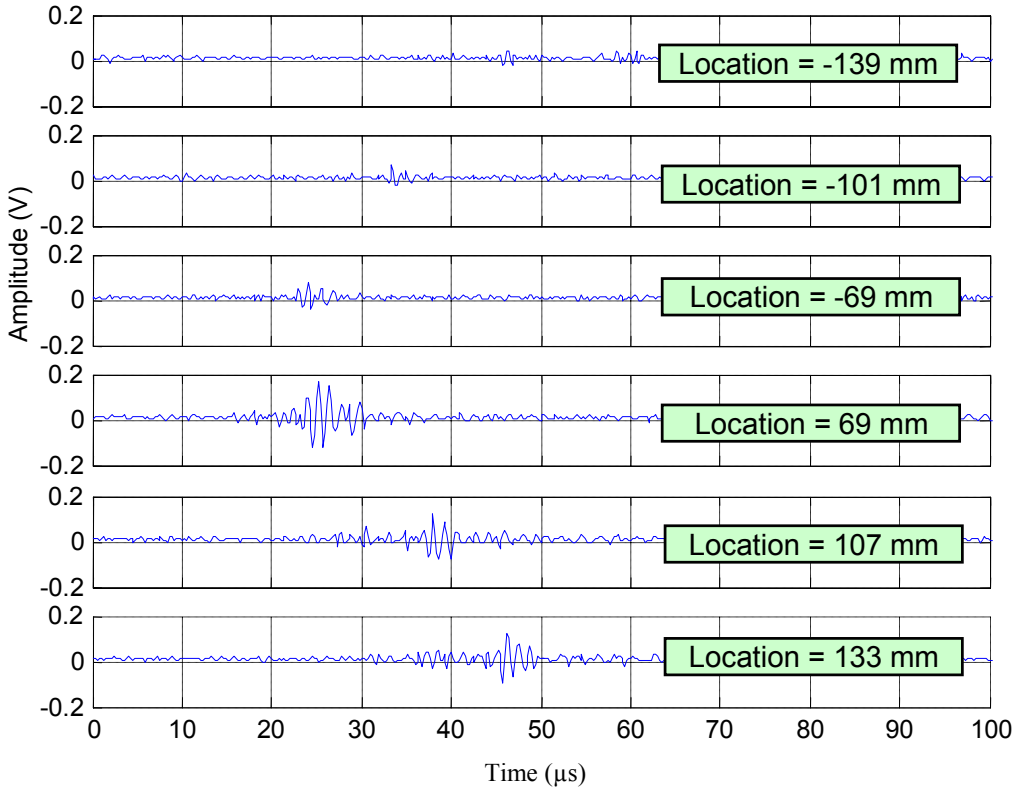

Fig. 4-16: Ultrasonic signals received at different locations.

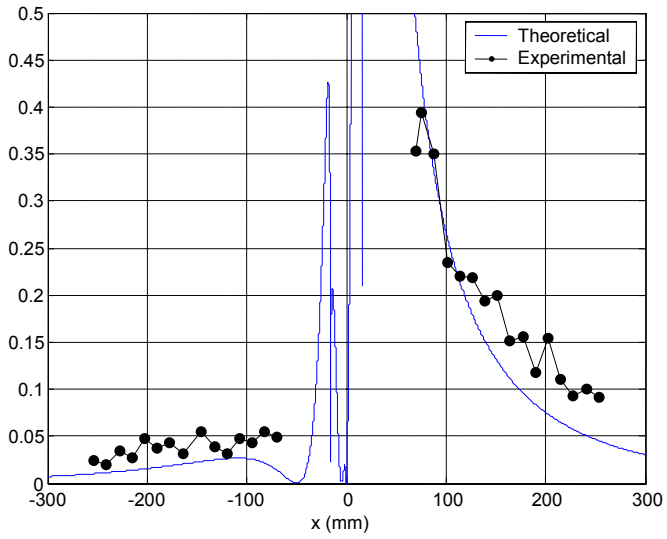

Fig. 4-17: Comparison between theoretical and experimental measurements of ultrasonic signal strength in a plate (ablation, shear wave).

4. 5 INFLUENCE OF THE SINGLE LINE SOURCE SIZE

The fiber phased array is implemented with three line sources. Each of the three line sources is composed of 7 single 400 μm silica fibers shown in Fig. 4-18.

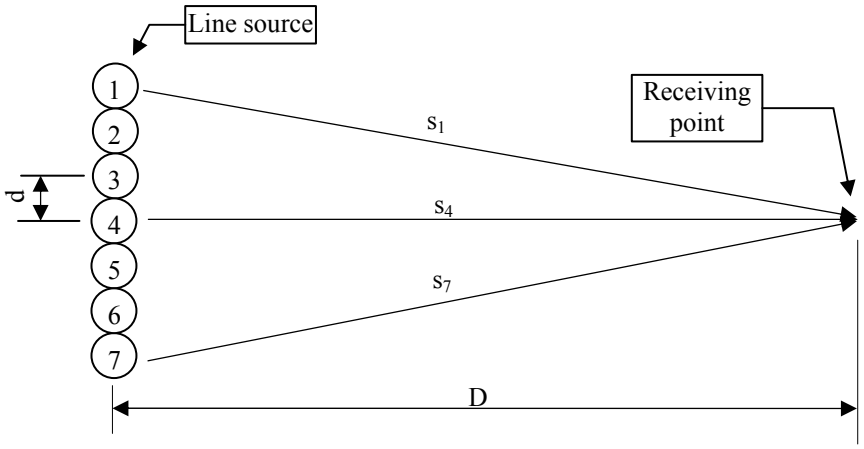

Fig. 4-18: Configuration of the single line source.

Strictly speaking, the ultrasounds generated from each source propagate along the slightly different distances before they reach the receiving point. In order for the ultrasonic fields generated from each of the 7 fiber sources to reinforce at the receiving location, the phase difference introduced by the different propagation path for each source must be significantly small. This can be guaranteed if the maximum propagation path difference is significantly small compared to the ultrasound wavelength.

For the shear wave with the propagation velocity of 3240 m/s, the ultrasound wavelength ranges from 0.162 mm to 6.48 mm for the frequency range of 0.5 MHz to 20MHz. For the longitudinal wave with the propagation velocity of 5960 m/s, the wavelength ranges from 0.30 mm to 11.92 mm. With the configuration shown in Fig. 4-18, the ultrasounds generated from fibers 1 and 7 travel the longest path to reach the

receiving point and fiber 4 travels the shortest. The path lengths for all of the 7 individual sources can be calculated by Eq. 4-7.

$$\begin{aligned} s_1 &= s_7 = \sqrt{D^2 + (3d)^2} \\ s_2 &= s_6 = \sqrt{D^2 + (2d)^2} \\ s_3 &= s_5 = \sqrt{D^2 + (d)^2} \\ s_4 &= D \end{aligned} \qquad \text{Eq. 4-7}$$

where,

d: single source diameter;

D: source-receiver distance;

$s_1 - s_7$: Ultrasound propagation path for seven fiber sources.

With D = 50 mm, and d = 0.25 mm (The laser spot incident on the sample surface has a diameter of half of the fiber's after the 0.5X focusing objective), the biggest difference in propagation paths is $s_1 - s_4 = 50.0056 - 50 = 0.0056$ mm. This difference is only about 3.4% of the smallest ultrasound wavelength of interest (0.162 mm). Thus, it can be assumed that the size of the line laser source has little destructive effect on the amplitude of the ultrasound received at receiving point. Based on Eq. 4-7, the source-destination distances for 7 individual sources are plotted in Fig. 4-19.

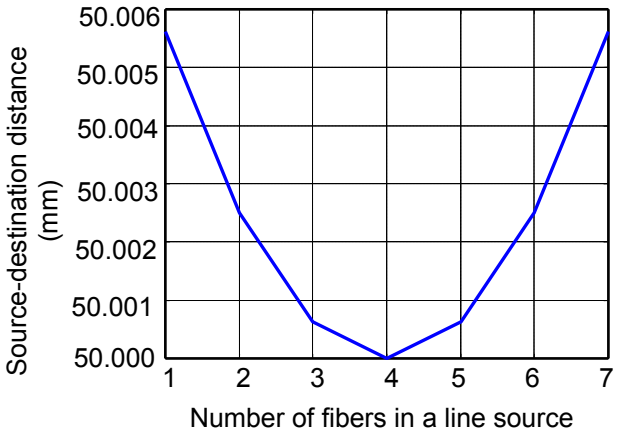

Fig. 4-19: Source-destination distance for 7 individual fibers.

To quantitatively analyze how the line size affects the single source performance, an analytical simulation is conducted with Matlab. It is assumed that the ultrasonic field generated by each fiber has the same amplitude A at source and B after they travel to the receiving point. Same attenuation is assumed as well for simplicity.

$$u_i^S(t) = A\sin(\omega t), \qquad i = 1, 2, \ldots 7$$
$$u_i^R(t) = B\sin\left[\omega\left(t - \frac{s_i}{v}\right)\right] = B\sin\left(\omega t - \omega\frac{s_i}{v}\right) \qquad \text{Eq. 4-8}$$

where,

$u_i^S(t)$: Ultrasonic fields generated at the source;

$u_i^R(t)$: Ultrasonic fields at the receiver location;

v: Speed of ultrasound;

ω : Angular frequency of ultrasound ($\omega = 2\pi f$);

s_i: Propagation path of ultrasound from source i.

The resultant ultrasonic field at the receiver location is the superposition of the seven fields at the receiver location described by Eq. 4-9:

$$u_s^R(t) = \sum_{i=1}^{7} B\sin\left(\omega t - \omega\frac{s_i}{v}\right) \qquad \text{Eq. 4-9}$$

Without the difference on the propagation path, all the $u_i^R(t)$ should be completely in phase and $u_s^R(t)$ should have an amplitude of 7*B. With the phased difference introduced by the propagation path difference, the resultant ultrasonic field has an amplitude that is less than 7*B. A Matlab program has been written to calculate the amplitude of $u_i^R(t)$. Fig. 4-20 shows the simulated result for frequency range of 0.5 ~ 20 MHz. The amplitude becomes smaller as the frequency increases since the wavelength is inversely proportional to the frequency. However, the decrease in amplitude for the entire range is so small (<0.36%) that it can be neglected.

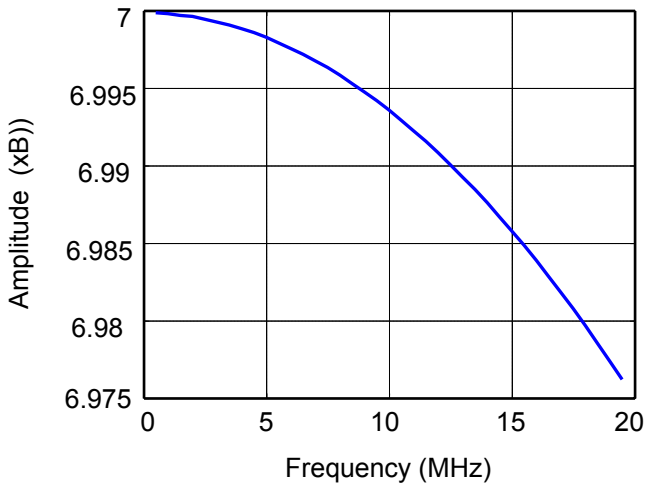

Fig. 4-20: Ultrasonic field amplitude at receiving point for 0~20 MHz.

In conclusion, the size of the line source will have more destructive effect at higher frequency. In this particular application, the decrease of the amplitude is less than 0.1% in the frequency range 0.5 ~ 2 MHz in which the EMAT receiver operates. So the destructive effect of line size can be ignored.

CHAPTER V

PARAMETRIC MODELING OF GMAW FOR TEMPERATURE DISTRIBUTION

The remote, real-time temperature measurement in welding process is not readily available while the temperature distribution is desired for ray-tracing algorithm. Furthermore, such sensors would only be applicable to the surface temperatures. The Finite Element Analysis (FEA) has been proven to be a very economic and efficient approach to obtain the temperature distribution in welding [Prasad and Narayanan, 1996; Kannatey-Asibu, *et al.*, 1989; Goldak, *et al,* 1986].

5.1 FE MODELING OF TEMPERATURE DISTRIBUTION IN WELDING

5.1.1 Fundamental Principles

A. Heat Equation

Based on the principle of conservation of energy, the heat equation is described by Eq. 5-1 [Radaj, 1992].

$$c\rho\frac{\partial T}{\partial t}=\frac{\partial}{\partial x}\left(k\frac{\partial T}{\partial x}\right)+\frac{\partial}{\partial y}\left(k\frac{\partial T}{\partial y}\right)+\frac{\partial}{\partial z}\left(k\frac{\partial T}{\partial z}\right)+\frac{\partial Q_v}{\partial t} \qquad \text{Eq. 5-1}$$

where

c : Specific heat capacity (J/kg°C)

ρ : Density of the material (kg/m^3)

k : Coefficient of thermal conductivity (W/m°C)

Q_v : Heat energy released or consumed per unit of volume (J/m^3)

Due to the complicated metallurgical changes in the work piece during the welding process, it is difficult to formulate an exact mathematical model of welding process. Appropriate simplifications and assumptions are necessary to make the simulation feasible in commercial FEA packages such as Ansys.

B. Initial Conditions:

The initial condition is usually the location-constant temperature of the surrounding medium or of preheating; in exceptional cases also a certain temperature distribution. For this specific case, the initial condition is the location-constant temperature of the surrounding medium of 25°C.

C. Boundary Conditions:

The boundary conditions are used to describe the heat exchange between the plate and its surroundings, the conditions of heat dissipation at the boundary surfaces of the structure. In this case, the natural boundary condition is desired and defined as Eq. 5-2:

$$k\frac{\partial T}{\partial n}+\alpha(T-T_0)+\sigma\varepsilon(T^4-T_0{}^4)=0 \qquad \text{Eq. 5-2}$$

where

k : Coefficient of thermal conductivity (W/m°C)

α : Heat transfer coefficient for convection (W/m^2°C)

σ : Stefan-Boltzmann constant (5.67x10^{-8} W/ m^2°C^4)

ε : Emissivity

T_0 : Ambient temperature (°C)

The three terms in Eq. 5-2 are used to describe thermal conductivity, convection, and radiation respectively. The upper surface area experiences forced convection because of the flow of the shielded gas, while the other sides of the weldment experience natural convection. These two convection boundary conditions are described by different convection heat coefficients: α_f = 50 W/m^2°C for forced convection and α_n = 18 W/m^2°C for natural convection [Boo, Cho, 1990]. The radiation is characterized by the emissivity. For polished metallic surfaces, ε = 0.2~0.4. For rough, oxidized surfaces of steel, ε = 0.6~0.9.

D. Heat Source

The welding heat source can be modeled as a moving point source, a moving line source, or a moving Gaussian distributed area source. The Gaussian distribution is preferred by most researchers because of its accuracy. In this project, an evenly distributed moving volume source is assumed for more accuracy. Based on earlier work [Radaj, 1992], the efficiency for the heat input of GMAW process is 0.65~0.90. A value of η = 0.7 is used in this project. The net rate of thermal energy q supplied by the welding arc is expressed by Eq. 5-3.

$$q = \eta UI \qquad \text{Eq. 5-3}$$

where

η : Heat transfer efficiency

U : Welding voltage (V)

I : Welding current (A)

Then, the heat generation corresponding to the volume in which the heat input is applied can be derived by dividing the heat-input q by the volume.

The volume heat source (heat generation) is used for accuracy. In this case, the welding arc is modeled as a uniform volume heat source. The size of the volume source is taken as the half of the weld. The moving arc is modeled with 100 steps along the welding direction.

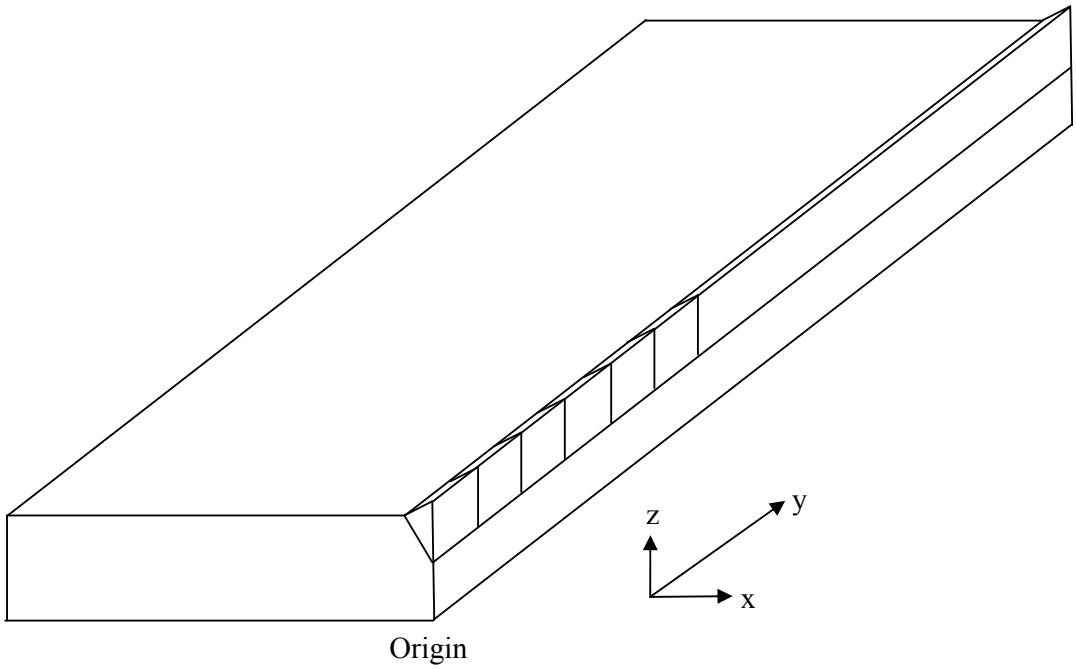

Fig. 5-1: Volume welding heat source with uniform distribution.

E. Material Properties for the Model:

For an accurate simulation result, the temperature dependent material properties are adopted, which are summarized in Table 5-1.

Table 5-1: Properties of mild steel [Radaj, 1992; Goldak, et al., 1986].

Temperature (°C)	0	200	400	600	800	1000	1500
Coefficient of thermal conductivity k (W/m°C)	62	53	45	36	33	---	---
Density ρ (kg/m^3)	7860	7800	7750	7680	7600	7530	---
Enthalpy (J/m^3) x10^9	---	---	---	1.2	---	---	10
Specific heat capacity c (J/kg°C)	600						

5.1.2 ANSYS Modeling

The ANSYS model for the welding temperature distribution is generated using ANSYS Parametric Design Language (APDL). Using APDL, as opposed to the Graphical User Interface (GUI), provided much greater flexibility in regard to altering geometric features, mesh spacing, boundary conditions, and applied loads.

A. Geometric Modeling

In order to take advantage of the symmetry and reduce the computation cost, only one of the two plates is modeled. The plate measures 101.6 x 203.2 x 12.7 mm (4" x 8" x 0.5"). As shown in Fig. 5-2, the entire half plate is modeled as four volumes. In this way, the different meshing sizes can be specified in different volumes. Note that four volumes

must be glued together before meshing is performed. If only one entire volume is defined, the mapped meshing is not allowed by Ansys.

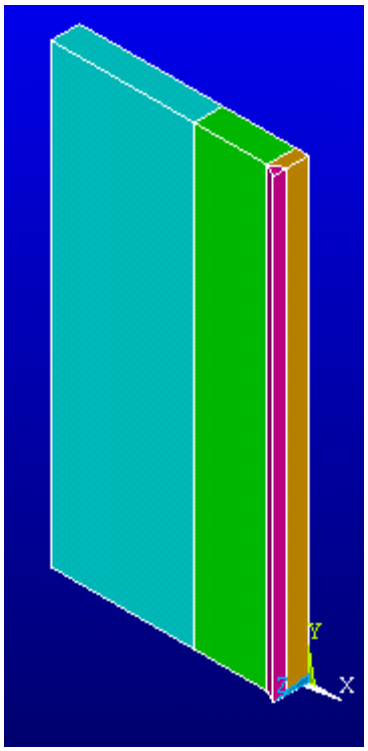

Fig. 5-2: Geometric modeling: the plate is modeled as 4 separated volumes.

B. Meshing:

Solid 70, a 3-D thermal brick element is used to mesh the whole volume. This element has eight nodes with a single degree of freedom, temperature, at each node. The element is applicable to a three-dimensional, steady-state or transient thermal analysis.

The vicinity of the weld path is meshed with finer elements because it has a greater temperature gradient than the rest of the model does. With all the information described above, the FEA simulation of the temperature distribution in welding process is carried out in Ansys 5.7.1. Fig. 5-4 shows the meshed model.

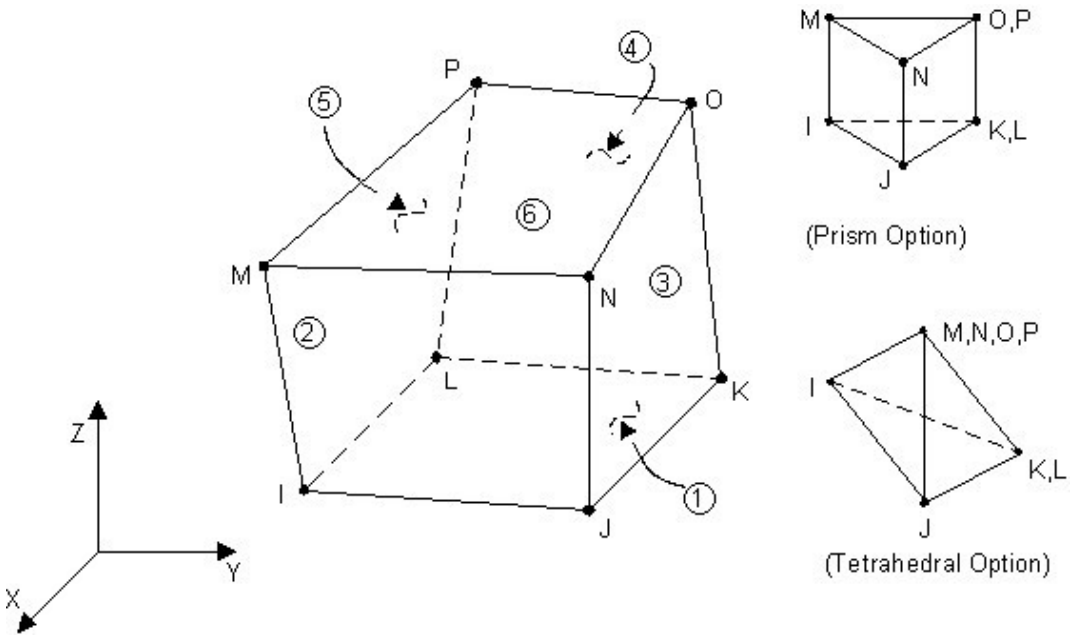

Fig. 5-3: 3-D thermal solid element - Solid70.

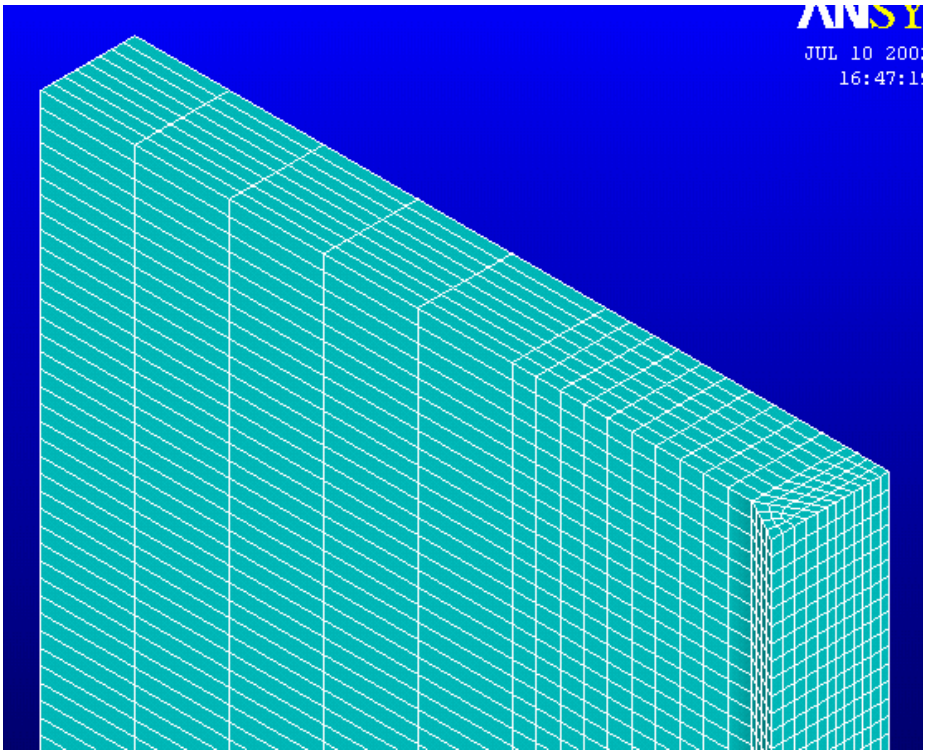

Fig. 5-4: Meshing of the model.

C. FEA Simulation Results

The simulation takes about 2 hours of the machine time for a 2.0 GHz Pentium 4 PC. Fig. 5-5 shows the temperature profiles at three time periods: t = 9 second (when welding torch reaches the middle of the weld), t = 18 second (when welding torch reaches the end of the weld), and t = 100 second (after it cools down for about 80 seconds). The results look like the wake caused by a ship moving in the water, which is expected. Since the welding arc moves relatively fast across the plates than the heat propagates in the direction perpendicular to the welding direction, the wake is very narrow.

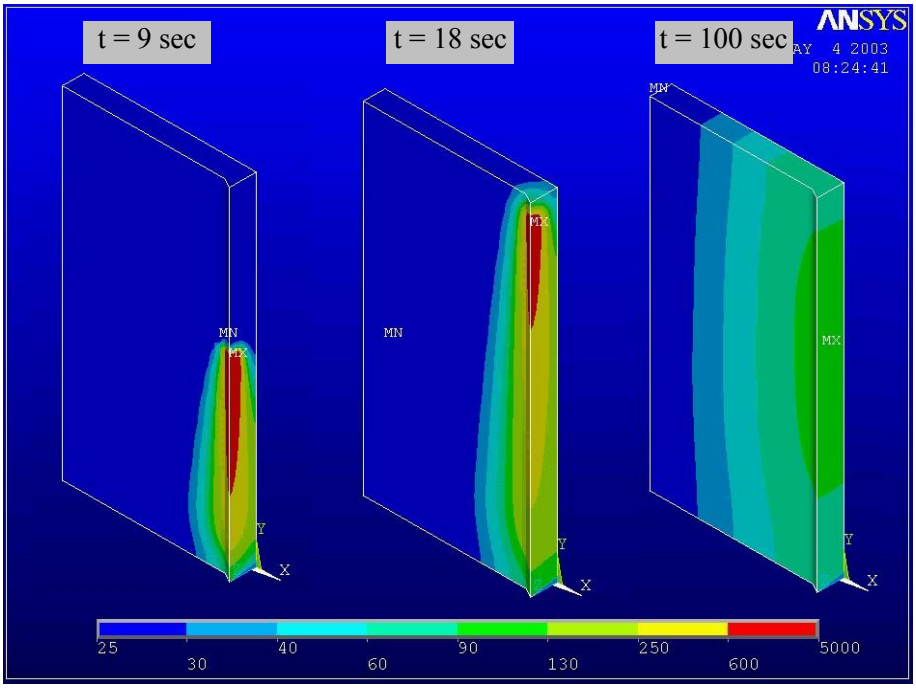

Fig. 5-5: Simulation results at three time periods

To verify the simulation results, the time history expression of the temperature profile at certain locations is desired to be compared to the experimental measurements. Fig. 5-6 shows the temperatures at six locations outlined by Fig. 5-7.

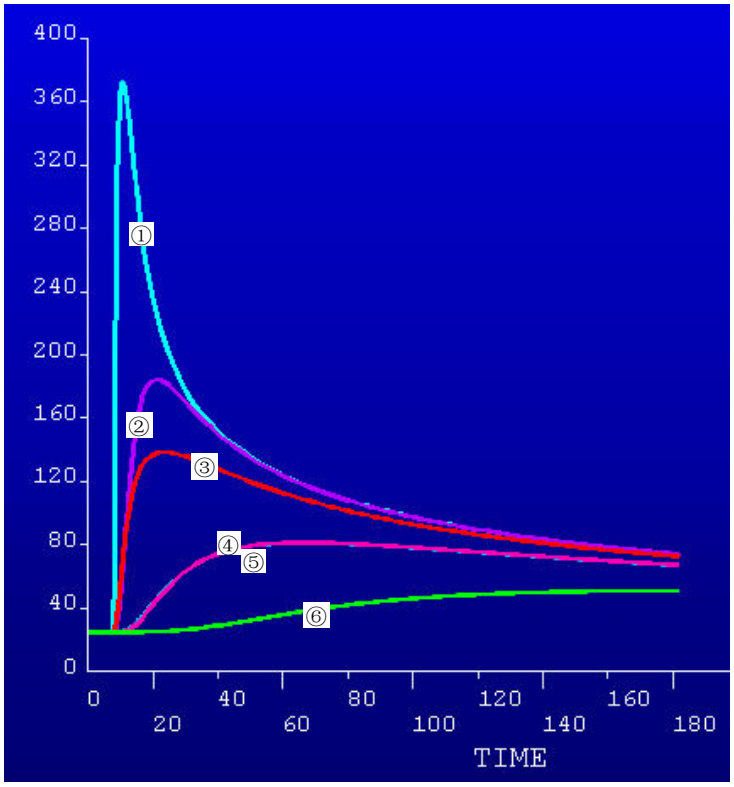

Fig. 5-6: Time history expression of the temperature profile at certain locations.

5.2 Experimental Measurement of Temperature Profile During GMAW

5.2.1 Measuring Setup

To verify the FEA model developed in last section, the temperatures are measured at 6 selected locations on both top and bottom of the weld samples, as shown in Fig. 5-7 and Fig. 5-8. An acquisition card, DaqBoard 112 from Omega Engineering, is used to acquire the temperature measurements from the 6 thermocouples. This card has sixteen input channels that are capable of performing A/D conversions at 100 kHz per channel, and two output channels that are capable of generating ±5V analog output signals. An extension card, DBK19 Thermocouple card, from the same company is used to interface

the thermocouples and the acquisition card. Hi-temperature inconel overbraided ceramic fiber insulated thermocouples are used in this measurement. This type of thermocouples can withstand temperatures up to 1090 ºC with K thermocouple calibration.

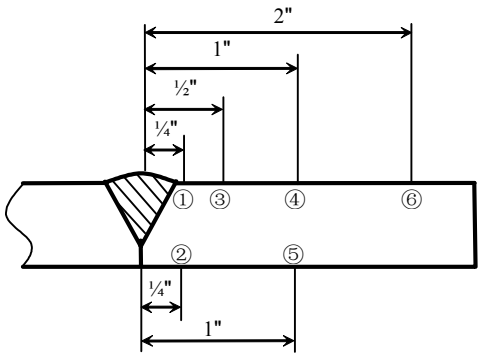

Fig. 5-7: Temperature measuring configuration. Four thermocouples are placed on the top (3.175 mm deep) and two thermocouples are placed on the bottom (3.175 mm deep).

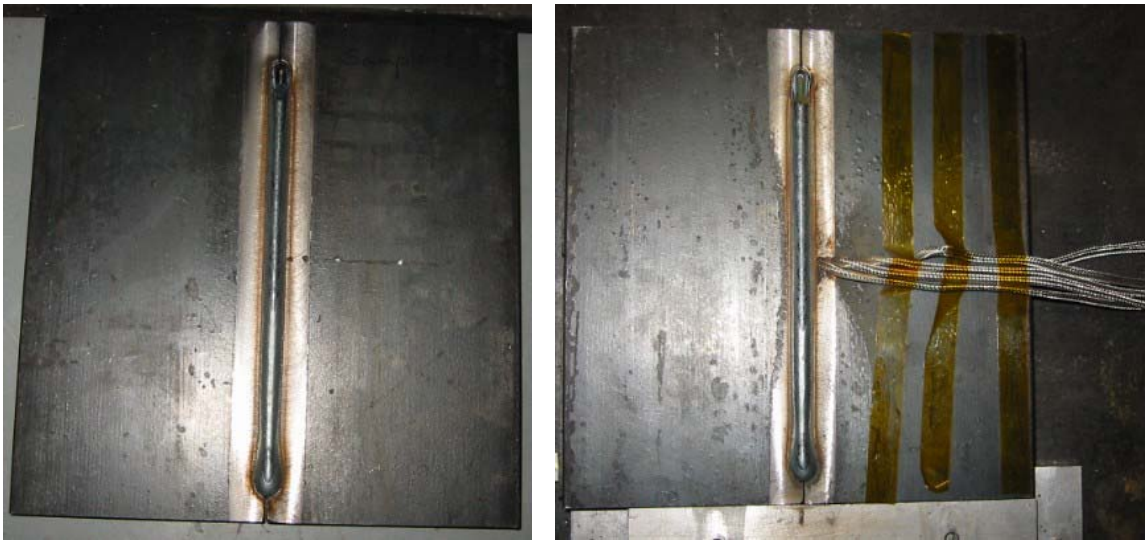

(a) (b)

Fig. 5-8: Welding samples with holes to hold thermocouples. (a) Sample 1 that shows holes in the middle. (b) Sample 2 that shows thermocouples placed in the holes and taped to the sample surface with Teflon tape.

5.2.2 Comparison of Experimental and Simulation Results

The temperature measurements are performed with the GMAW of two 1018 mild steel samples. The temperature profiles in time history at the six selected locations are recorded with the thermocouples. The measurement is repeated four times with the same setup and same welding parameters. The four measurements are then averaged to obtain a relatively reliable temperature profile.

Fig. 5-9 shows one of the temperature measurements and Fig. 5-10 shows the average of the four measurements. The averaging reduces both noise caused by the welding process and the deviation cased by the measuring location perturbation. A signal from robot controller is also recorded that indicates the welding period, as shown in the two figures.

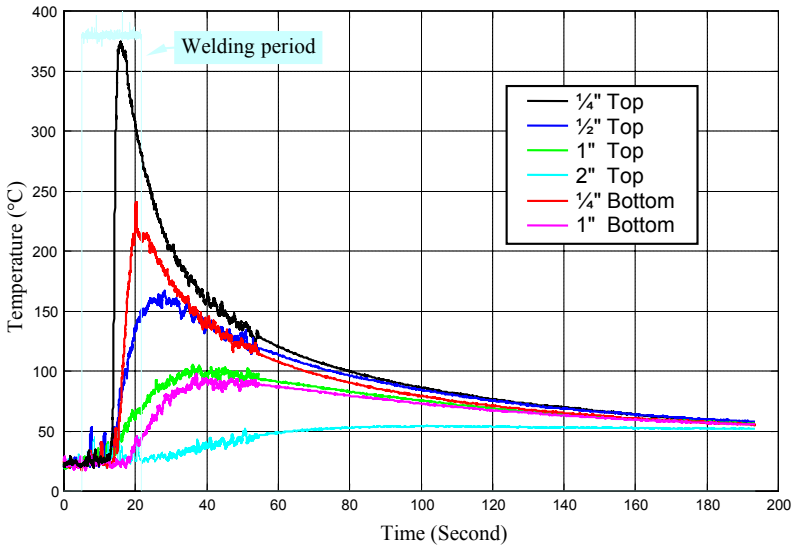

Fig. 5-9: Temperature profile measured with sample 1. (Welding voltage = 25V; Welding current = 250 A; Wirefeed rate = 500 in/min; Welding speed = 0.5 in/sec)

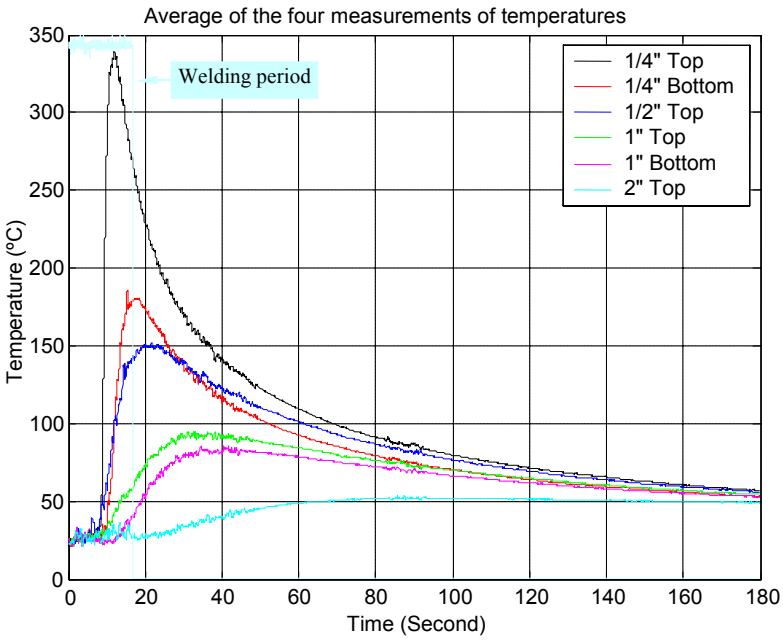

Fig. 5-10: Average of four measurements of temperatures (Welding voltage = 25V; Welding current = 250 A; Wire feed rate = 500 in/min; Welding speed = 0.5 in/sec)

The time history temperature profiles from both FE simulation and experimental measurements are compared in Fig. 5-11. The simulation results agree well with the experimental measurement at the specified locations. The maximum difference between peak values is 33°C(9.7%) at location ①.

This discrepancy between the simulation and experimental results may be caused by either simulation or experiments. In FE simulation, the uniformly distributed volume heat source is a simplification from the real situation. The heat efficiency and boundary conditions are estimated. In the experiments, the thermocouple measuring bead size ranges from 1 mm to 2 mm. So the measurement of the temperature would be an average of the small volume rather than a point. This definitely causes errors when temperature changes sharply.

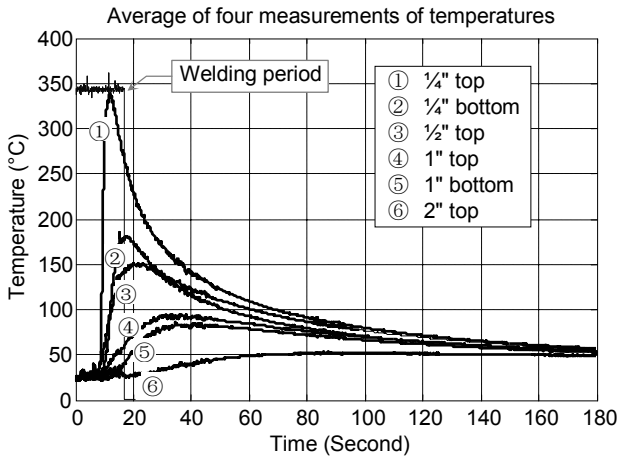

(a)

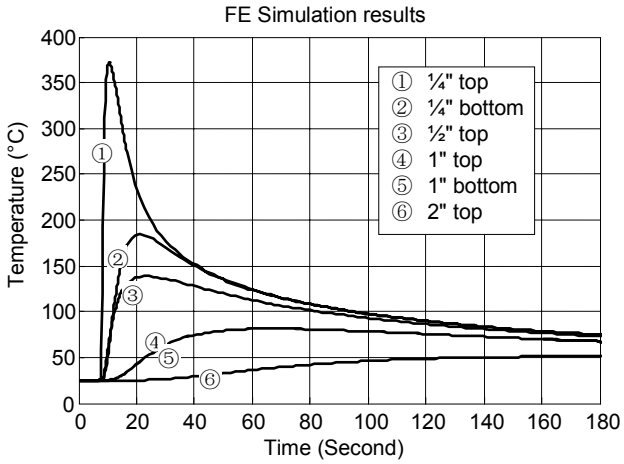

(b)

Fig. 5-11: Comparison of experimental and simulation results of temperature distribution.

(a) Experimental results. (b) Simulation results.

CHAPTER VI

3-D RAY TRACING OF ULTRASOUND DURING REAL-TIME WELDING

Due to temperature gradient around the weld and the temperature dependence of the ultrasound propagation speed, ultrasound ray bending associated with the ultrasound velocity change occurs. The propagation of the ultrasound is no longer a straight line and its real path requires a ray tracing algorithm to find out. Ray tracing problems have been studied in geophysics for seismic modeling [Sadeghi *et al.*, 1998; Grechka *et al.*, 1996]. However, the ray tracing algorithms developed so far in geophysics can not be directly applied to the welding case. A 2-D ray tracing based on Snell's law has been studied and applied on ultrasonic wave propagation in temperature gradients [Johnson *et al.*, 1987]. In this research, a 3-D ray tracing algorithm based on Fermat's principle is presented. First of all, a set of ray equations are derived from Fermat's principle using calculus of variations. Unlike Snell's law, the derivation directly from Fermat's principle does not require the assumption of discrete plane layers and works for both 2-D and 3-D cases. Then, with the temperature field (and then ultrasound speed field) within the weld sample obtained by FEA, Runge-Kutta method is applied to solve the initial value ray equations and the shooting method is applied to solve the boundary value problem to obtain the ray path specified by the source and the destination. After the curved ray path is obtained, the ToF can be found by integrating the time variable along the ray path. Assisted by

geometric analysis, an analytical relationship between the ToF and the penetration depth can be established by repeating the ray tracing algorithm for different penetration depths. Experimental measurements of ToF have been performed to validate the numerical results. Experiments are discussed in Chapter 7.

6.1 Derivation of 3-D Ray Tracing Equations Based on Fermat's Principle

Fermat's principle states that a ray path between any two points P_0 and P_1 is a path of minimum propagation time [Weinstock, 1952]. Shown in Fig. 6-1, the propagation time from P_0 to P_1 is expressed by Eq. 6-1, where *n(x,y,z)* is used to denote the slowness, namely the reciprocal of speed *v(x,y,z)*.

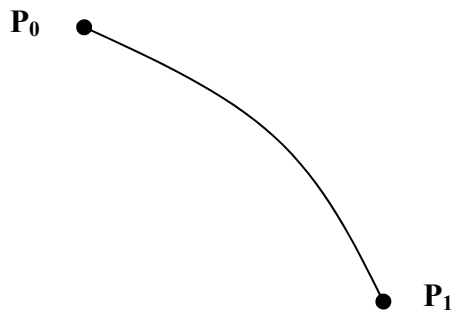

Fig. 6-1: Fermat's principle.

$$T = \int_{P_0}^{P_1} dt = \int_{P_0}^{P_1} \frac{ds}{v(x,y,z)} = \int_{P_0}^{P_1} n(x,y,z)ds \qquad \text{Eq. 6-1}$$

When the ray path is expressed by a parametric form with the independent variable *t* (note that the independent variable *t* could be time, but not necessarily), the differential *ds* of the path is given by Eq. 6-2.

$$ds = \sqrt{\left(\frac{dx}{dt}\right)^2 + \left(\frac{dy}{dt}\right)^2 + \left(\frac{dz}{dt}\right)^2}\,dt = \sqrt{\dot{x}^2 + \dot{y}^2 + \dot{z}^2}\,dt \qquad \text{Eq. 6-2}$$

With the expression of Eq. 6-2, the Eq. 6-1 can be expressed as Eq. 6-3.

$$T = \int_{P_0}^{P_1} n(x,y,z)\sqrt{\dot{x}^2 + \dot{y}^2 + \dot{z}^2}\,dt = \int_{P_0}^{P_1} F(x,y,z,\dot{x},\dot{y},\dot{z})dt \qquad \text{Eq. 6-3}$$

where:

$$F(x,y,z,\dot{x},\dot{y},\dot{z}) = n(x,y,z)\sqrt{\dot{x}^2 + \dot{y}^2 + \dot{z}^2}\,dt \qquad \text{Eq. 6-4}$$

According to the calculus of variations, the minimum of the integral expressed by Eq. 6-3 must satisfy Euler-Lagrange equation [Weinstock, 1952], as shown in Eq. 6-5.

$$\begin{aligned} \frac{\partial F}{\partial x} - \frac{d}{dt}\left(\frac{\partial F}{\partial \dot{x}}\right) &= 0 \\ \frac{\partial F}{\partial y} - \frac{d}{dt}\left(\frac{\partial F}{\partial \dot{y}}\right) &= 0 \\ \frac{\partial F}{\partial z} - \frac{d}{dt}\left(\frac{\partial F}{\partial \dot{z}}\right) &= 0 \end{aligned} \qquad \text{Eq. 6-5}$$

Plugging the expression of $F(x,y,z,\dot{x},\dot{y},\dot{z}) = n(x,y,z)\sqrt{\dot{x}^2 + \dot{y}^2 + \dot{z}^2}$ into Eq. 6-5 gives Eq. 6-6.

$$\begin{aligned} \sqrt{\dot{x}^2 + \dot{y}^2 + \dot{z}^2}\,\frac{\partial n}{\partial x} - \frac{d}{dt}\left(\frac{n\dot{x}}{\sqrt{\dot{x}^2 + \dot{y}^2 + \dot{z}^2}}\right) &= 0 \\ \sqrt{\dot{x}^2 + \dot{y}^2 + \dot{z}^2}\,\frac{\partial n}{\partial y} - \frac{d}{dt}\left(\frac{n\dot{y}}{\sqrt{\dot{x}^2 + \dot{y}^2 + \dot{z}^2}}\right) &= 0 \\ \sqrt{\dot{x}^2 + \dot{y}^2 + \dot{z}^2}\,\frac{\partial n}{\partial z} - \frac{d}{dt}\left(\frac{n\dot{z}}{\sqrt{\dot{x}^2 + \dot{y}^2 + \dot{z}^2}}\right) &= 0 \end{aligned} \qquad \text{Eq. 6-6}$$

Since the ultrasound velocity in weld specimen does not have a closed form expression, Eq. 6-6 can not be solved analytically and a numerical technique has to be sought to solve the ray equations and obtain the ray path. Eq. 6-6 are second order differential equations and it is extremely difficult (if not impossible) to directly solve them numerically. In order to rewrite Eq. 6-6 and express them as six first order equations, the unit tangent vector $\mathbf{I} = (i_x, i_y, i_z)$ is introduced and its three components are shown in Eq. 6-7,

$$\begin{aligned} i_x &= n\dot{x} \\ i_y &= n\dot{y} \\ i_z &= n\dot{z} \end{aligned} \qquad \text{Eq. 6-7}$$

By combining Eq. 6-6 and Eq. 6-7, Eq. 6-8 is derived.

$$\begin{aligned} \frac{di_x}{dt} &= i_x \frac{d}{dt}\left(\ln\left(\sqrt{\dot{x}^2+\dot{y}^2+\dot{z}^2}\right)\right) + \frac{\partial n}{\partial x}\left(\dot{x}^2+\dot{y}^2+\dot{z}^2\right) \\ \frac{di_y}{dt} &= i_y \frac{d}{dt}\left(\ln\left(\sqrt{\dot{x}^2+\dot{y}^2+\dot{z}^2}\right)\right) + \frac{\partial n}{\partial y}\left(\dot{x}^2+\dot{y}^2+\dot{z}^2\right) \\ \frac{di_z}{dt} &= i_z \frac{d}{dt}\left(\ln\left(\sqrt{\dot{x}^2+\dot{y}^2+\dot{z}^2}\right)\right) + \frac{\partial n}{\partial z}\left(\dot{x}^2+\dot{y}^2+\dot{z}^2\right) \end{aligned} \qquad \text{Eq. 6-8}$$

When the independent variable t is considered as time, we have $v = \sqrt{\dot{x}^2+\dot{y}^2+\dot{z}^2}$ and $n = 1/v$. Plugging the expressions of v and n into Eq. 6-8 and combining Eq. 6-7, the ray equations expressed in Eq. 6-9 can be derived.

$$\begin{aligned}
\frac{dx}{dt} &= vi_x \\
\frac{dy}{dt} &= vi_y \\
\frac{dz}{dt} &= vi_z \\
\frac{di_x}{dt} &= i_x \frac{d}{dt}(\ln v) - \frac{\partial v}{\partial x} \\
\frac{di_y}{dt} &= i_y \frac{d}{dt}(\ln v) - \frac{\partial v}{\partial y} \\
\frac{di_z}{dt} &= i_z \frac{d}{dt}(\ln v) - \frac{\partial v}{\partial z}
\end{aligned} \qquad \text{Eq. 6-9}$$

Given the initial values of the source location **X** and propagation direction **I**, and the velocity (slowness) field over the region of interest, the entire ray path can be found by numerically integrate Eq. 6-7 and Eq. 6-9. The numerical method for solving this problem is discussed next in more detail.

6.2 Numerical Solution of Ray Equations

6.2.1 Ultrasound Velocity Field in Weld Specimen

Ultrasound speed is dependent on temperature. With the temperature distribution obtained by FEA, the ultrasound speed can be determined using empirical relationships between the temperature and the ultrasound speed.

Scruby and Moss have measured ultrasonic velocity in mild steel and published their results for longitudinal and shear waves over the temperature range of 17 - 1200°C [Scruby, Moss, 1993]. Some of the material properties such as Poisson's ratio, Shear modulus, and Young's modulus have been derived.

With shear wave speed and Poisson's ratio known, the surface wave velocity can be derived from Eq. 6-10[Graff, 1975].

$$C_R = C_t \frac{0.87 + 1.12\sigma}{1 + \sigma} \qquad \text{Eq. 6-10}$$

where,

σ : Poisson's ratio

C_R : Rayleigh surface wave velocity

C_t : Shear wave velocity

Fig. 6-2 shows the velocities of three major ultrasonic waves at different temperatures.

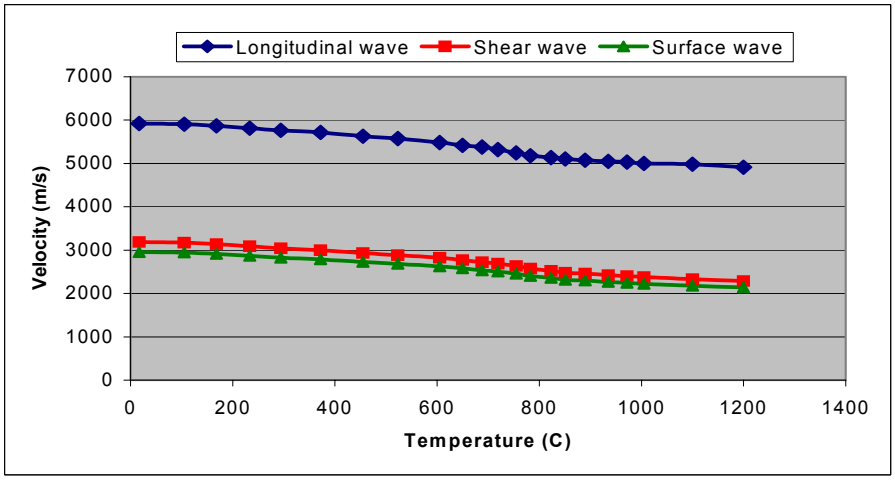

Fig. 6-2: Ultrasonic compression and shear velocity of mild steel as a function of increasing temperature [Scruby, Moss, 1993].

With the simulation results from Chapter VI, the velocity field (slowness filed) within the steel sample can be derived, which will be employed in the ray tracing algorithm to obtained the curved ultrasound propagation path numerically.

6.2.2 Numerical Technique to Solve Boundary Value Ray Tracing Problem

Given the initial values of source location and propagation direction, and the velocity field obtained from 6.2.1, the entire ray path can be found by numerically integrating the ray equations given by Eq. 6-9. In most of the real world applications, however, the ray tracing problem is a two-point boundary value problem, which means the source location and the destination location are give.

For initial value problems, it is possible to start an acceptable solution at its beginning (initial values) and just march it along by numerical integration to its end (final values). For the two-point boundary problems, the boundary conditions at the starting point do not determine a unique solution to start with - and a "random" choice among the solutions that satisfy these (incomplete) starting boundary conditions is almost certain not to satisfy the boundary conditions at the other specified point. The shooting method can be used to solve the two-point boundary value problems. The strategy is iteration on the initial problem approach until the ray path arrives at the specified destination within a preset tolerance.

Since the shooting method is based on iteration on the initial problem approach, the numerical techniques for solving initial value problems serve as the fundamentals for solving boundary value problems. So, before the shooting method is introduced, the two

most commonly used initial value approaches are discussed. They are Euler's method and Runge-Kutta method.

A. Euler's method

Euler's method is a basic numerical approach for solving initial value problems. In Euler's method, linear approximation is used to get the next point. It is a first-order method and hence relatively inaccurate and unstable.

The general formula for Euler's method is briefly introduced [Chapra and Canale, 1998]. Suppose that the goal is to solve the ODE expressed by Eq. 6-11 and to determine $y(t)$.

$$\dot{y} = f(t, y) \qquad y(t_0) = y_0 \qquad \text{Eq. 6-11}$$

First, the independent variable t (usually time in most real world applications) is discretized into small subintervals over the entire interval $[t_0, T]$. The method does not require the subintervals to be equally spaced.

When the slope at t_k is used over the subinterval $[t_k, t_{k+1}]$ and the k^{th} interval size is $h_k = t_{k+1} - t_k$, Eq. 6-12 can be derived to estimate the function $y(t)$. This formula is referred to as Euler's method.

$$y_{k+1} = y_k + f(t_k, y_k)h_k \qquad \text{Eq. 6-12}$$

B. Runge-Kutta method

Euler's method uses straight-line segments to approximate the solution and it is referred as a first-order method. A fundamental source of error in Euler's method is that

the derivative at the beginning of the interval is assumed to apply across the entire interval. Runge-Kutta method is a modification to help circumvent this shortcoming. Runge-Kutta method computes y_{k+1} from y_k in several stages. The most popular Runge-Kutta method is fourth-order and the most commonly used form is shown in Eq. 6-13.

$$
\begin{aligned}
y_{k+1} &= y_k + \frac{1}{6}(k_1 + 2k_2 + 2k_3 + k_4)h_k \\
k_1 &= f(t_k, y_k) \\
k_2 &= f\left(t_k + \frac{1}{2}h_k, y_k + \frac{1}{2}k_1 h_k\right) \\
k_3 &= f\left(t_k + \frac{1}{2}h_k, y_k + \frac{1}{2}k_2 h_k\right) \\
k_4 &= f(t_k + h_k, y_k + k_3 h_k)
\end{aligned}
\qquad \text{Eq. 6-13}
$$

To solve the ray tracing problem with Runge-Kutta method, six first-order ODEs shown in Eq. 6-9 need to be solved simultaneously. In Eq. 6-9, the slopes for i_x, i_y, and i_z involve $\frac{d}{dt}(\ln v)$ and partial differentials $\frac{\partial v}{\partial x}$, $\frac{\partial v}{\partial y}$, and $\frac{\partial v}{\partial z}$. These differentials can be replaced with differences calculated from the velocity field.

C. Shooting method

For the shooting method, the initial direction of the ray traced is assumed to be parallel to the straight line connecting the source and destination. Then the initial problem is numerically solved by integrating along the path until one of the coordinate components (let's take *x*) reaches the destination. The other two coordinate components (*y* and *z*) are compared to the boundary values. If they are within the preset tolerance, the shooting procedure ends and the ray path obtained is considered the actual path for ultrasound to take. Otherwise, the initial propagation direction is updated based on the

error (difference between the actual location and the numerically traced location). The shooting method is very efficient and three or four iterations will bring the traced destination location to the specified boundary value within 1 micro. The algorithm is depicted in Fig. 6-3.

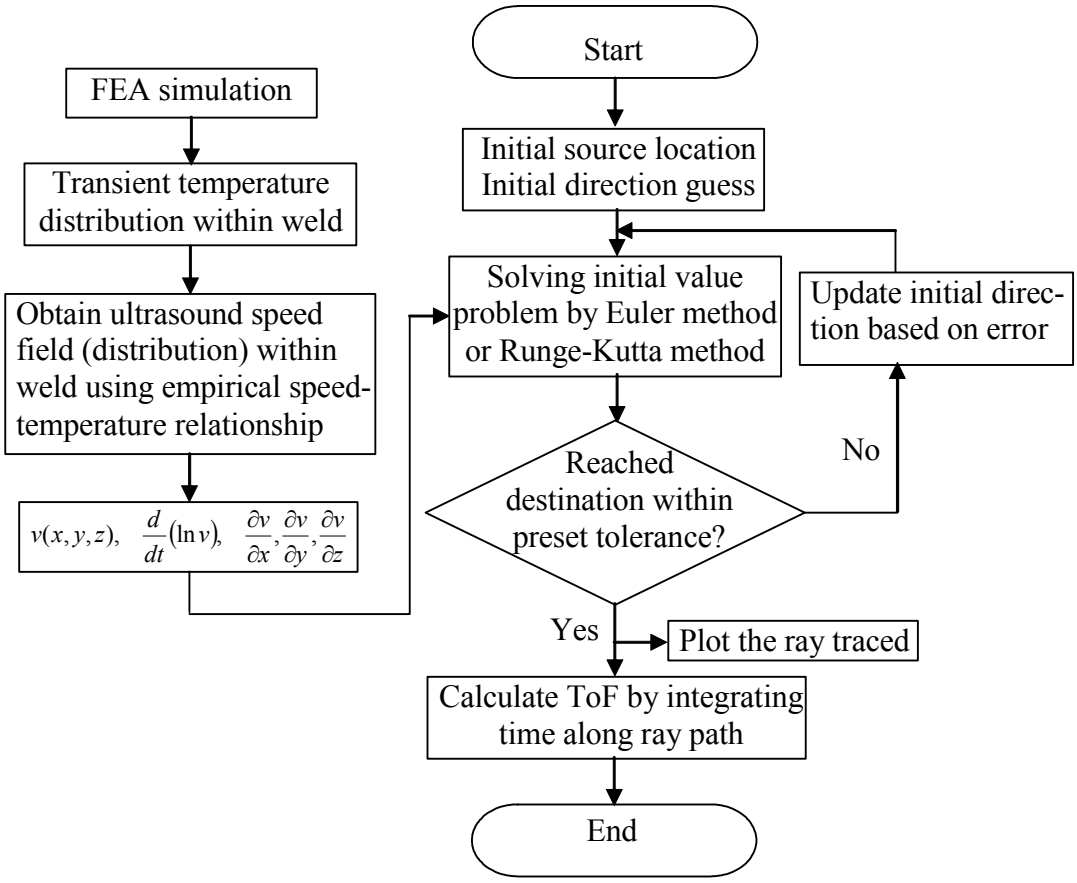

Fig. 6-3: Numerical algorithm to solve boundary value ray tracing problem.

6.3 Numerically Traced Rays for Shear Wave

The ray tracing algorithm is applied on half of the weld sample (illustrated in Fig. 6-4) and the ray path for shear wave is traced. As shown in Fig. 6-5, the propagation of ultrasound in real-time welding obtained by ray tracing is no longer a straight line. The

ray connecting the ultrasound source and the tip of weld is bent downwards at the vicinity of weld tip. This bending agrees with the Fermat's principle because the ray tries to find its way with higher traveling speed (lower temperature) so that it will take the least time to reach the destination.

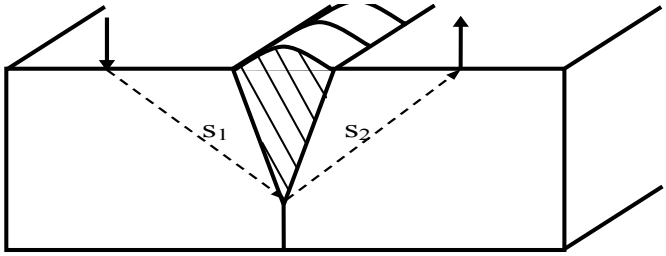

Fig. 6-4: Schematic of weld cross-section. Demonstrated in Fig. 6-5 is left half plate and path s_1 traced for shear wave.

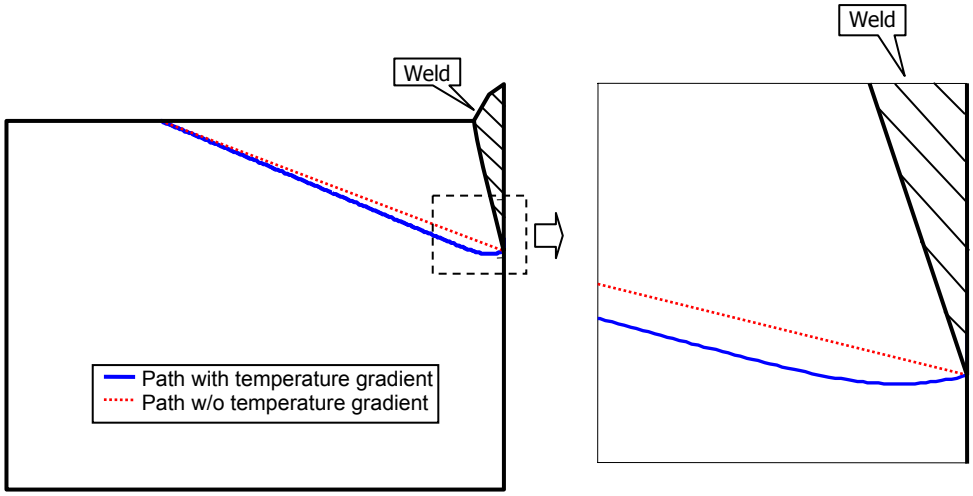

Fig. 6-5: Ray traced for shear wave.

6.4 NUMERICAL TOF

Once ray is obtained numerically, ToF can be determined by integrating time with Eq. 6-14 along ray path (refer Fig. 6-4). Over a series of weld penetration depths, ray tracing is performed and ToF can be determined. Although absolute ToF is obtained in this case, relative ToF (relative to a reference value) is desired because it is more relevant to the applications. Relative ToF (relative to that with penetration depth of 5.5 mm) over penetration depth is plotted in Fig. 6-6, which will be compared to experimental results in next chapter.

$$ToF = \int_{s_1} \frac{ds_1}{v(x)} + \int_{s_2} \frac{ds_2}{v(x)} \qquad \text{Eq. 6-14}$$

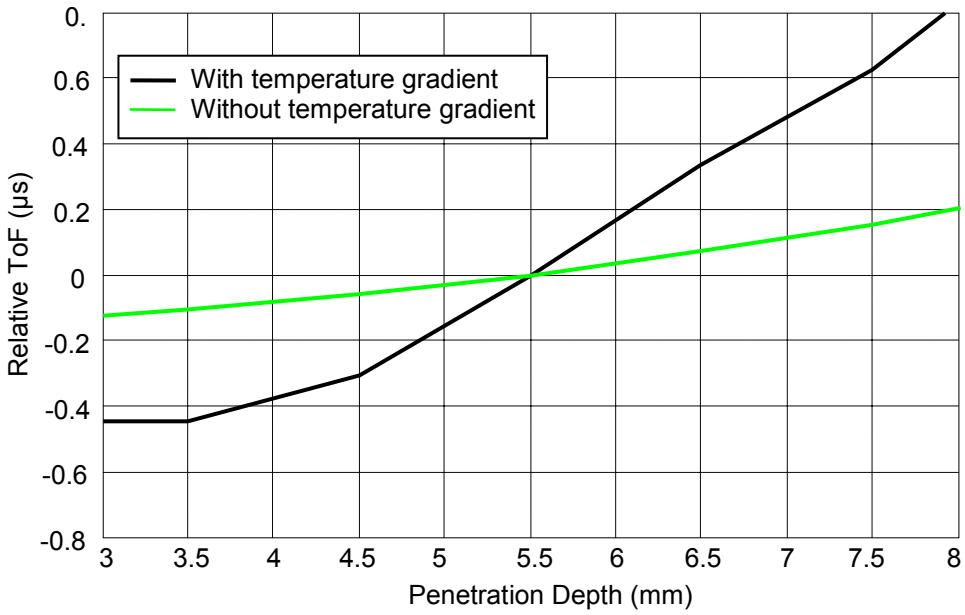

Fig. 6-6: Numerical ToF vs. penetration depth obtained by ray tracing.

CHAPTER VII

EXPERIMENTAL MEASUREMENT OF WELD PENETRATION DEPTH

7.1 MAPPING TOF TO WELD PENETRATION DEPTH

The weld penetration depth can be estimated from the received ultrasound in the following sense. When the welding torch passes, the intensive heat inputs from the welding arc melt the base material and the filling wire and the weld pool forms. Afterwards, the weld pool starts to cool down and solidify. After a certain period of time a solid shell around the liquid pool is formed so that shear wave starts to propagate through the weld bottom, shown by Fig. 4-10. For this reason, the phased array and the EMAT sensing system need to be placed at a lag behind the welding torch. The lag is referred as the torch-sensor distance d_{ts} as shown in Fig. 7-1. In this research project, experiments are conducted with the sensing system stationary. Since the ultrasounds are collected continuously at the rate of the laser firing frequency (10 Hz), the measured ToF can be correlated to the weld penetration depth at various torch-sensor distance d_{ts} (when welding speed is given, its corresponding lag time t_{ts} is given as $t_{ts} = d_{ts} / v$, where v is the welding speed). The optimized d_{ts}, at which the best correlation between measured ToF and weld penetration depth is drawn, will be determined experimentally.

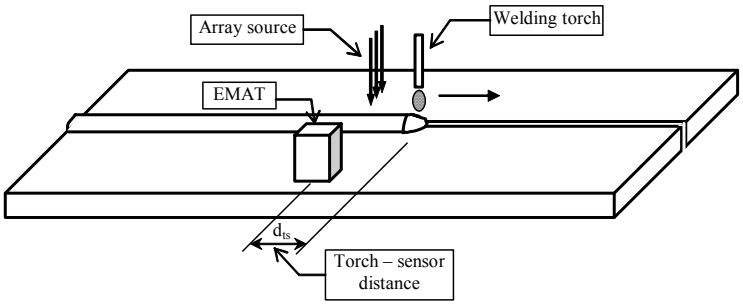

Fig. 7-1: Illustration of torch-sensor distance.

The focus of this research is to establish the relationship between the ToF and the weld penetration depth. Once this relationship is established, the penetration depth can be obtained in real-time from the measured ultrasound ToF.

When a constant ultrasound velocity is considered, the relationship between the ToF and the penetration depth can be obtained by a simple geometric analysis. In reality, however, the traveling speed of ultrasound depends on temperatures. Welding process produces a temperature field with large gradient, especially in the vicinity of the weld pool. To accurately map the measured ToF to the weld penetration depth, temperature dependent propagation speed of the ultrasound and the ray bending of the ultrasound must be taken into account.

First, the case without ray bending is considered. As shown in Fig. 7-2, the ultrasound diffracted at the bottom of the weld bead reaches where the EMAT is placed. The ultrasound speed changes along the traveling path because of the temperature gradient. The relationship between the ToF and the penetration depth D is obtained by the differential analysis on the ultrasonic path, as shown by Eq. 7-1 and Eq. 7-2.

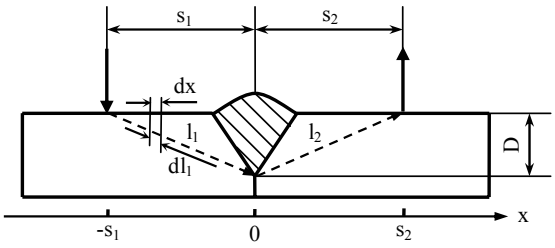

Fig. 7-2: Mapping ToF to the penetration depth.

$$dl_1 = \frac{\sqrt{D^2 + s_1^{\,2}}}{s_1} dx\,, \qquad dl_2 = \frac{\sqrt{D^2 + s_2^{\,2}}}{s_2} dx \qquad \text{Eq. 7-1}$$

$$ToF = \int_{-s_1}^{0} \frac{dl_1}{v(x)} + \int_{0}^{s_2} \frac{dl_2}{v(x)} = \int_{-s_1}^{0} \frac{\sqrt{D^2 + s_1^{\,2}}}{s_1 v(x)} dx + \int_{0}^{s_2} \frac{\sqrt{D^2 + s_2^{\,2}}}{s_2 v(x)} dx \qquad \text{Eq. 7-2}$$

Apparently, the relationship between ToF and weld penetration depth D is non-linear. While the ToF can be evaluated when a penetration depth is given with a closed form equation expressed by Eq. 7-2, no closed form equation can be derived to evaluate the penetration depth D for a given ToF. There are two solutions for this problem. One is to make a table to tabulate the relationship between ToF and D. Whenever a ToF is measured, the computer will look up the table to correlate the ToF to its corresponding penetration D. The second approach is linearization around the desired penetration D. By linearization, the small change of penetration δD is related to the change of $\delta(ToF)$ by a linear factor K, shown by Eq. 7-3.

Assume the weld penetration depth varies by a small amount. The relationship between ToF and penetration depth can be considered linear. The linearization between ToF and penetration depth is obtained by taking the first derivative with respect to

penetration depth D. Shown in Eq. 7-4, K is evaluated at the desired weld penetration depth. Numerical method is used to evaluate the integration.

$$\delta(ToF) = K\delta D \qquad \text{Eq. 7-3}$$

$$K = \frac{\partial(ToF)}{\partial D} = \frac{D}{s_1\sqrt{D^2 + {s_1}^2}} \int_{-s_1}^{0} \frac{dx}{v(x)} + \frac{D}{s_2\sqrt{D^2 + {s_2}^2}} \int_{0}^{s_2} \frac{dx}{v(x)} \qquad \text{Eq. 7-4}$$

When ray bending is considered, Eq. 7-2 and Eq. 7-4 are no longer valid. The ToF is an integration of time along the ultrasound path obtained by ray tracing analysis discussed in Chapter 6.

7.2 ToF Estimation by Cross-Correlation Method

ToF refers to the time for the ultrasound to travel from the source to the receiving point. ToF technique is a relatively recent ultrasonic NDE technique. This method relies on the diffraction of ultrasonic energies from 'ends' of internal structures (such as weld, or crack) in a component under test. The change in ToF caused by the perturbation in penetration depth is expected to be very small. To be able to sense the difference, the ToF has to be estimated very accurately and reliably. ToF can be measured by applying a threshold on the signal, and then locating the time when the signal crosses the threshold [Miller, *et al*., 2002], or by locating the peak directly. When the signal-to-noise ratio is high and the amplitude is consistent, the methods using threshold or locating the peak give reasonably accurate estimate of ToF. However, when the signals are weak or distorted by attenuation and other factors (in welding environment), the above methods become less accurate and less reliable.

In this research, an advanced method based on the cross-correlation technique is developed to measure the ToF. Time delay measurements by cross-correlation method have been used successfully with conventional pulsed ultrasonic contact techniques [Aussel, Monchalin, 1989; Hull, Kautz, Vary, 1985]. Cross-correlation method eliminates the need for the criterion that is usually affected by distortion or low signal-to-noise ratios, and hence gives the most reliable and reproducible results in difficult cases like in welding environment. In this method, a reference signal with the distance between the source and receiving point known is measured ahead of time. The real-time ultrasonic signal is correlated to the reference signal by cross-correlation function. ToF difference between the real-time signal and the reference signal is estimated by locating the peak of the cross-correlation function. The fundamental principle of this technique is presented below.

Assume that the reference signal $x_{ref}(t)$ and the real-time signal $x_{real}(t)$ are simply delayed and magnitude attenuated from the signal at the source $s(t)$ contaminated with random noises $v_1(t)$ and $v_2(t)$, expressed by Eq. 7-5 and Eq. 7-6.

$$x_{ref}(t) = A_{ref}\, s(t - \tau_{ref}) + v_1(t) \qquad \text{Eq. 7-5}$$

$$x_{real}(t) = A_{real}\, s(t - \tau_{real}) + v_2(t) \qquad \text{Eq. 7-6}$$

where:

$s(t)$: Signal at source;

$x_{ref}(t)$: Reference signal received;

$x_{real}(t)$: Real-time signal received;

τ_{ref} : Time delay from the source for reference signal;

τ_{real} : Time delay from the source for real-time signal;

$v_1(t), v_2(t)$: Random noises.

Assume the noises are uncorrelated to each other and they are uncorrelated to the signals, the cross-correlation function between the reference signal and the actual real-time signal can be rewritten as an auto-correlation function of the source signal $s(t)$. This result can be derived from the definition of cross-correlation, as shown by Eq. 7-7

$$\begin{aligned} R(\tau) &= E\{x_{ref}(t)x_{real}(t+\tau)\} \\ &= E\{[A_{ref}s(t-\tau_{ref})+v_1(t)][A_{real}s(t-\tau_{real}+\tau)+v_2(t+\tau)]\} \\ &= E\{[A_{ref}s(t-\tau_{ref})][A_{real}s(t-\tau_{real}+\tau)]\}+E\{[A_{ref}s(t-\tau_{ref})][v_2(t-\tau)]\}+ \\ &\quad E\{[v_1(t)][A_{real}(t-\tau_{real}+\tau)]\}+E\{v_1(t)v_2(t+\tau)\} \\ &= A_{ref}A_{real}R_{ss}(\tau-\tau_{real}+\tau_{ref}) \end{aligned} \qquad \text{Eq. 7-7}$$

where:

$R(\tau)$: Cross-correlation function between $x_{ref}(t)$ and $x_{real}(t)$;

$R_{ss}(\tau)$: Auto-correlation function of $s(t)$;

It is a well established property that the auto-correlation $R_{ss}(\tau-\tau_{real}+\tau_{ref})$ peaks at $\tau-\tau_{real}+\tau_{ref}=0$. Thus, the difference $\tau_{real}-\tau_{ref}$ can be estimated from the $R(\tau)$ by locating the peak.

With finite data record $x_{ref}(t)$ and $x_{real}(t+\tau)$, $0 \le t \le T$, an unbiased estimate of the cross-correlation function is given by Eq. 7-8 [Bendat and Piersol, 1993]:

$$\hat{R}_{unbiased}(\tau)=\frac{1}{T-|\tau|}\int_{0}^{T-\tau}x_{ref}(t)x_{real}(t+\tau)dt \qquad \text{Eq. 7-8}$$

For larger τ, there is less averaging in $\hat{R}(\tau)$ and the estimation becomes less reliable. A windowing function is usually applied to reduce this effect. The most commonly used windowing function is Bartlett window (triangular window). After the Bartlett window is applied, the estimate of the cross-correlation function is called biased, as shown by Eq. 7-9.

$$\hat{R}_{biased}(\tau)=\frac{1}{T}\int_{0}^{T-\tau}x_{ref}(t)x_{real}(t+\tau)dt \qquad \text{Eq. 7-9}$$

7.3 NOISE CHARACTERIZATION

When the auto-correlation of a noise is an impulse and its auto-spectrum is uniform, it is called white noise. In reality, however, almost all of the noises measured by equipment are band-limited because of the presence of the band-pass filter. A band limited white noise has an uniform auto-spectrum over a bandwidth B, expressed by Eq. 7-10.

$$G_{xx}(f)=\begin{cases}G & 0\le f\le B\\ 0 & f>B\end{cases} \qquad \text{Eq. 7-10}$$

The autocorrelation function of the band limited white noise can be derived by taking an inverse Laplace Transformation of Eq. 7-10, as given by Eq. 7-11:

$$R_{xx}(\tau) = \int_0^B G\cos(2\pi f\tau)df = GB\left(\frac{\sin(2\pi B\tau)}{2\pi B\tau}\right) \qquad \text{Eq. 7-11}$$

This correlation function is a *sinc* function and it diminishes very rapidly, with the first zero crossing at $\tau = 1/(2B)$, as illustrated in Fig. 7-3.

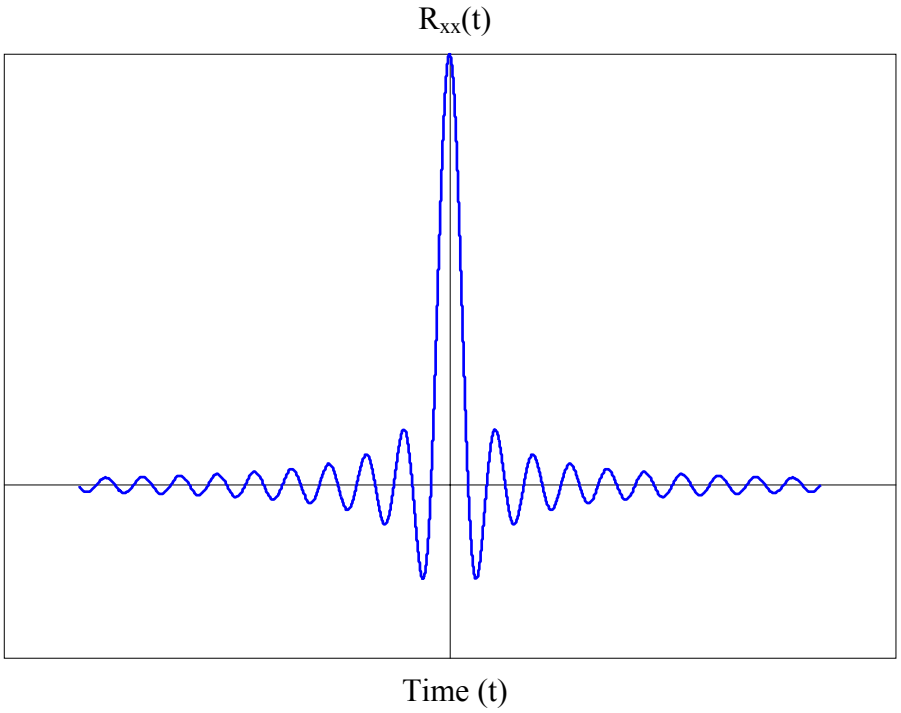

Fig. 7-3: Idealized auto-correlation function for band limited white noise.

It is noted that the validity of Eq. 7-7 is based on the assumption that the noises are uncorrelated to each other. To validate this assumption, the noises are measured by recording the EMAT output without firing laser. One measurement of the noise and the averaging of 32 noise measurements are compared in Fig. 7-4. It is shown that the noise can be reduced significantly to nearly zero by averaging and hence it is random noise. The stochastic characterization of the noise is shown in Fig. 7-5. Since their cross-correlation function is close to zero, the noises are uncorrelated. Its auto-correlation

function looks exactly like the one from a band limited random noise (Fig. 7-3). The first zero crossing occurs at around $\tau = 0.25\mu s$ (as shown in Fig. 7-6), which corresponds to a frequency band of $B = 1/2\tau = 2Mhz$ (band limit for the EMAT reception system).

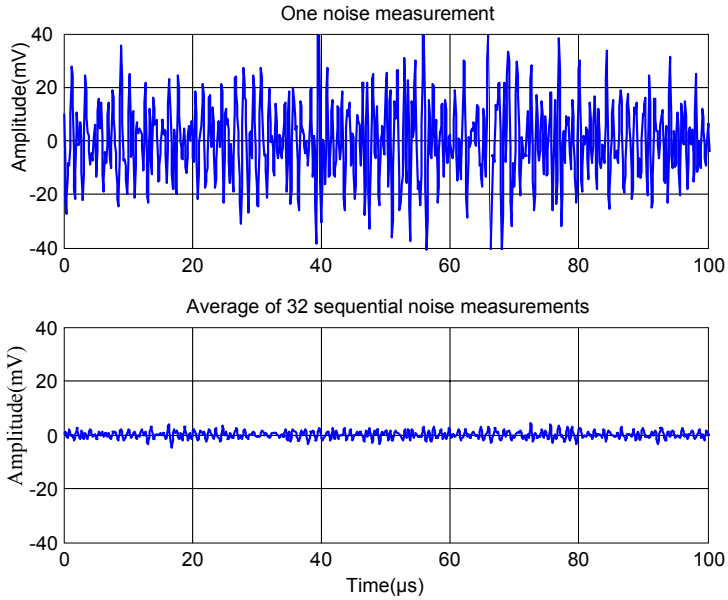

Fig. 7-4: Measured noise.

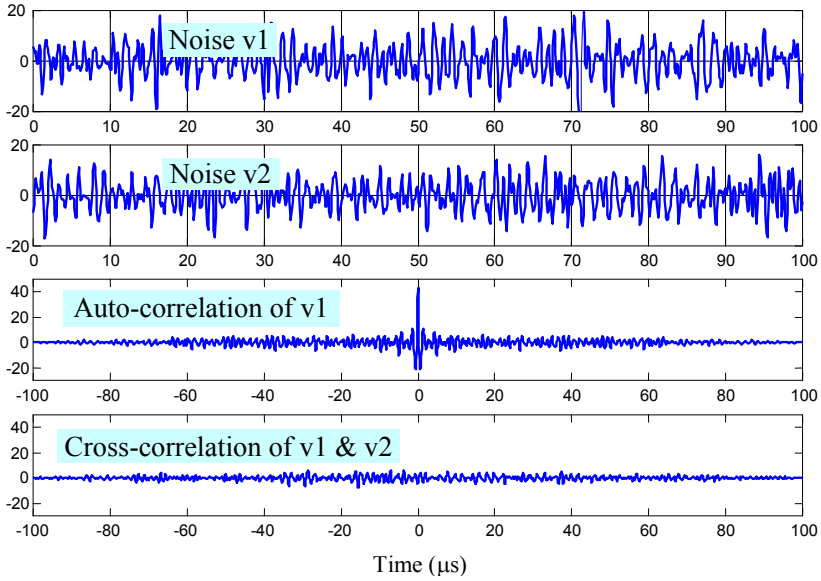

Fig. 7-5: Noise characterization.

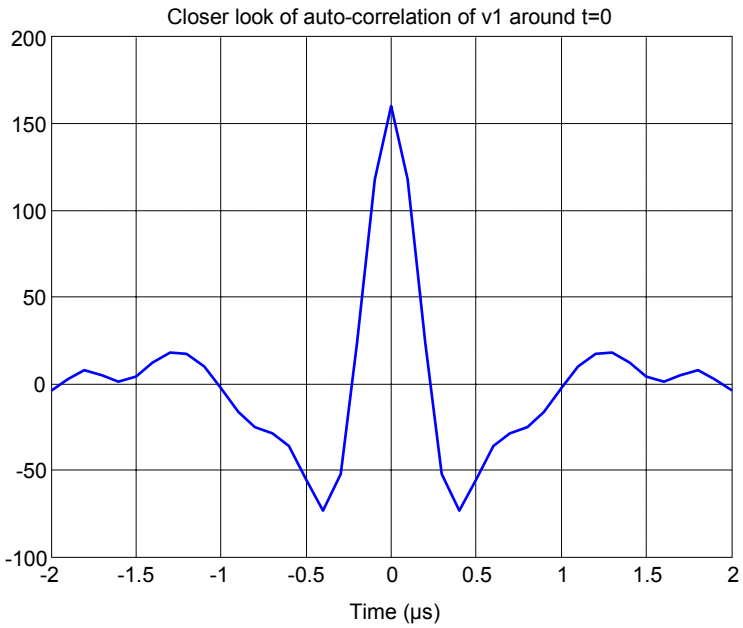

Fig. 7-6: Zoom in of auto-correlation function of measured noise.

7.4 Welding Experimental Setup Conditions and Specimen Preparation

7.4.1 Effects of Welding Parameters on Weld Penetration Depth

The weld penetration depth is affected by most of the welding parameters such as electrode extension, welding torch angle, welding voltage, and welding current, etc. Table 7-2 summarizes the effects on the weld geometries by different welding parameters.

The relationship discussed in this section can be used in the future to correct the welding process based on the real-time measurement of the weld penetration depth. In a controlled experiment, a range of the weld penetration depths could be realized by applying different welding parameters. However, the change on the welding parameters is limited by the welding machine and hence a desired range of the penetration depth can

not be easily realized by changing welding parameters. The specimen preparation is used to achieve a desired range of penetration depth, which is discussed in the next section.

Table 7-1: The effects of GMAW parameters on weld geometries [Smith, 1984].

Welding variables to change	Desired changes							
	Penetration depth		Deposition rate		Bead size		Bead width	
	⇧	⇩	⇧	⇩	⇧	⇩	⇧	⇩
Current and wire feed speed	↑	↓	↑	↓	↑	↓	-	-
Voltage	+	+	-	-	-	-	↓	↑
Travel speed	+	+	-	-	↓	↑	↑	↓
Extension (Stickout)	↓	↑	↑	↓	↑	↓	↑	↓
Wire diameter	↓	↑	↓	↑	-	-	-	-
Gun angle	Back hand	Fore hand	-	-	-	-	Fore hand	Back hand
Legend: - No effect; + Little effect; ↑ Increase; ↓ Decrease								

7.4.2 Welding Scheme

A Miller Pulse Welding machine and a General Electric P-50 robot are used to perform GMAW. The welding parameters include current of 250 A, voltage of 25 V, and wire feed rates of 500 in/min using 0.1143 cm diameter wire. The spray transfer mode is used with a wire-to-workpiece distance of about 0.5 inch. The welds are produced using direct current reverse polarity (DCRP). The shielding gas is 75% argon and 25% carbon dioxide.

A. Polarity

Different welding currents have a large effect on the results obtained in gas metal-arc welding. Optimum efficiency is achieved with DCRP. The heat in this instance is concentrated at the weld puddle and therefore provides deeper penetration at the weld. Furthermore, with DCRP there is greater surface cleaning action which is important in welding metals having heavy surface oxides such as aluminum and magnesium. Direct current straight polarity (DCSP) is impractical with gas metal-arc welding because weld penetration is wide and shallow, and spatter is excessive, and there is no surface cleaning action. The ineffectiveness of straight polarity largely results from the pattern of the metal transfer from the electrode to the weld puddle. Whereas in reverse polarity the transfer is in the form of a fine spray, with straight polarity the transfer is largely of the globular type.

B. Spray transfer:

In spray transfer very fine droplets or particles of the electrode wire are rapidly projected through the arc plasma from the end of the electrode to the work piece in the electrode pointing direction. The droplets are equal to or smaller than the diameter of the electrode. While in the process of transferring through the welding arc, the metal particles do not interrupt the flow of current and there is nearly constant spray of metal.

Spray transfer requires a high current density. With the higher current, the arc becomes a steady quiet column having a well-defined narrow incandescent cone-shape core within which metal transferring takes place. The use of argon or a mixture of argon and carbon dioxide is also necessary for spray transfer. Argon produces a pinching effect on the molten tip of the electrode, permitting only small droplets to form and transfer during the welding process.

7.4.3 Specimen Preparation

As shown in Fig. 7-7, the specimens are grooved in different sizes so that a desired range of weld penetration depth can be achieved without changing other welding parameters.

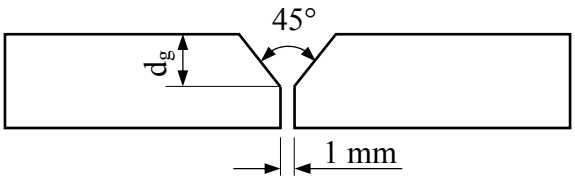

Fig. 7-7: Specimen preparation.

Seven pairs of samples are prepared with the groove depth d_g ranging from 0 to 6 mm. Three sets of samples with grooves are prepared for 1 MHz PZT, 2.25 MHz PZT, and EMAT measurements.

7.5 Experimental Results and Analysis

Experiments are conducted with fiber phased array as ultrasound generation and both PZT transducers and EMAT as receivers. The acquisition of the ultrasonic signals starts when the welding arc is initiated and terminates at 15 seconds after the welding process ends. Before the non-contact transducer EMAT is used as receiver, two PZTs with a high temperature angle beam (70^o) wedge are used to investigate the possibility to monitor the weld penetration depth in real-time with ToF technique.

7.5.1 PZT Reception of Ultrasound

Two PZTs with center frequencies of 1.0 MHz and 2.25 MHz are used as the ultrasound receivers. A 70^{o} angle wedge with high temperature capabilities is used to receive the diffractive shear waves. The 70^{o} angle is chosen because that is about the angle the ultrasound reaches the sample surface from the weld tip. A fixture is designed and machined to hold the angle beam transducer in place and apply constant pressure upon it (that means consistent coupling efficiency) so that the location of PZT transducer is consistent between experiments and the signal strength is not influenced by the coupling. The fixture also serves as a shield and protection for the PZT transducer from the welding arc and spatter. The pictures in Fig. 7-8 show how the angle beam PZT transducer and its fixture work together. The fixture is machined with aluminum for light weight. All the surfaces with contact to the transducer are covered with rubber pads to protect the transducer. The rubber pads also slow down the heat transferred from the aluminum to the transducer. The top cover is connected to the main frame with two hinges and a spring is used to exert constant pressure on the transducer when the top cover is closed.

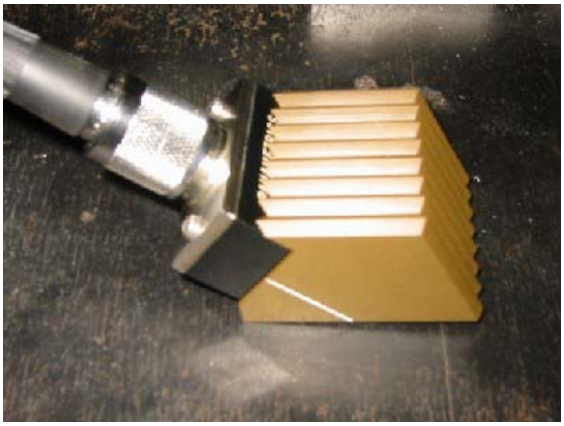

a). PZT transducer with wedge

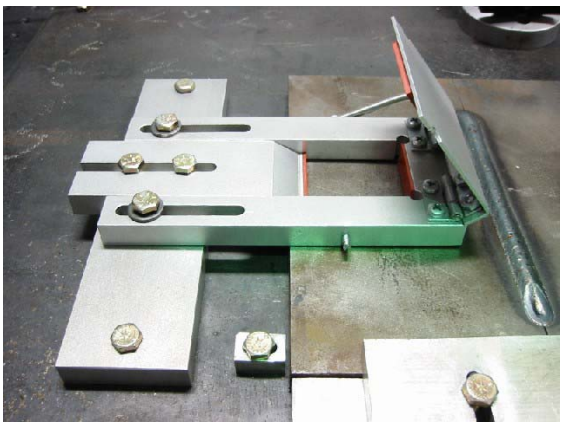

b) Fixture designed for PZT

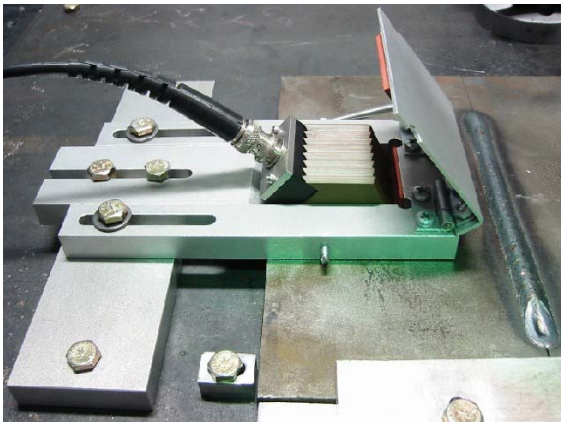

c) Fixture with angle beam PZT

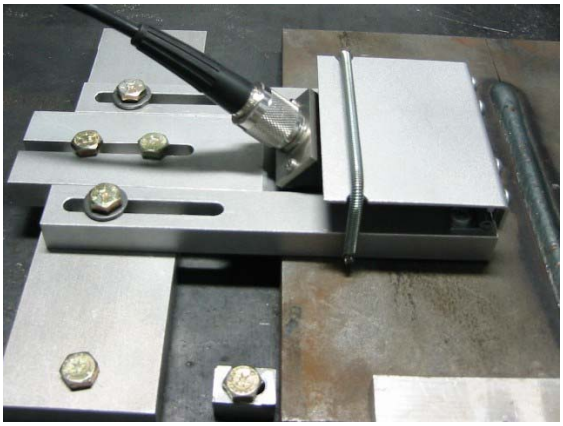

d) Fixture with spring loaded top cover closed

Fig. 7-8: Angle beam PZT and its fixture.

The experimental setup is shown in Fig. 7-9. The fiber phased array generation is on the right half plate. The picture in Fig. 7-9 shows the fiber array chuck and the custom designed focusing objective. The angle beam PZT and its fixture is placed on the left half plate. The welding torch travels between them to make the weld. Fig. 7-10 shows the schematic of the sensing system configuration with measured dimensions.

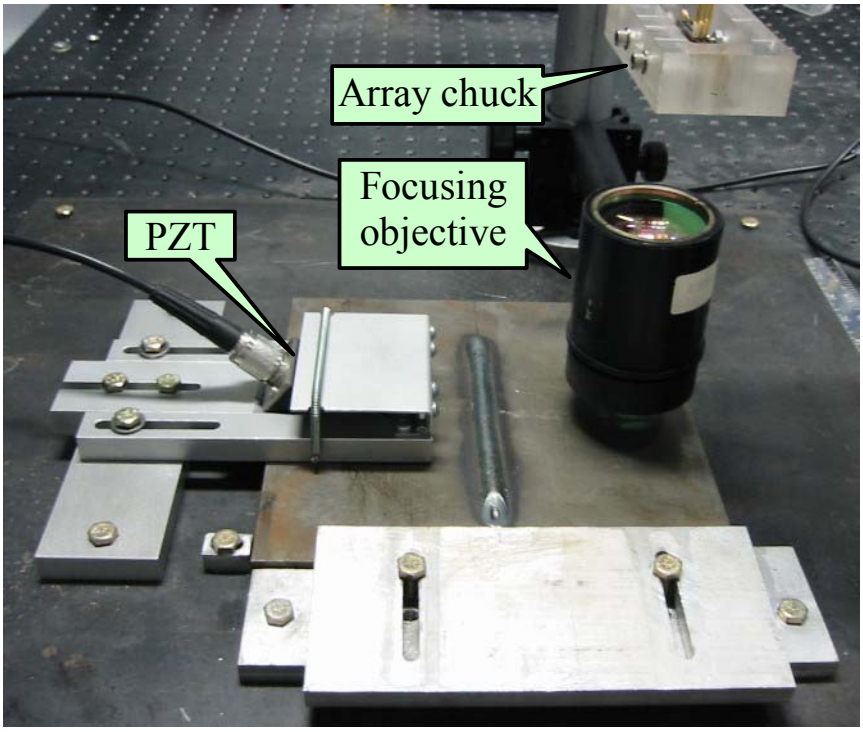

Fig. 7-9: Experimental setup for PZT measurement.

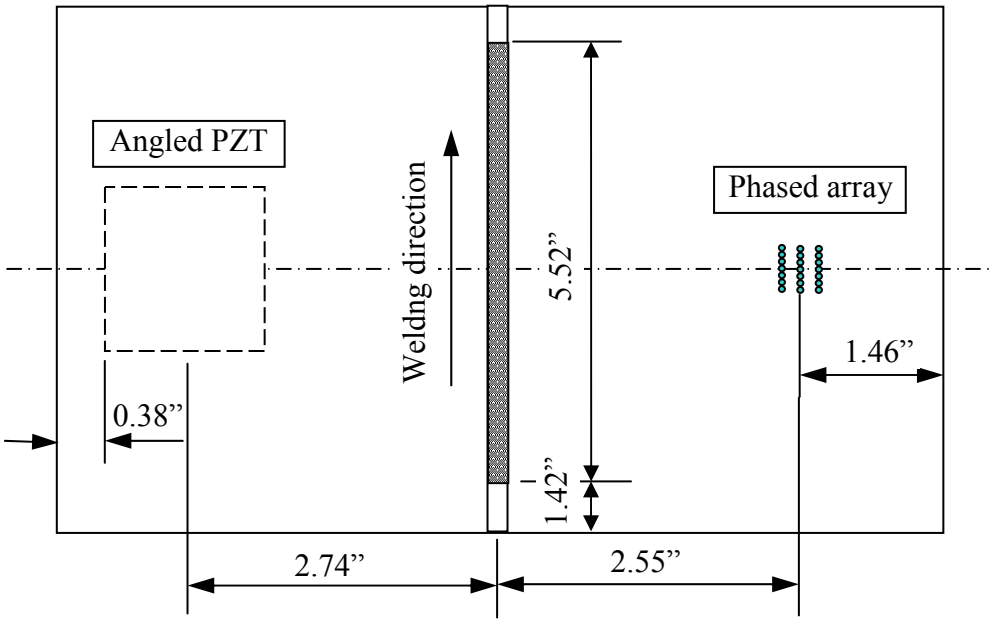

Fig. 7-10: Schematic of the sensor configuration.

The welding experiments are repeated for each transducer with a set of samples with different groove sizes. The typical signal received by the 1.0 MHz PZT is shown in Fig. 7-11. No longitudinal wave is received due to the configuration. The first received shear wave is marked on the plot and it is followed by surface wave and shear waves with multiple reflections.

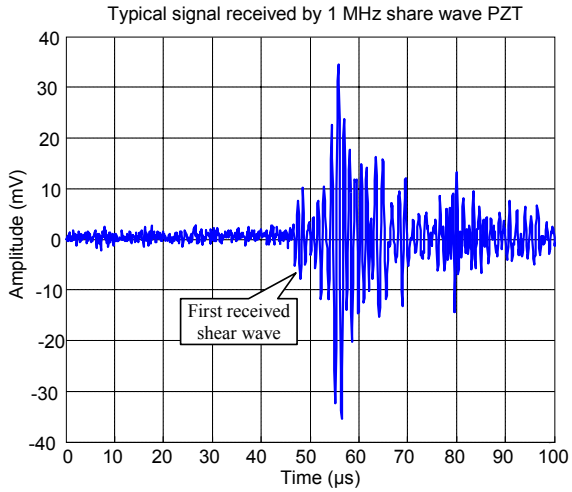

Fig. 7-11: Typical signal received by 1 MHz PZT.

After the welding, all welds are cut perpendicular to weld path to measure the penetration depth. Table 7-2 and Table 7-3 list the prepared groove sizes, measured weld penetration depths, and the weld cross-section images for all the samples. The ruler in the image has the unit of inch.

The weld penetration depth is measured from the bottom side. Both a caliper and a T-shape ruler are used to measure the depth of the unwelded slot and the results are averaged. The weld penetration depth is the difference between the thickness of the sample and the depth of the unwelded slot.

Table 7-2: Weld samples for 1.0 MHz PZT measurement.

Sample number	Groove size (mm)	Measured penetration depth (mm)	Weld cross-section image
1	0	3.175	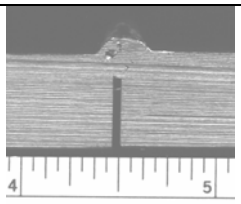
2	1.0	3.518	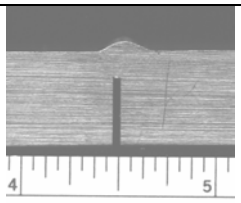
3	2.0	4.489	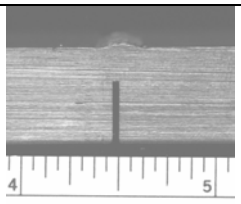
4	3.0	6.433	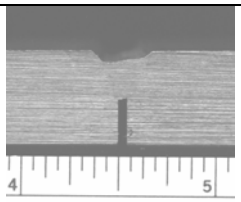
5	4.0	6.318	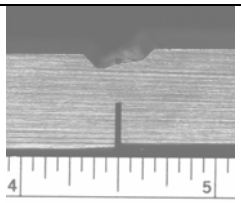
6	5.0	7.658	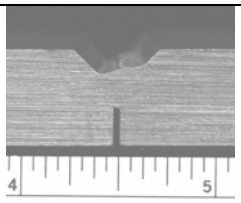
7	6.0	8.172	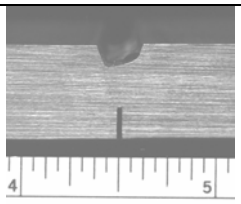

Table 7-3: Weld samples for 2.25 MHz PZT measurement.

Sample number	Groove size (mm)	Measured penetration depth (mm)	Weld cross-section image
1	0	3.334	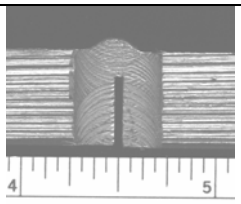
2	1.0	3.829	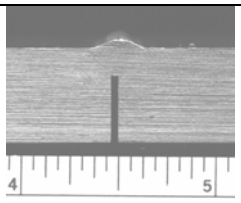
3	2.0	4.826	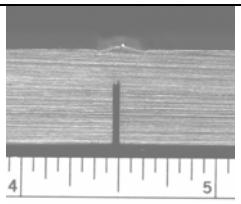
4	3.0	5.264	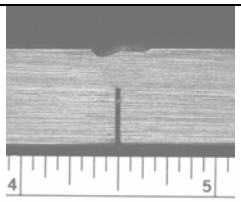
5	4.0	7.068	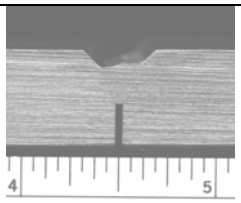
6	5.0	8.007	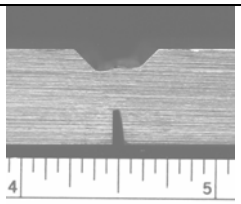
7	6.0	7.684	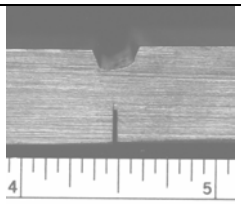

Section 6.4 discussed how the numerical ToF can be obtained after the ultrasound ray is traced. Section 7.2 discussed the experimental estimation of ToF by cross-correlation method, which gives the relative ToF. Relative ToF is preferable over absolute ToF in the real-application because of the following reasons. First, it is difficult to get an accurate absolute ToF estimate. There are two methods that can be used to measure the absolute ToF: threshold method or locating peak method. When threshold method is used, the ultrasound amplitude and noise will affect the measurement of ToF. When the method of locating peak value is used, multiple-peak ultrasound will make it confusing, especially when noise is present. Second, the absolute path corresponding to the absolute ToF is difficult to locate because the receiver is an area receiver.

Both 1 MHz PZT and 2.25 MHz PZT are used to measure the ultrasound signals. All experimental and numerical results of ToF are relative to the sample with penetration depth of 5.5 mm, which is about the middle point of the investigated penetration depth range. The experimental and numerical ToF results for a series of penetration depth are plotted in Fig. 7-12 to Fig. 7-16. Each figure corresponds to a certain time (t_{ts}) that is measured from the moment the welding torch passes the ultrasound sensing system. Different t_{ts} corresponds to the different torch – sensor distance d_{ts}, which is discussed in the beginning of this chapter.

The sum of square error (SSE) is used to measure the deviation of experimental ToF from the numerical values. The smaller value of SSE means better agreement. The numerical results with ray tracing have smaller SSE than those without ray tracing overall. When comparing all of these figures, the experimental ToF gives the best match to the numerical result at $t_{ts} = 2.0$ seconds, which corresponds to the torch –sensor lag of 1 inch.

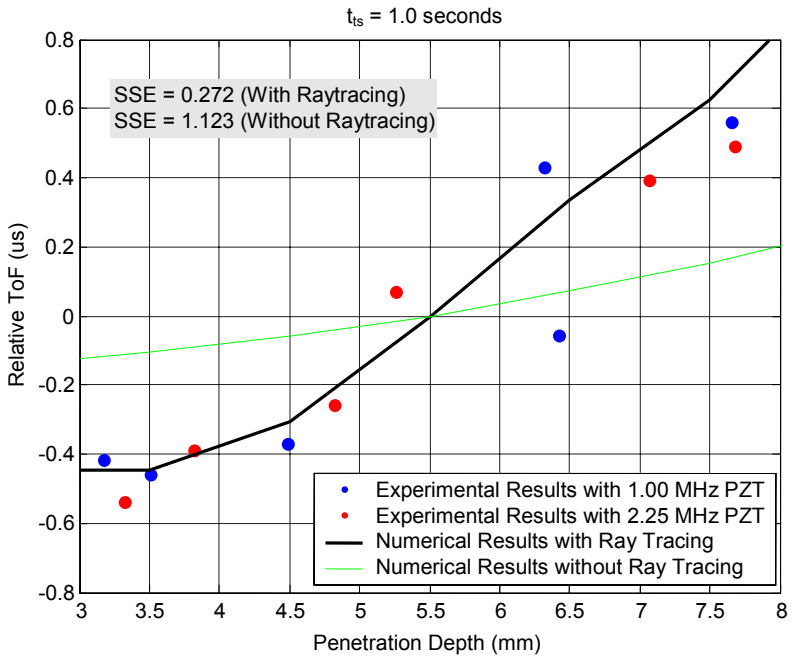

Fig. 7-12: Comparison of experimental and numerical ToF results (PZT, t_{ts} = 1.0 s).

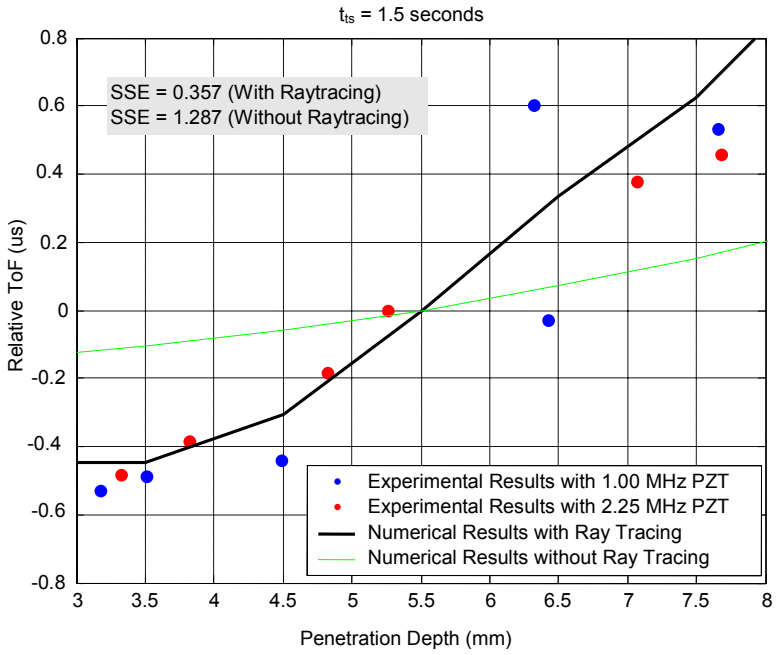

Fig. 7-13: Comparison of experimental and numerical ToF results (PZT, t_{ts} = 1.5 s).

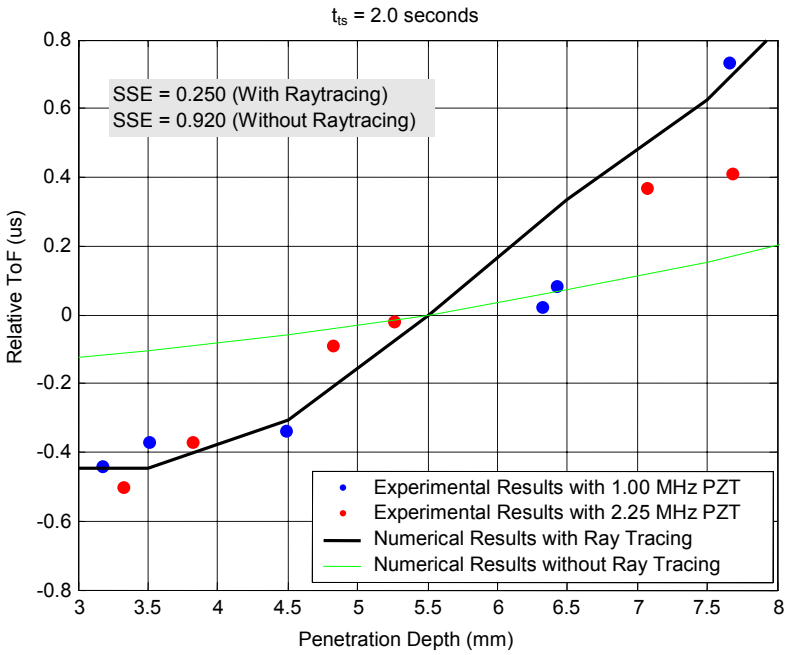

Fig. 7-14: Comparison of experimental and numerical ToF results (PZT, t_{ts} = 2.0 s).

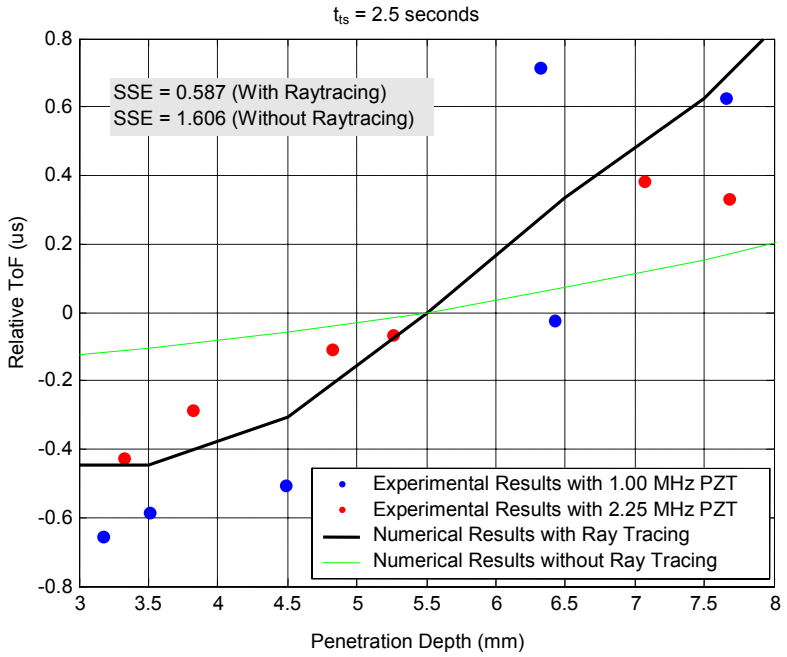

Fig. 7-15: Comparison of experimental and numerical ToF results (PZT, t_{ts} = 2.5 s).

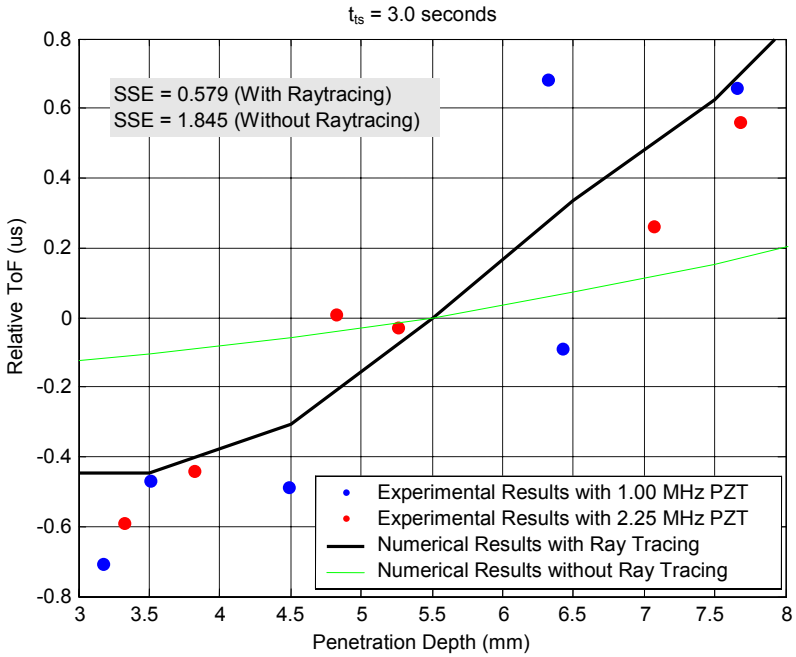

Fig. 7-16: Comparison of experimental and numerical ToF results (PZT, t_{ts} = 3.0 s).

In the first portion of the welding process, no ultrasonic signals can be received because of the air gap between the two samples. Signals start to appear when the welding torch shortly passes the sensor, at about t_{ts} = 1.0 second. The signals are weak and noisy in the beginning so the experimental ToF does not give the best correlation to the weld penetration depth. Based on SSE, the best match between the experimental ToF and the numerical results is obtained at t_{ts} = 2.0 seconds. After that, more weld pool is solidified and the propagation of the ultrasound becomes more complicated. The match of the measured ToF to the numerical results starts to deteriorate.

7.5.2 EMAT Reception of Ultrasound

The EMAT is used to receive the ultrasound in a similar setup, as shown in Fig. 7-17. EMAT is preferred in a final sensing system setup because it is noncontact and capable of operating at high temperatures for an extended time period.

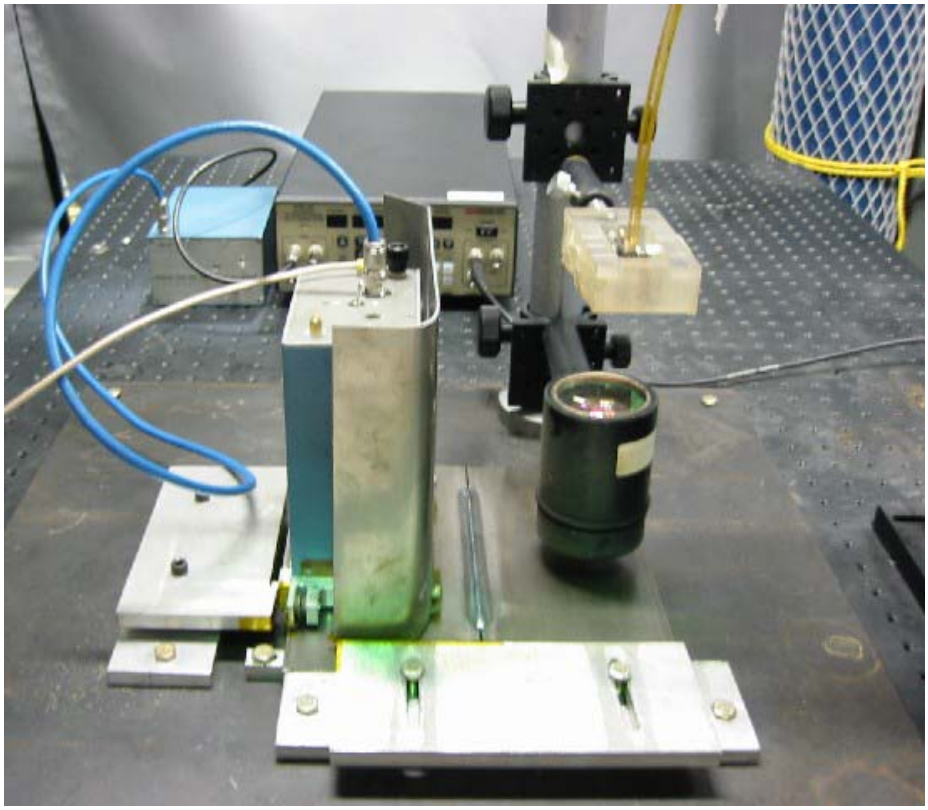

Fig. 7-17: Experimental setup for EMAT measurement.

Again, all welds are cut perpendicular to weld path to measure the penetration depth. Table 7-4 lists the prepared groove sizes, measured weld penetration depths, and the weld cross-section images for all the samples with EMAT ultrasound reception. The ruler in the image has the unit of inch.

Table 7-4: Weld samples for EMAT measurement.

Sample number	Groove size (mm)	Measured penetration depth (mm)	Weld cross-section image
1	0	3.226	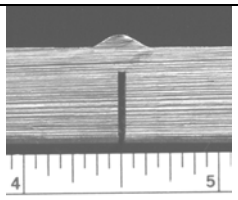
2	1.1	3.685	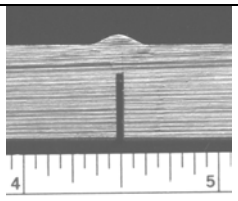
3	2.2	4.931	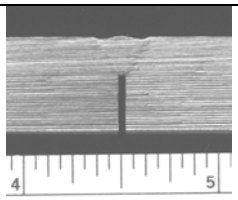
4	3.3	6.371	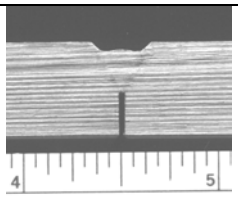
5	4.4	7.190	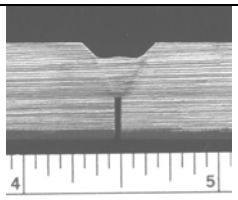
6	5.5	8.655	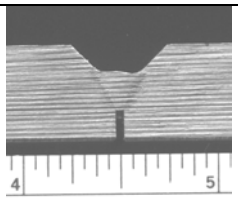
7	6.6	9.235	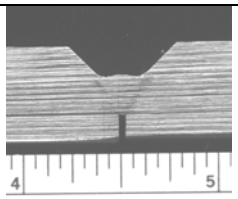

Fig. 7-18 shows the ultrasonic signals received by the EMAT for the 7 samples with different penetration depths. The signals are the averaging of 3 consecutive real-time signals. Note that the difference of ToFs for different samples is not obvious. The small change in ToF has to be estimated very accurately and reliably, which makes the cross-correlation method a necessity.

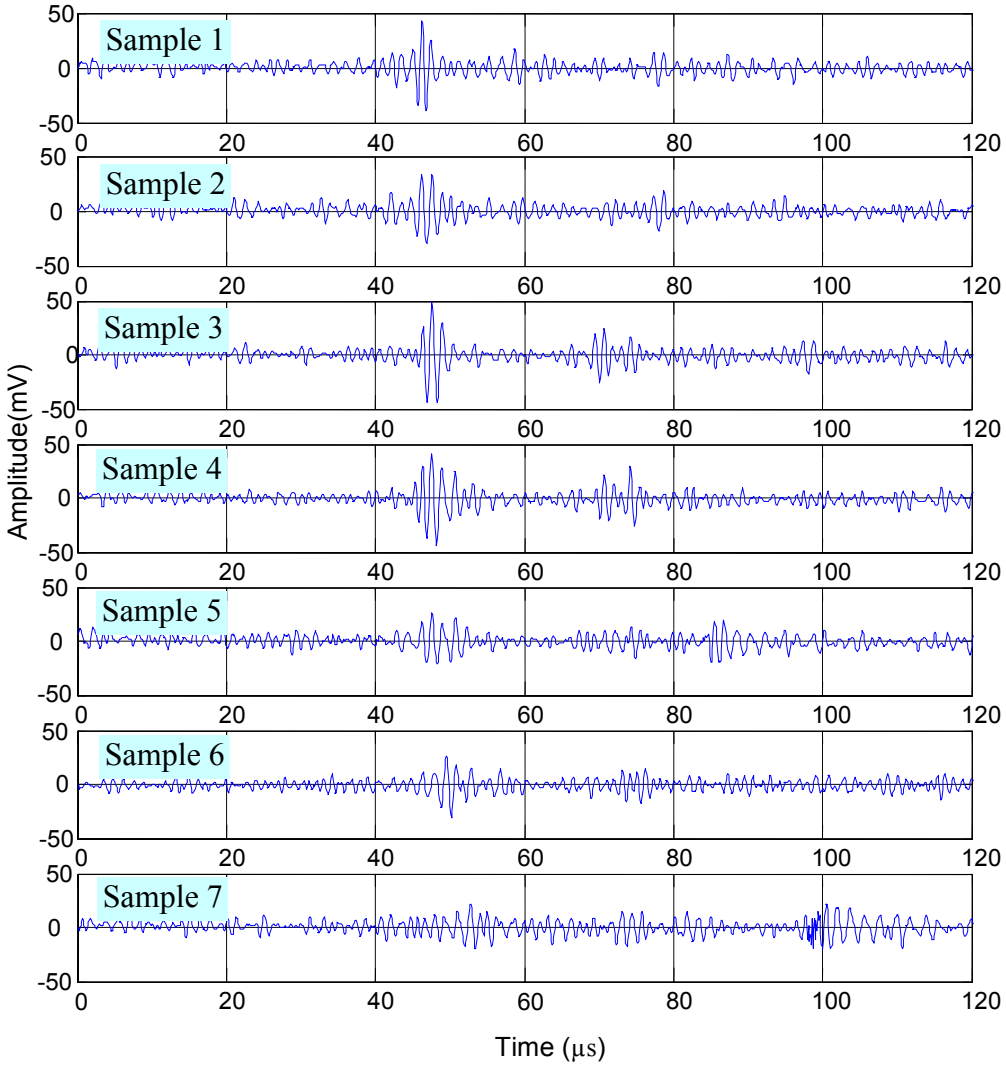

Fig. 7-18: Ultrasonic signals received by EMAT for different penetration depth. (2 seconds after the welding torch passes the sensor; average of 3 consecutive signals)

The experimental and numerical results of the relative ToF are plotted at a series of times shortly after the welding torch passes the sensing system, as shown in Fig. 7-19 to Fig. 7-23. When the SSE is used as a criterion for how good the agreement is, the experimental ToF gives the best match to the numerical result at t_{ts} = 2.0 seconds. The same conclusion is drawn as from PZT receivers. This implies that the torch-sensor distance should be set at d_{ts} = 1 inch when the sensor is moving along with the welding torch.

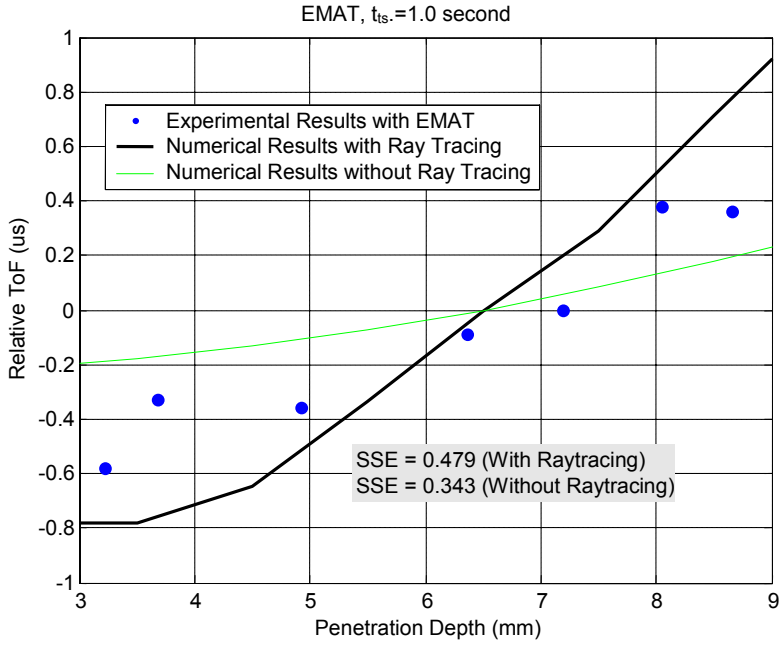

Fig. 7-19: Comparison of experimental and numerical ToF results (EMAT, t_{ts} = 1.0 s).

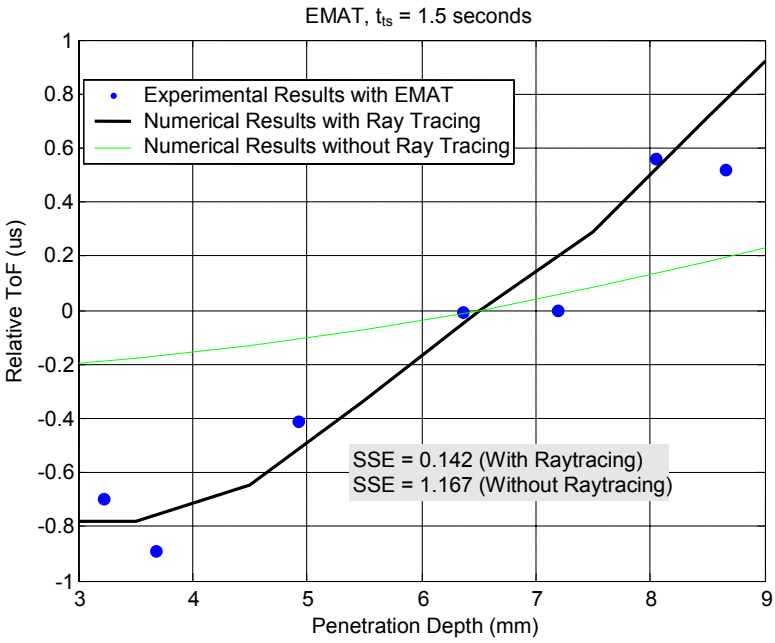

Fig. 7-20: Comparison of experimental and numerical ToF results (EMAT, t_{ts} = 1.5 s).

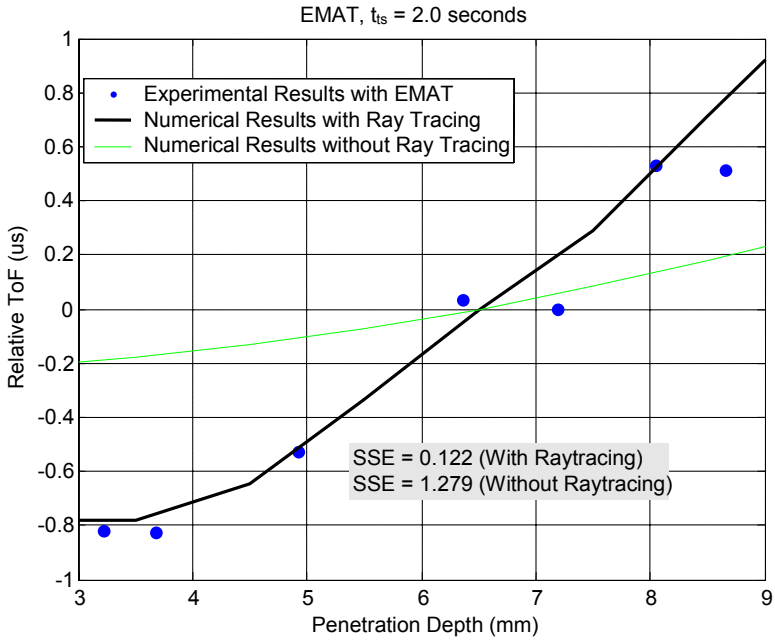

Fig. 7-21: Comparison of experimental and numerical ToF results (EMAT, t_{ts} = 2.0 s).

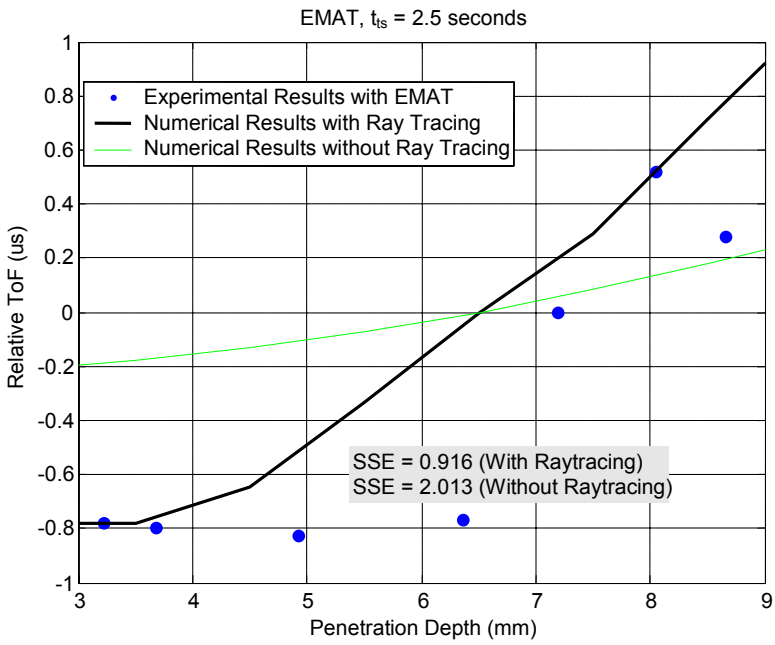

Fig. 7-22: Comparison of experimental and numerical ToF results (EMAT, t_{ts} = 2.5 s).

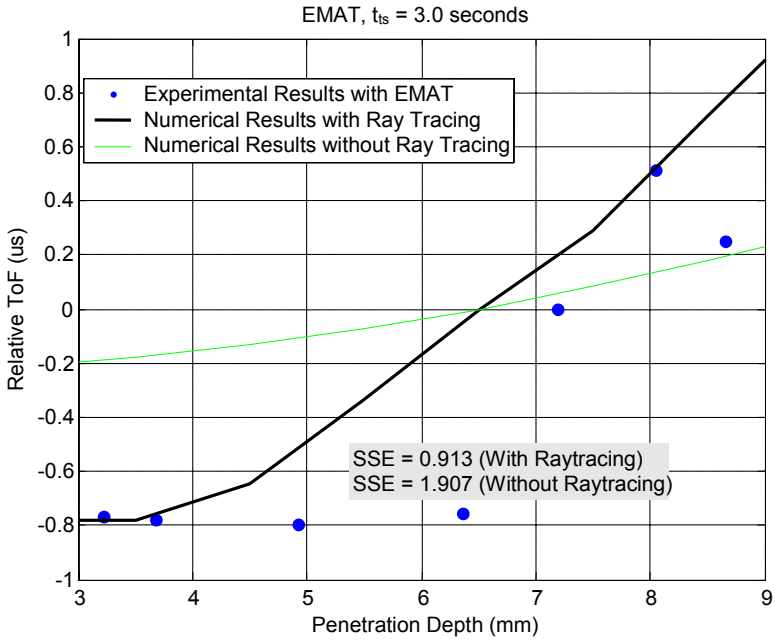

Fig. 7-23: Comparison of experimental and numerical ToF results (EMAT, t_{ts} = 3.0 s).

CHAPTER VIII

CONTRIBUTIONS AND IMPACTS

8.1 CONTRIBUTIONS

My contributions in this research can be summarized as the following.

1. Implemented and optimized fiber phased array ultrasound generation unit. Designed fixtures to hold the fiber bundles. Characterized the laser energy delivered by each fiber with a laser power meter and optimized the coupling of the pulsed laser beam into the 21-fiber bundle.
2. Built a parametric transient FEA model in Ansys to predict the temperature distribution during welding.
3. Developed a 3-D ray tracing algorithm directly from Fermat's principle. In solving the ray tracing equations, the ultrasound velocity field is derived from the transient temperature distribution obtained from FE simulation. Shooting method is applied to numerically trace the rays specified by two boundary locations. GMAW experiments have been performed and the experimental ToF is used to verify the numerical results. When SSE is used as a criterion, the experimental ToF results match numerical ToF with ray tracing better than numerical ToF when straight line is assumed (without ray tracing).

4. Developed a signal processing algorithm based on cross-correlation technique to estimate the ToF of the ultrasound, which is later correlated to the weld penetration depth.
5. Conducted experiments with the fiber phased array as the ultrasound generator and both the PZT and EMAT as the receivers. Designed fixtures to configure the weld samples and the transducers so that their locations are consistent. Correlated the experimental ToF to the weld penetration depth. Validated the numerical ray tracing results with the experimental measurements.

8.2 IMPACTS

Controlling welding parameters through a real-time sensory feedback will reduces cost, heat affected zone, material degradation, and thermal distortion. Hence it will increase throughput and weld quality. This will have important financial implications in industries that use welding in their products and in construction industries. So far, the development of reliable non-contact, non-destructive, on-line sensors, which are able to detect defects as they form and with the capability of operating at high temperatures and in harsh environments, remains a big challenge to a fully automated robotic welding process.

The real-time weld penetration depth sensing system developed in this research is efficient and can readily be deployed in a commercial application. The successful completion of this research will remove the major obstacle to a fully automated robotic welding process. An on-line welding system will facilitate mass production characterized by consistency, high quality, and low costs. Moreover, such in-process control will

relieve human operators of tedious, repetitive, and hazardous welding tasks, thus reducing welding-related injures.

CHAPTER IX

CONCLUSIONS AND RECOMMENDATIONS

9.1 CONCLUSIONS

This research work has demonstrated the application of the fiber phased array and EMAT for the real-time monitoring of weld penetration depth. Fiber phased array allows flexible source configuration and noncontact generation of laser ultrasound. The use of an EMAT allows the noncontact reception of ultrasound and hence withstands high temperatures involved in the welding process and rough surfaces. The overall system provides a noncontact and nondestructive evaluation method for real-time welding process control.

A transient FE model is developed to predict the temperature distribution during GMAW. The temperature obtained is used to derive the ultrasound velocity field for the ray tracing algorithm and determine the temperature requirement for the transducers. A 3-D ray tracing algorithm is developed directly from Fermat's principle to understand the ultrasound propagation in a temperature gradient. Shooting method is applied to numerically trace the rays specified by two boundary locations. GMAW experiments have been performed and the experimental ToF is used to verify the numerical results.

When SSE is used as a criterion, the experimental ToF results match numerical ToF with ray tracing better than numerical ToF when straight line is assumed (without ray tracing).

The results show that the effects of the temperature gradients on the ultrasound propagation can be understood and calculated. The experimental results with both the PZT and the EMAT indicate that the best correlation between the estimated ToF and the weld penetration depth is obtained at t_{ts} = 2 seconds. This implies a torch-sensor distance of 1 inch when sensing system is moving along with the welding torch.

The established relationship between ToF and weld penetration depth will be used in the design of real-time weld penetration depth monitoring and control system. The information on weld penetration depth extracted from the ultrasonic signals can be used as feedback to control the welding parameters (such as welding current, arc voltage, welding speed, etc…), to achieve desired penetration, and hence to improve weld quality. The real-time weld sensing technique developed is efficient and can readily be deployed for commercial applications.

9.2 RECOMMENDATIONS

The current results show that this technique is a promising approach to monitor the weld penetration depth in real-time. However, future work is still required to deploy this technique into a commercial system to feedback control the welding process in real-time.

1. Other thickness of the weld samples should be investigated to determine the system's limitation in thickness.

2. The sensing system, including both fiber phased array generation and the EMAT reception subsystems, should be designed to move along with the welding torch so that a real-time sensing and feed back control scheme can be tested. To achieve this, a lot of design and optimization work is involved. The fiber phased array needs to be reconfigured so that its distal end is flexible enough to move along with the welding torch without breaking fibers. For the EMAT, a strong dragging force is required due to its strong magnetic attraction force. The surface of the test piece must be clean and free of magnetic particles in the moving area. This could be accomplished by using an air nozzle pointed ahead of the probe travel, followed up by a strong magnet with a small gap mounted ahead of the EMAT probe in the direction of travel.

3. The current system setup could be used to investigate the detection of other types of defects of the weld in real-time, e.g., welding cracks, porosity, dimensional defects, deformations, incomplete fusion, and nonmetallic inclusions. Once the ultrasonic signal is received by the EMAT and acquired by the computer, other signal features such as signal strength and frequency components could be correlated to certain types of the weld defects.

REFERENCES

[1] Allison, S.W., Gillies, G.T., Magnuson, D.W. and Pagano, T.S. "Pulsed Laser Damage to Optical Fibers," *Applied Optics*, Vol. 24, No. 19, 1985, pp. 3140-5

[2] Aussel, J.D., LeBrun, A., and Baboux, J.C., "Generating Acoustic Waves by Laser: Theoretical and Experimental Study of the Emission Source", *Ultrasonics*, Vol. 26, No. 5, 1988, pp. 245-55

[3] Aussel, J.D. and Monchalin, J.P., "Measurement of Ultrasound Attenuation by Laser Ultrasonics", *Journal of Applied Physics*, Vol. 65, No. 8, 1989, pp. 2918-22

[4] Aussel, J.D. and Monchalin, J.P., "Precision Laser-Ultrasonic Velocity Measurement and Elastic Constant Determination", *Ultrasonics*, Vol. 27, No. 3, 1989, pp. 165-77

[5] Beck, T., Reng, N., and Richter, K. "Fiber Type and Quality Dictate Beam Delivery Characteristics," *Laser Focus World*, Vol. 29, No. 10, 1993, pp. 111-5.

[6] Bendat, J.S., Piersol, A.G., *Engineering Applications of Correlation and Spectral Analysis*, John Wiley & Sons, Inc., 2nd Edition, 1993

[7] Bernstein, J.R. and Spicer, J.B., "Line Source Representation for Laser-Generated Ultrasound in Aluminum", *Journal of the Acoustical Society of America*, Vol. 107, No. 3, 2000, pp. 1352-7

[8] Boo, K.S., Cho, H.S., "Transient Temperature Distribution in Arc Welding of Finite Thickness Plates", *Proceedings of the Institution of Mechanical Engineers*, Vol. 204, 1990, pp.175-82.

[9] Bruinsma, A. J.A., and Vogel, J.A., "Ultrasonic Non-contact Inspection System with Optical Fiber Methods," *Applied Optics*. Vol. 27, No. 22, 1988, pp. 4690-5

[10] Carlson, N.M., Johnson, J.A., "Ultrasonic Sensing of Weld Pool Penetration", *Welding Journal*, Vol. 67, No. 11 1988, pp. 239s-46s

[11] Carlson, N.M., Johnson, J.A., Lott, L.A., Kunerth, D.C., "Ultrasonic NDT Methods for Weld Sensing", *Materials Evaluation*, Vol. 50, 1992, pp. 1338-43

[12] Chandel, R.S., Oddy, A.S., Goldak, J.A., "Computer Prediction of Weld Bead Shapes", *Second International Conference of Computer Technology in Welding*, pp159-167, 1988

[13] Chapre, S.C., Canale, R.P., *Numerical Methods for Engineers: With Programming and Software Applications*, McGraw-Hill Science/Engineering/Math, 3rd Edition, 1998

[14] Chen, W.H., Nagarajan, S., and Chin, B.A., "Weld Penetration Sensing and Control", *SPIE – Infrared Technology XIV*, Vol. 972, 1988, pp. 268-72

[15] Dewhurst, R.J., Nurse, A.G., and Palmer, S.B., "High Power Optical Fiber Delivery System for the Laser Generation of Ultrasound", *Ultrasonics*, Vol. 26, No. 6, 1988, pp. 307-10

[16] Ditchburn, R.J., Burke, S.K., and Scala, C. M., "NDT of Welds: State of the Art", *NDT & E International*, Vol. 29, No. 2, 1996, pp. 111-7

[17] Dixon, S., Edwards, C., and Palmer, S. B., "A laser-EMAT System for Ultrasonic Weld Inspection", *Ultrasonics*, Vol. 37, No. 4, 1999, pp. 273-81

[18] Doubrava, J. H., Ticknor, G. W., Jones, M. G., "Implementation of Laser Welding for Lamp Leads," *ICALEO*, 1990, pp. 400-10.

[19] Goldak, J., Bibby, M., et al., "Computer Modeling of Heat Flow in Welds", *Metallurgical Transactions*, Vol. 17B, 1986, pp. 587-600

[20] Graff, K.F., *Wave Motion in Elastic Solids*, Ohio State University Press, Columbus, 1975

[21] Graham, G.M., Ume, I.C., "Automated System for Laser Ultrasonic Sensing of Weld Penetration", *Mechatronics*, Vol. 7, No. 8, 1997, pp. 711-21

[22] Graham, G.M., Sanderson, T.M., Ume, I.C., "Intelligent Welding with Laser Ultrasonic Sensing", *Proceedings of 1st World Congress on Intelligent Manufacturing Processes and Mayaguez*, San Juan, Puerto Rico, Feb. 1995, pp. 1043-53

[23] Grechka, V.Y., McMechan, G.A., "3-D Two-Point Ray Tracing for Heterogeneous Weakly transversely Isotropic Media", *Geophysics*, Vol. 61, No. 6, 1996, pp. 1883-94

[24] Guu, A.C., Rokhlin, S.I., "Arc Weld Process Control Using Radiographic Sensing", *Materials Evaluation*, Vol. 50, No. 11, 1992, pp. 1344-8, 1356

[25] Hopko, S.N., "Laser Ultrasonic Probe for Industrial or High Temperature Applications", Ph.D. Dissertation, Georgia Institute of Technology, 1998

[26] Hopko, S.N., Ume, I.C., "Laser Generated Ultrasound by Material Ablation Using Fiber Optic Delivery", *Ultrasonics*, Vol. 37, No. 1, 1999, pp.1-7

[27] Hull, D.R., Kautz, H.E., Vary, A., "Measurement of Ultrasonic Velocity Using Phase-Slope and Cross-Correlation Methods", *Materials Evaluation*, Vol. 43, No. 11, 1985, pp. 1455-60

[28] Hutchins, D.A., Dewhurst, R.J., and Palmer, S.B., "Directivity Patterns of Laser-Generated Ultrasound in Aluminum", *Journal of the Acoustical Society of America*, Vol. 70, No. 5, 1981, pp. 1362-69

[29] Hutchins, D., Hu, J., Lundgren, K., "A Comparison of Laser and EMAT Techniques for Noncontact Ultrasonics", *Materials Evaluation*, Vol. 44, No. 10, 1986, pp. 1244-53

[30] Ing, R.K., Fink, M., and Gires, F., "Directivity Patterns of a Moving Thermoelastic Source in Solid Media," *IEEE Transactions on Ultrasonics, Ferroelectrics and Frequency Control*, Vol. 39, No. 2, 1992, pp. 285-92

[31] Jarzynski, J. and Berthelot, Y. H., "The Use of Optical Fibers to Enhance the Laser Generation of Ultrasonic Waves," *Journal of Acoustical Society of America*, Vol. 85, No. 1, 1989, pp. 158-62

[32] Jasper, K., Scheede, S., Burghardt, B., Senczuk, R., Berger, P., Kahlert, H.J., "Excimer Laser Beam Homogenizer with Low Divergence", *Applied Physics A (Materials Science Processing)*, Vol. A69, 1999, pp. S315-8

[33] Johnson, J.A., Carlson, N.M., and Lott, L.A., "Ultrasonic Wave Propagation in Temperature Gradients", *Journal of Nondestructive Evaluation*, Vol. 6, No. 3, 1987, pp. 147-56

[34] Jones, M. G. "Laser Materials Processing with a Lensless Fiber Optic Output Coupler", U.S. Patent #4799755, 1989.

[35] Kannatey-Asibu, E., Kikuchi, N., Jallad, A, "Experimental Finte Element Analysis of Temperature Distribution During Arc Welding", *Journal of Engineering Materials and Technology*, Vol. 111, No. 1, 1989, pp. 8-18

[36] Kovacevi, R., Cao, Z.N., and Zhang, Y.M., "Role of Welding Parameters in Determining the Geometrical Appearance of Weld Pool", *Journal of Engineering Materials and Technology*, Vol. 118, No. 4, 1996, pp. 589-95

[37] Kou, S., Le, Y., "Welding Parameters and the Grain Structure of Weld Metal – A Thermaldynamic Consideration", *Metall. Trans*., Vol. 19A, 1988, pp. 1075

[38] Kurtz, A.F., "Design of a laser printer using a laser array and beam homogenizer", *Proceedings of SPIE*, Vol. 4095, 2000, pp. 147-153

[39] Lanza di Scalea, F., Berndt, T.P., Spicer, J.B., and Djordjevic, B.B., "Remote Laser Generation of Narrow-Band Surface Waves Through Optical Fibers", *IEEE Transactions on Ultrasonics, Ferroelectrics, and Frequency Control*, Vol. 46, No. 6, 1999, pp. 1551-7

[40] Lewis, C.L.S., Weaver, I., Doyle, L.A., *et al.*, "Use of a Random Phase Plate as a Krf Laser Beam Homogenizer for Thin Film Deposition Applications", *Review of Scientific Instruments*, Vol. 70, No. 4, 1999, pp. 2116-21

[41] Liao, T.W., Li, Y., "An Automated Radiographic NDT System for Weld Inspection", *NDT&E International*, Vol. 31, No. 3, 1998, pp. 183-92

[42] Ludwid, R., You, Z., Palanisamy, R., "Numerical Simulations of an Electromagnetic Acoustic Transducer-Receiver System for NDT Applications", *IEEE Transactions on Magnetics*, Vol. 29, No. 3, 1993, pp. 2081-89

[43] Miller, G.F., Pursey, H., "The Field and Radiation Impedance of Mechanical Radiators on the Free Surface of a Semi-infinite Isotropic Solid", *Proceeding of the Royal Society*, Vol. A223, 1954, pp. 521-41

[44] Miller, M., Mi, B., Kita, A., and Ume, C., "Development of Automated Real-Time Data Acquisition System for Robotic Weld Quality Monitoring", *Mechatronics*, Vol. 12, No. 9-10, 2002, pp. 1259-69

[45] Murray, T. W., Deaton, J. B., and Wagner, J. W., "Experimental Evaluation of Enhanced Generation of Ultrasonic Waves Using an Array of Laser Sources," *Ultrasonics*, Vol. 34, 1996, pp. 69-77

[46] Nagarajan, S., Chen, W.H., and Chin, B.A., "Infrared Sensing for Adaptive Arc Welding", *Welding Journal*, Vol. 68 No. 11, 1989, pp. 462s-6s

[47] Noroy, M., Royer, D., Fink, M.A., "The Laser-Generated Ultrasonic Phased Array: Analysis and Experiments", *Journal of Acoustical Society of America*, Vol. 94, No. 4, 1993, pp. 1934-43

[48] Noroy, M., Royer, D., Fink, M.A., "Shear-Wave Focusing with a Laser-Ultrasound Phased-Array", *IEEE Transactions on Ultrasonics, Ferroelectrics and Frequency Control*, Vol. 42, No. 6, 1995, pp. 981-8

[49] Oursler, D.A., Wagner, J.W., "Narrow-band Hybrid Pulsed Laser/EMAT System for Non-Contact Ultrasonic Inspection Using Angled Shear Waves", *Material Evaluation*, Vol. 53, No. 5, 1995, pp. 593-7

[50] Placious, R.C., Garrett, D.A., Kasen, M.B., Berger, H., "Dimensioning Flaws in Pipeline Girth Welds by Radiographic Methods", *Materials Evaluation*, Vol. 39, No. 8, 1981, pp. 755-60

[51] Prasad, S., Narayanan, T.K.S., "Finite Element Analysis of Temperature Distribution during Arc Welding Using Adaptive Grid Technique", *Welding Journal*, Vol. 75, 1996, pp. 123s-8s

[52] Radaj, D., *Heat Effects of Welding*, Berlin Heidelberg, New York, 1992, pp. 20-30

[53] Richardson, R. W., Gutow, D. A., and Rao, S. H., "A Vision Based System for Arc Weld Pool Size Control", *Winter Annual Meeting of ASME*, Phoenix, AZ, USA, 1982, pp. 65-75

[54] Rokhlin, S.I., "In-process Radiographic Evaluation of Arc Welding", *Materials Evaluation*, Vol. 47, No. 2, 1989, pp. 219-24

[55] Rose, L. R. F. "Point-Source Representation for Laser-Generated Ultrasound*," Journal of Acoustical Society of America*, Vol. 75, 1984, pp. 723-32

[56] Sadeghi, H., Suzuki, S., and Takenaka H., "A Two-Point, Three-Dimensional Seismic Ray Tracing Using Genetic Algorithms", *Physics of the Earth and Planetary Interiors*, Vol. 113, 1999, pp. 355-65

[57] Savage, W.F., Lundin, C.D., and Aronson, A.H., "Weld Metal Solidification Mechanics", *Welding Journal*, Vol. 44, 1965, pp. 175

[58] Scruby, C.B., Jones, K.R., and Antoniazzi, L., "Diffraction of Elastic Waves by Defects in Plates: Calculated Arrival Strengths for Point Force and Thermoelastic Sources of Ultrasound", *Journal of Nondestructive Evaluation*, Vol. 5, No. 3, 1986, pp. 145-56

[59] Scruby, C.B., Moss, B.C., "Non-Contact Ultrasonic Measurements on Steel at Elevated Temperatures*", NDT&E International,* Vol. 26, No. 4, 1993, pp. 177-88

[60] Scruby, C.B., Smith, R.L., and Moss B.C., "Microstructural Monitoring by Laser-Ultrasonic Attenuation and Forward Scattering", *NDT International*, Vol. 19, No. 5, 1986, pp. 307-13

[61] Shah, P.M., "Ray Tracing in Three Dimensions", *Geophysics*, Vol. 38, No. 3, 1973, pp. 600-4

[62] Smith, D., *Welding Skills and Technology*, McGraw-Hill, New York, 1984

[63] Stroud, R., "Problems and Observations whilst Dynamically Monitoring Molten Weld Pools Using Ultrasound", *British Journal of Non-Destructive Testing*, Vol. 31, No. 1, 1989, pp. 29-32

[64] Sugitani, Y., Nishi, Y., and Sato, T., "Intelligent Arc Welding Robot with Simultaneous Control of Penetration Depth and Bead Height", *NKK Technical Review*, No. 58, Apr. 1990, pp. 93-9

[65] Sundell, R. E., Solomon, H. D., and Correa, S. M., "Minor Element Effects On Gas Tungsten Arc (GTA) Weld Penetration - Weld Pool Physics", *Proceedings of an International Conference on Trends in Welding Research*, Gatlinburg, TN, USA, 1986, pp. 53-7

[66] Vogel, J. A., Bruinsma, J. A., and Berkhout, A. J., "Beamsteering of Laser Generated Ultrasound," *Proceedings of Ultrasonics International*, Butterworth, Washington, D. C., 1987, pp. 141-52.

[67] Vorontsov, G.A., "Automatic In-Process Control of Penetration Depth in Electric Plug Welding", *Automatic Welding*, Vol. 23, No.2, 1970, pp. 28-31

[68] Weinstock, R., *Calculus of Variations: With Applications to Physics and Engineering*, Dover Publications, Inc., New York, 1952, pp. 67-71

[69] White, R.M. "Generation of Elastic Waves by Transient Surface Heating," *Journal of Applied Physics*, Vol. 34, 1963, pp. 3559-67

[70] Yang, J., DeRidder, N., Ume, C., Jarzynski, J., "Non-Contact Optical Fiber Phased Array Generation of Ultrasound for Nondestructive Evaluation of Materials and Processes", *Ultrasonics*, Vol.31, No.6, 1993, pp. 387-94

[71] Yang, J., Ume, I.C., "Performance Evaluation of Fiber Array for NDE Application", *Research in Nondestructive Evaluation*, Vol. 5, No. 3, 1994, pp. 175-90